X-RAY SPECTROSCOPY OF ORGANIC MATERIALS

A Thesis Submitted to the College of

Graduate Studies and Research

In Partial Fulfilment of the Requirements

For the Degree of Doctor of Philosophy

In the Department of Physics and Engineering Physics

University of Saskatchewan

Saskatoon

By

REGAN GEORGE WILKS

Permission to Use

In presenting this thesis in partial fulfilment of the requirements for a Postgraduate degree from the University of Saskatchewan, I agree that the Libraries of this University may make it freely available for inspection. I further agree that permission for copying of this thesis in any manner, in whole or in part, for scholarly purposes may be granted by Dr. Alexander Moewes or, in his absence, by the Head of the Department or the Dean of the College in which my thesis work was done. It is understood that any copying, publication, or use of this thesis or parts thereof for financial gain shall not be allowed without my written permission. It is also understood that due recognition shall be given to me and to the University of Saskatchewan in any scholarly use which may be made of any material in my thesis.

Requests for permission to copy or to make other use of material in this thesis in whole or part should be addressed to:

Head of the Department of Physics and Engineering Physics

University of Saskatchewan

Saskatoon, Saskatchewan

S7N 5E2

Abstract

The radiation-induced decomposition of glycine is studied using a combination of Near Edge X-ray Absorption Fine Structure (NEXAFS) measurements and density functional theory calculations. Principal Component Analysis was used to determine the number of distinct molecules that were needed to explain the observed changes in the measured spectra, and the emerging absorption features are assigned to various product molecules through comparison with simulated spectra of several model compounds. It is clear from the experiment that the major effect of soft X-ray irradiation is the fragmentation of the molecule, primarily at the carbonyl sites. Peptide formation is shown to occur under irradiation; a condensation reaction initiated by the removal of a carbonyl oxygen is the proposed mechanism. This study utilizes a novel approach to the study of radiation damage that can occur during measurements, and suggests that it may be possible to use simulated model spectra to correct for these effects in measured spectra.

A study of oligothiophene-based molecular semiconductor materials with potential applications in light-emitting and photovoltaic devices is undertaken. Angle-resolved NEXAFS measurements of the star-shaped 4(HPBT) molecules on an amorphous indium surface show a strong dichroic signal indicating a well-ordered, uniformly upright arrangement of planar molecules. The X-ray excited optical luminescence (XEOL) measurements showed several sharp features associated with vibronic splitting of the LUMO-HOMO luminescent transition. The HOMO-LUMO gap determined from the XEOL measurements is 2.28 eV; this value is in agreement with previously published optical measurements as well as with the value that is estimated from the combination of NEXAFS and X-ray emission spectroscopy (XES) measurements. Films formed from blended solutions of 4(HPBT) and the hole-transporting molecular semiconductor PCBM are shown to form a bilayer structure with the PCBM adjacent to the substrate. Annealing causes desorption of the 4(HPBT) from the surface.

Acknowledgements

I would like to thank my faculty advisors, Alexander Moewes and Gap Soo Chang, for their help and support during the course of my degree. I would also like to thank the beamline scientists at the SGM Beamline at the CLS – Rob Blyth and Tom Regier – as well as at Beamline 8.0.1 at the ALS – Jonathan Denlinger and Wanli Yang. The contribution of my Advisory Committee members is greatly appreciated.

Funding by the Natural Sciences and Engineering Research Council of Canada (NSERC) and the Canada Research Chair program is gratefully acknowledged. Research described in this thesis was performed at the Canadian Light Source, which is supported by NSERC, NRC, CIHR, and the University of Saskatchewan. The work at the Advanced Light Source at Lawrence Berkeley National Laboratory was supported by the U.S. Department of Energy (Contract DE-AC03-76SF00098).

Contents

List of Tables

List of Figures

List of Abbreviations

4(HPBT)	1,2,4,5-tetra(50 -hexyl-[2,20]-bithiophenyl-5-vinyl)-benzene
ALS	Advanced Light Source
BL8	Beamline 8.0.1
CLS	Canadian Light Source
DFT	Density Functional Theory
DMFT	Dynamic Mean-Field Theory
DZVP	Double-Zeta plus Valence Polarisation
ECP	Effective Core Potential
EPR	Electron Paramagnetic Resonance
FY	Fluorescence Yield
GTO	Gaussian Type Orbital
HOMO	Highest Occupied Molecular Orbital
LDA	Local Density Approximation
LUMO	Lowest Unoccupied Molecular Orbital
MCP	Multi-Channel Plate
MO	Molecular Orbital
NEXAFS	Near Edge X-ray Absorption Fine Structure
NXES	Nonresonant X-ray Emission Spectroscopy
OLED	Organic Light-Emitting Diode
P3HT	Poly(3-hexylthiophene)
Pc	Pthalocyanine
PCA	Principal Component Analysis
PCBM	methanofullerene [6,6]-phenyl C_{61}-butyric acid methyl ester
PFY	Partial Fluorescence Yield
PLY	Partial Luminescence Yield
RF	Radio Frequency
RXES	Resonant X-ray Emission Spectroscopy
SCF	Self-Consistent Field
SGM	Spherical Grating Monochromator
TBPe	2,5,8,11-tetra-tertbutylperylene
TEY	Total Electron Yield
TFY	Total Fluorescence Yield
TM	Transition Metal
TR-XEOL	Time-Resolved X-ray Excited Optical Luminescence
TZVP	Triple-Zeta Plus Valence Polarization
UHV	Ultra High Vacuum
XAS	X-ray absorption Spectroscopy
XEOL	X-ray Excited Optical Luminescence
XES	X-ray Emission Spectroscopy

1. Introduction

This manuscript focuses on the use of soft X-ray spectroscopy in the study of various molecular materials. The problem of radiation damage is addressed in great detail via the study of radiation damage in glycine. Although it is a fairly small molecule, glycine is a very good subject for such a study, as it has a well-known structure, has been studied extensively using soft X-ray spectroscopy and other techniques, and contains carbon, nitrogen, and oxygen, allowing any energy- or element-dependent effects to be examined. The behaviour of irradiated glycine is also of some practical interest beyond the spectroscopic community; as the most basic building material for peptides and proteins it is an ideal model for any number of biological systems. This study shows the advantages and disadvantages of the application of these techniques to organic samples, as it shows that they can be readily damaged under normal experimental conditions, while the rich spectra that evolve as a function of this damage serve to illustrate the amount of structural and electronic information that can be obtained. Simulation of the spectra using density functional theory allows a model of the radiation damage mechanisms to be proposed, knowledge which may be useful in further experiments and in general studies of the interaction of ionizing radiation with biological matter.

The second major topic related to the study of molecular materials uses many of the same techniques that were employed in the radiation damage study to probe the properties of organic light-emitting diode materials. The study of TBPe, a useful blue emitter, was initiated as part of a collaboration with Dr. T.K. Sham of the University of Western Ontario, and will serve as an introduction to the study of organic light-emitting diode (OLED) materials using X-ray spectroscopy by comparing X-ray excited absorption, emission, and optical luminescence spectra with the spectra modelled with density functional theory, in order to gain useful insight into the electronic structure of the material, particularly the gap between the occupied and unoccupied molecular orbitals.

The themes from the study of TBPe will be greatly expanded upon in the study of the novel OLED material 4(HPBT). The main part of the study uses angle-dependent X-ray absorption spectroscopy to better understand the orientation of the molecules in films, a

property which has a great deal of influence on the device behaviour of molecular semiconductors. Improved methods for determining relevant electronic structure information, specifically the electronic energy gaps of the materials, were developed and will be described in detail; they will be applied to a number of samples in order to confirm that they give a suitable representation of the electronic structures of the materials. In addition to the study of pure 4(HPBT), further insight into its behaviour in devices was gained through the study of blended samples of 4(HPBT) and PCBM, a common fullerene-based organic semiconductor.

As an introduction to the studies described above, the first section of the manuscript will describe the experimental apparatus, namely synchrotron light sources. An overview of the theory and practice of the production of synchrotron radiation for use in experiments will be described, as will the instrumentation that is needed to manipulate the light according to the desires of the user. As well, the experimental techniques that are used in this study will be introduced, with a limited theoretical background and a description of the properties, strengths, and weaknesses of each. All of the measurements in this study have the same goal – the experimental determination of the electronic structure of a material. A brief introduction to the quantum mechanical theory behind electronic structures in materials will be used to introduce the numerical methods that are here employed to model it. A summary of the software used will be provided, as will a detailed description of the individual calculations that are needed to model the experimental spectra.

2. Theory and Calculations

The majority of spectroscopic techniques in materials science and condensed matter physics involve the measurement of the effects of the excitation of a material by an external energy source. In the current study, the excitation is achieved by the absorption of soft X-ray radiation – composed of photons with energy ranging from approximately 100 eV to 2000 eV – by bound electrons in a variety of molecular and crystalline materials. In a very broad and general sense, the goal of the measurements is to determine the characteristics of electrons in the presence of a potential that is created by the presence of various nuclei and by other electrons. Although the analysis of the measured spectra and numerical models contained in this manuscript will not be discussed in these terms, it is essential that the quantum mechanical basis of the studies be presented as a starting point for the discussion of the experimental and theoretical techniques that are utilised. Having established this basis, the electronic structure will generally be referred to as the electronic density of states, an energy-resolved representation of the likelihood of finding an electron at a particular energy.

2.1. Schrödinger's Equation

The two most important aspects of quantum mechanics as it pertains to the study of electrons in a material are also two of the most basic: quantization of energy and the wave nature of particles. Electrons are treated as a distributed wave of total charge $e = -6.02\text{x}10^{-19}$ C, and the existence of these waves in a potential leads them inevitably to occupy discrete energy levels. The energy levels of any particle in a potential are solutions of the time-dependent Schrödinger equation, which can be expressed in its very simplest form as:

$$H\Psi(x_1,x_2,x_3...,x_N) = E\Psi(x_1,x_2,x_3...,x_N) \tag{2.1}$$

In the above expression, the symbol Ψ denotes the N-electron wave function. The Hamiltonian, H, contains the description of the potentials that the electrons are subject to, and E represents the eigenvalues of the equations, namely the electron energy levels. For a generic assembly of n positively charged nuclei with atomic number Z and N negatively

charged electrons of charge *e*, the Hamiltonian will contain terms describing all of the interactions. It can be written in a basic form as:

$$H = -\sum_{i}^{N} \frac{\hbar^2}{2m_e} \nabla^2 - \sum_{k}^{n} \frac{\hbar^2}{2m_k} \nabla^2 - \sum_{i}^{N} \sum_{k}^{n} \frac{e^2 Z_k}{r_{ik}} + \sum_{i<j}^{j=N} \frac{e^2}{r_{ij}} + \sum_{k<l}^{k=n} \frac{e^2 Z_k Z_l}{r_{kl}} \qquad (2.2)$$

The five terms in the Hamiltonian describe, respectively, the electron kinetic energy, the nuclear kinetic energy, the electron-nucleus attraction, the interelectron repulsion, and the internuclear repulsion. Solving the Schrödinger equation with this Hamiltonian will provide a complete set of energy levels for the system. Unfortunately, the equation cannot be solved for the overwhelming majority of systems, and so approximations, generalizations, and simplified models must be developed to describe the system.

2.2. The Born-Oppenheimer Approximation

The introduction to this section referred to condensed matter physics as the study and modelling of the energy of electrons in a potential, but when the Hamiltonian was introduced, it contained extra terms describing the kinetic energy of the nuclei and the internuclear repulsion. This inconsistency can be explained by the first major simplification of the *N*+*n*-particle Hamiltonian: the Born-Oppenheimer Approximation. The basic assumption of the approximation is that the nuclear movement occurs on a much slower time scale than does the movement of the electrons, and so a reliable model of the electronic structure can be obtained by treating the nuclei as being fixed in space. This assumption results in a major simplification of the Hamiltonian, as it not only removes two terms from the expression, it removes the correlation between the nuclei and the electrons. Despite this simplification, the Schrödinger equation can still not be solved for any but a handful of systems, and so further approximations of the electronic structure are employed. All calculations, however, have the Born-Oppenheimer approximation of the Hamiltonian as an inherent part of their model.

2.3. Molecular Orbital Theory

A basic approximation of the electronic structure in molecules is known as molecular orbital (MO) theory. MO theory assumes that the electronic states in a molecule can be expressed in terms of orbitals of discrete energy, formed through superposition of the individual atomic wavefunctions of its components [1]. It is worth developing this model in a bit more detail, because although more sophisticated methods for simulating the electronic structure will be employed, many of the descriptions of the findings in the later sections of this manuscript will be explained using terminology from MO theory.

The simplest example of MO theory is the formation of bonding and antibonding orbitals in a diatomic molecule such as O_2. The electron configuration of atomic oxygen is $1s^2 2s^2 2p^4$, describing the occupation of the various orbital levels in terms of the primary quantum number n and the angular momentum quantum number l. The shapes of the s and p wavefunctions are well-known, and are outlined in Figure 2.1.

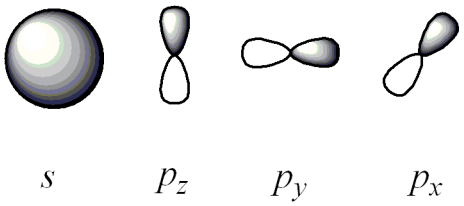

Figure 2.1: Shapes of *s* and *p* orbital wavefunctions.

In general oxygen needs to form two bonds in order to be stable within a molecule. It is for this reason that monatomic oxygen is not found in significant quantities in the environment; instead two oxygen atoms will be held together with a double bond (O=O), forming the stable, relatively nonreactive diatomic oxygen molecule. In a simple picture, the bond between the oxygen atoms contains two electrons with wavefunctions that extend across the interatomic bond. The MO picture of the bond formation involves the superposition of two of the *2p* functions. The wavefunctions can interfere either constructively, to form bonding orbitals, or destructively, to form antibonding orbitals. The diagram of O=O bond formation shown in Figure 2.2 describes the formation of both bonding and antibonding orbitals, and also introduces nomenclature that will be used

throughout the discussion of molecular spectroscopy. Molecular orbitals are labeled according to their symmetry characteristics; the orbitals in Figure 2.2 are antisymmetric with respect to reflection through a mirror plane containing the bond axis, and are designated as π (π*) bonding (antibonding) orbitals. Orbitals that are symmetric through this plane are called σ and σ* orbitals; their formation is shown in Figure 2.3.

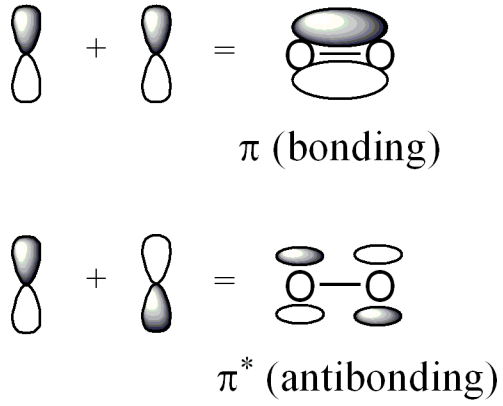

Figure 2.2: Formation of π (bonding) and π* (antibonding) orbitals by constructive and destructive interference of *p* orbitals.

The formation of a σ-bond in a F_2 molecule is shown in Figure 2.3. The σ orbital describes an electron distribution with the electron delocalized along the bond axis. These orbitals are formed by the interference of *p* or *s* orbitals that do not have nodes along the line of the bond axis.

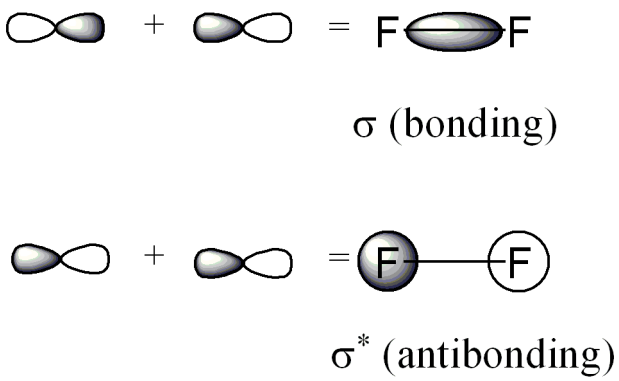

Figure 2.3: formation of σ (bonding) and σ* (antibonding) orbitals by constructive and destructive interference of *p* orbitals.

The terms bonding and antibonding are used in the general formation of MO theory, but for the remainder of this study the terms will be largely discarded. Instead, orbitals will be described as being either "occupied" or "unoccupied," to be consistent with discussions of density of states. Two more specific terms will be used extensively: the least-tightly bound occupied orbital will be referred to as the highest occupied molecular orbital (HOMO), and the most tightly-bound unoccupied orbital will be referred to as the lowest unoccupied molecular orbital (LUMO).

2.4. Density Functional Theory

In the previous sections, the density of electronic states was described in terms of the many-particle wavefunction $\Psi(x_1,x_2,x_3,\ldots x_N)$, which by definition explicitly contains all of the information about every electron in the system. The extraordinary complexity of this function means that it cannot be determined directly for all but the simplest systems. Methods for approximating this wavefunction, however, are common in materials research, and have proven to be extremely useful in the modelling and prediction of observable properties.

One common approach to modelling the electronic structures is density functional theory (DFT), in which the system of N electrons is treated as a cloud of charge Ne that is subjected to the potential created by the nuclei. This is, of course, a tremendous oversimplification of the DFT formalism, but it is a useful starting point for this introduction to the technique. The "cloud" in DFT is a density function, $\rho(\mathbf{r})$, that describes the distribution of the electrons in space. The density function can be related to the many-particle wavefunction as follows [2]:

$$\rho(\mathbf{r}) = N \int \ldots \int d\mathbf{r}_2 d\mathbf{r}_3 \ldots d\mathbf{r}_N \left|\Psi(\mathbf{r},\mathbf{r}_2,\mathbf{r}_3 \ldots \mathbf{r}_N)\right|^2 \tag{2.3}$$

This expression defines the likelihood of finding an electron at $\mathbf{r}$ when all of the other electrons in the system are found within the volume element defined by the integrals. The density function is subject to the normalization condition:

$$N = \int \rho(\mathbf{r}) d\mathbf{r} \tag{2.4}$$

The goal of DFT calculations is to establish a density function that is based on models of electron wavefunctions, optimize the model so that it represents the distribution of electrons in a real system as accurately as possible, and then analyse the density function to derive electronic structure information from it. The following sections will provide an overview of the basis and implementation of DFT methodology; the descriptions will largely follow those published by Cramer [3] and Chretien [2].

2.4.1. Hohenberg-Kohn Theorems

Modern density functional theory owes much to the work of Hohenberg and Kohn, whose proof of two theorems helped DFT to be developed into a viable computational technique [4]. The first proof establishes that the electron density is unique for a given external potential, and that knowledge of one can therefore be used to understand the other.

The proof proceeds by first assuming that there are multiple external potentials that will lead to the same density function, then showing that the inevitable outcome of this assumption contains a contradiction. The two potentials are given the generic names $V_a(\mathbf{r})$ and $V_b(\mathbf{r})$; their corresponding Hamiltonians are H_a and H_b. Application of the Hamiltonians to the ground state wavefunctions Ψ_a and Ψ_b gives the ground state energy eigenvalues E_a and E_b. By definition, E_a and E_b are the minimum energies that can exist in the presence of the two unique potentials. Therefore, assuming that the two wavefunctions are nondegenerate, the energy of Ψ_b in the presence of potential V_a must be greater than the ground state energy of Ψ_a in the same potential. This is described by the following inequality:

$$E_a < \langle \Psi_b | H_a | \Psi_b \rangle \tag{2.5}$$

A similar inequality can be constructed for E_a by reversing all of the subscripts, and the two expressions can be modified to give:

$$E_a < \langle \Psi_b | H_a - H_b + H_b | \Psi_b \rangle = \langle \Psi_b | V_a - V_b | \Psi_b \rangle + E_b$$
$$E_b < \langle \Psi_a | H_b - H_a + H_a | \Psi_a \rangle = \langle \Psi_a | V_b - V_a | \Psi_a \rangle + E_a \quad (2.6)$$

Adding these two expressions together leads to the contradictory inequality:

$$E_a + E_b < E_b + E_a \quad (2.7)$$

The significance of this proof is that it shows that two nonidentical external potentials cannot produce two identical wavefunctions, and therefore the density functions derived from the wavefunctions must be unique for a given potential. This is a necessary characteristic for the density function to have if it is to be of use in describing the electronic structure of a material.

Another important proof, though not nearly as complex as the existence theorem described above, provides a very basic introduction to the methods usually used to determine the nature of the density function. The Hohenberg-Kohn Variational Theorem outlines how, given a defined external potential, one would go about searching for the corresponding unique density function. The first step is to assume that there is a candidate density (ρ_C) and by extension a related candidate wavefunction (Ψ_C) and Hamiltonian (H_C). (The Hamiltonian must also have the "candidate" designation, because it contains terms related to the electron density as well as the external potential V.) The energy of the system (E_C) must by definition be greater than the ground state energy, unless in fact it is the ground state energy. This is expressed in terms of the candidate functions as:

$$E_0 \leq E_C = \langle \Psi_C | H | \Psi_C \rangle \quad (2.8)$$

Because it has already been shown that the electron wavefunction in a given external potential is unique, then there must exist a single wavefunction, and by extension a single density function, that produces the ground state energy E_0 as its eigenvalue. Therefore, the variational principal states that the ground state density can be found by varying the

density function across various parameters until the energy of the system is minimized. The minimum energy must then correspond to the ground state of the system.

2.5. The Kohn-Sham Self-Consistent Field Method

While the Hohenberg-Kohn theorems provided theoretical justification for the use of DFT in electronic structure calculations, they do not provide any real clue about how to construct the density function or how to determine the energy of the system. A major step forward in the implementation of the ideas came from Kohn and Sham in 1965 [5]. They proposed a major simplification to the model of the density function. The electrons in a material are a system of interacting particles; this correlation makes them difficult to model. The method that is proposed by Kohn and Sham is to assume that the density function represents a series of non-interacting particles that has the same ground state density as a system of interest in which the particles do interact. The Hamiltonian can then be expressed in the form of a sum of one-electron operators [3]. The kinetic energy and electron-electron repulsion effects are accounted for through operators that act on the system of non-interacting particles. The complete ground state energy functional for the system can be summarised as:

$$E_0\left[\rho(\mathbf{r})\right] = T_{n-i}\left[\rho(\mathbf{r})\right] + V\left[\rho(\mathbf{r})\right] + V_{ee}\left[\rho(\mathbf{r})\right] + \Delta T_i\left[\rho(\mathbf{r})\right] + \Delta V_{i-ee}\left[\rho(\mathbf{r})\right] \qquad (2.9)$$

The right-hand side of the functional contains terms accounting for the kinetic energy of the non-interacting particle, the external potential V (*i.e.* the nucleus-electron attraction), the electron-electron repulsion for the non-interacting system (essentially the energy required to assemble a uniform distribution of N electrons within the volume defined by ρ) V_{ee}, and the corrections to the classical kinetic energy (ΔT_i) and electron repulsion ($\Delta V_{i\text{-}ee}$) due to the interactions of the particles.

The density is expressed as the superposition of the individual orbital wavefunctions of non-interacting particles (φ):

$$\rho(\mathbf{r}) = \sum_{i}^{N} \langle \varphi_i(\mathbf{r}_i) | \varphi_i(\mathbf{r}_i) \rangle \tag{2.10}$$

Because the energy functional has been expressed in terms of single-electron operators, the total energy of the system is expressed as a summation over N of the energy of all individual orbital wavefunctions. The energy functional then has the form:

$$\begin{aligned} E[\rho(\mathbf{r})] = & \sum_{i}^{N} \left(\langle \varphi_i(\mathbf{r}_i) | -\frac{1}{2}\nabla_i^2 | \varphi_i(\mathbf{r}_i) \rangle - \langle \varphi_i(\mathbf{r}_i) | \sum_{k}^{n} \frac{Z_k}{|\mathbf{r}_i - \mathbf{r}_k|} | \varphi_i(\mathbf{r}_i) \rangle \right) \\ & + \sum_{i}^{N} \langle \varphi_i(\mathbf{r}_i) | \frac{\rho(\mathbf{r}')}{|\mathbf{r}_i - \mathbf{r}'|} d\mathbf{r}' | \varphi_i(\mathbf{r}_i) \rangle + E_{XC}[\rho(\mathbf{r})] \end{aligned} \tag{2.11}$$

Note that the non-classical corrections have been combined into a single functional E_{XC}. This is known as the exchange-correlation functional; its nature will be described in more detail in Section 2.6. The energy functional can be expressed in a more familiar fashion, in terms of a single-particle Hamiltonian given by:

$$h_{KS} = -\frac{1}{2}\nabla_i^2 - \sum_{k}^{n} \frac{Z_k}{|\mathbf{r}_i - \mathbf{r}_k|} + \int \frac{\rho(\mathbf{r}')}{|\mathbf{r}_i - \mathbf{r}'|} d\mathbf{r}' + V_{XC} \tag{2.12}$$

The exchange-correlation potential V_{XC} is defined as the derivative of the E_{XC} with respect to the density function $\rho(\mathbf{r})$. The last three terms in the above expression are collectively referred to as the effective potential:

$$V_{EFF}[\rho(\mathbf{r})] = \sum_{k}^{n} \frac{Z_k}{|\mathbf{r}_i - \mathbf{r}_k|} + \int \frac{\rho(\mathbf{r}')}{|\mathbf{r}_i - \mathbf{r}'|} d\mathbf{r}' + V_{XC}[\rho(\mathbf{r})] \tag{2.13}$$

Using the Kohn-Sham Hamiltonian and the definition of the effective potential, the single-particle Schrödinger equation can be written:

$$-\frac{1}{2}\nabla^2\varphi_i(\mathbf{r}) + V_{EFF}\left[\rho(\mathbf{r})\right]\varphi(\mathbf{r}) = \varepsilon_i\varphi_i \qquad (2.14)$$

Collectively, the equations describing the composition of the density function (2.10), the definition of the effective potential (2.13), and the single-particle Schrödinger equation (2.14) are known as the Kohn-Sham equations, and a self-consistent solution to all three will provide a model of the electronic structure of the system. An iterative approach is employed to solve them. A starting model of the density is used to calculate the effective potential V_{EFF} (2.13), which is then substituted into the Schrödinger equation (2.14). The eigenfunctions of the Schrödinger equation are used to formulate a new density function (2.10). The process is repeated until the changes in density and energy between iterations is less than a preset convergence criterion.

The DFT calculations that are presented in later sections use the StoBe software [6,7,8], which employs the general Kohn-Sham procedure described above. In practice, of course, the numerical implementation of the Kohn-Sham methodology is considerably more complicated, and some aspects of it will be discussed in the following sections, with particular reference to StoBe where appropriate.

2.6. Models of the Exchange-Correlation Functional

The basis of the models of the exchange-correlation functional is the inclusion of a Coulomb hole in the electron probability distribution. The presence of the positively charged Coulomb hole results in an attractive force that acts upon the electron density. A proper model of the hole will apply the necessary correction to the kinetic energy and electron-electron attraction terms, as described in Equation (2.11). The models used in StoBe are based on the generalised gradient approximation methods which were largely developed by Perdew [9,10,11,12]. Another model that is used was developed by Becke [13], who included empirical parameters in the model of the functional to correct the asymptotic behaviour. The exchange energies are unique functions of the density, having a general $\rho^{-1/3}$ dependence; the relationship with the density function is included present in all gradient approximations in the form of the parameter $s(\mathbf{r})$, which is defined in terms of the density as:

$$s(\mathbf{r}) = \frac{|\nabla\rho|}{\rho^{\frac{4}{3}}} \tag{2.15}$$

2.7. Basis Sets

Solving the Kohn-Sham equations requires initial models of the density and the exchange-correlation functions to be developed beforehand. The formation of the density is based on a summation of individual orbital functions as described in Equation (2.10), although the functions that are used to describe these orbitals have not yet been discussed.

The functions that are used to approximate the orbitals are known as basis functions, and all of the functions for a particular element are known collectively as a basis set. It is necessary, or at least very beneficial, that the functions used to model the orbitals have the same radial symmetry (*s*, *p*, *d*, etc.) as the orbitals themselves. This requirement still allows many different types of functions to be used in the model; the calculations in this work use sets of Gaussian–type orbitals (GTO). Gaussian functions do not have the same shape as do real atomic orbitals, especially near the origin [3], but they are relatively easy to manipulate, and multiple Gaussian functions can be added together to produce a model of the orbital functions that more closely mimics atomic orbitals. The orbitals in the calculations take the form:

$$\varphi_i = \sum_j a_j \chi_j \tag{2.16}$$

The index *j* can have a range of values, *a* is a real coefficient, and the function χ is the actual Gaussian function:

$$\chi = r^l e^{-\alpha r^2} \tag{2.17}$$

The *l* parameter is directly analogous to the *l* quantum number – it designates the function as *s*-type, *p*-type, etc.

The initial "guess" density function for the DFT calculation is constructed from tabulated orbital basis sets that are optimised for a particular element. The Gaussian basis sets in StoBe are based on the Huzinaga basis sets [14], originally formulated for Hartree-Fock calculations. The basis sets are essentially a list of coefficients a and exponents α for each function used in the basis set. Each atomic energy level is represented by a group of Gaussian functions that have been optimized such that they give the best possible representation of the shape of the atomic orbital. During the self-consistent field (SCF) procedure, the groups of orbital functions are varied in a correlated fashion – the "block" of functions is essentially treated as a single entity with a coefficient that can be varied. In practice, the values of the constants contained in the exponents do not change during the calculation.

The orbital basis sets are described by the number of *s*-, *p*-, and *d*-type functions that they contain; the general notation is (*ns*/*np*/*nd*). The simplest Huzinaga basis set designed to describe first-row elements has the notation (63/5). In this basis set, a block of six *s*-type Gaussian orbitals is used to approximate the *1s* level, a block of three GTOs represents the *2s* orbitals, and a block of five GTOs is used to model the *2p* orbitals. This basis set would provide an adequate description of the electronic structure of an isolated atom, but it is not sufficient to describe the behaviour of an atom that is subject to external potentials, i.e. one that is located in a molecule. To better approximate molecular orbitals the blocks of functions are broken up, forming a (621/41) set, allowing greater flexibility in response to the nuclear potential. To improve the basis set's description of polarization within the molecule, a *d*-type function is added to the expanded basis set, forming a double-zeta plus valence polarization (DZVP) basis set (621/41/1*). A better description of molecular orbitals is obtained by adding extra *p*- and *s*-type functions to the DZVP basis set and expanding it further. The majority of the calculations contained here use these (7111/411/1*) basis sets, called triple zeta plus valence polarization (TZVP). It is possible to perform the DFT calculations using only the orbital basis sets, as they are intended to provide a direct representation of the electrons in the system, but the SCF procedure can be speeded up by using additional basis sets – known as auxiliary basis sets – to model the electron density and the exchange-correlation functionals at certain points in the calculation. The auxiliary basis sets are also formed from Gaussian

functions, but they are functions of probability density, rather than probability amplitude, reducing the number of functions needed to model the density. The auxiliary basis sets decrease the number of calculations needed in steps of the SCF procedure that do not depend on constructive or destructive wave interference. The density is modelled in terms of the auxiliary basis functions as:

$$\rho_A = \sum_m b_m \Omega_m \tag{2.18}$$

The auxiliary models of the density and exchange-correlation functional are fitted to the orbital models at each step of the SCF procedure; the time needed to perform this operation is more than compensated for by the time that is saved in the overall calculation. Like the orbital basis sets, the auxiliary sets are described in terms of the number of each type of function they contain, although the form is slightly different as the auxiliary basis sets are composed of blocks of *s*-type and *spd*-type functions. The notation follows the basic form (v_s,v_{spd}:d_s,d_{spd}), giving the number of each type of function used to model the density (d) and the exchange-correlation functions (v).

When absorption spectra are simulated, an additional set of large, diffuse Gaussian functions centred on the excitation site is included. The functions in this augmentation basis set are intended to approximate the behaviour of the electrons excited above the ionization threshold. The spatial extent of the augmentation basis functions is finite, and so they do not reflect the true nature of these excitations; in practice they do provide an adequate model of the shape of the broad resonances above the ionization threshold.

3. Synchrotrons

The measurements included in this study were performed at two different electron storage rings: the Canadian Light Source (CLS) at the University of Saskatchewan and the Advanced Light Source (ALS) at the Lawrence Berkeley National Laboratory. Both sources are relatively compact, third-generation synchrotron light sources; the majority of the descriptions that follow are applicable to both facilities; specific characteristics of each facility will be included where appropriate.

3.1. Synchrotron Light

Intense light across a wide range of the electromagnetic spectrum can be created by the controlled acceleration of electrons. When it was first observed, this light was treated as a nuisance, as it was a major mechanism for energy loss in betatron storage devices. When a charged particle, an electron in the current study, travels along a curved path, it will emit radiation [15]; when it is produced from electrons with velocities approaching the speed of light the radiation pattern is folded forward in the direction of the electron's travel. This relativistic effect leads to an increase in the emitted power and a collimation of the beam. The angular distribution of the synchrotron radiation is related to the velocity (v_e) of the electrons and the speed of light in a vacuum (c) by the Lorentz factor:

$$\gamma = \frac{1}{\sqrt{1 - \frac{v^2}{c^2}}} \tag{3.1}$$

The power of the emitted radiation is closely related to the characteristics of the storage ring. Instantaneously, the power emitted by a high-energy (i.e. $\gamma \approx 1$) electron following a curved trajectory in a storage ring can be described in terms of its energy (E_{ring}), the storage ring current (I_{ring}), and the radius of curvature of its path (ρ) using the following equation:

$$P[kW] = \frac{8.85x10^{-2} E_{ring}^{4}[GeV] I_{ring}[mA]}{\rho[m]} \tag{3.2}$$

This emitted radiation can be seen as either a loss mechanism that needs to be overcome in order to maintain the energy of the electrons or as a valuable commodity that can be used in experiments. High power is only one of the characteristics of synchrotron radiation; in order to more completely describe the nature of the light and how it can be used in research, it is necessary to examine the structure of synchrotrons more closely.

3.2. Source Components

3.2.1. The Linear Accelerator

A linear accelerator is used to produce the electron beam that will eventually be used to create synchrotron radiation. Electrons are emitted by a cathode, and primary acceleration is via the application of a large potential difference. Energy is added to the beam as it passes through a radio frequency (RF) cavity. The electrons absorb radio waves; a secondary effect is that the electrons in the beam form bunches having a size related to the wavelength of the radio system. The linear accelerator at the CLS produces bunches of 250 MeV electrons that are then injected into the booster ring.

3.2.2. The Booster Ring

Facilities such as the CLS and the ALS are generally referred to as synchrotrons, but because the term refers to a circular particle accelerator in which variable magnetic fields are used to maintain the particles at a constant radius it can really only be accurately applied to one component of the facilities: the booster ring. In order to achieve the high electron energies that are characteristic of synchrotron light sources – 1.9 GeV at the ALS and 2.9 GeV at the CLS – the beam is sent along a circuitous path containing an RF system for acceleration and bending magnets that are used to control its trajectory. The electrons pass through each section of the booster ring many times, and this is the key difference between the booster ring and the linear accelerator. The RF system boosts the energy of the electron beam, causing further bunching, and the electrons gain energy each

time they pass through the RF system. The energy they gain in this way more than offsets the losses that occur as a result of the radiation emitted when the electrons pass through the bending magnets. These losses in energy due to the production of synchrotron radiation are, as was discussed earlier, a nuisance; the useful effects of this radiated power occur when the electron beam is injected into the storage ring.

3.2.3. The Storage Ring

Once the desired electron energy is obtained in the booster ring, the electrons are injected into the larger storage ring. The electrons circulate in this ring for hours, and the energy losses that occur as a result of passing through bending magnets and insertion devices are compensated for by a final RF system, which maintains the energy of the beam. The light produced when the electrons pass through the magnetic devices has distinct characteristics related to the device parameters, and so an introduction to the two main types of magnetic structures found in the storage ring will be beneficial.

3.2.4. Bending Magnets

Bending magnets in a synchrotron storage ring serve the dual purposes of controlling the trajectory of the electron bunches, steering them from one straight section into another, and producing a broad spectrum of radiation for use in experiments. Although no bending magnet-based beamlines were used in the current study, the importance of these devices necessitates a brief discussion of their operation and will serve to introduce some concepts that will arise in the description of insertion devices in the next section.

Bending magnets produce radiation in the manner described in Section 3.1, by forcing high-energy electrons to travel along a curved trajectory. The radiation has a smooth, continuous energy spectrum across a wide energy range. Typically, a synchrotron will be designed such that all bending magnets are identical, and so they will all have the same characteristic radiation spectrum. The curves showing the flux and brightness of the ALS bending magnets as a function of photon energy, taken from the ALS website [16], are shown in Figure 3.1.

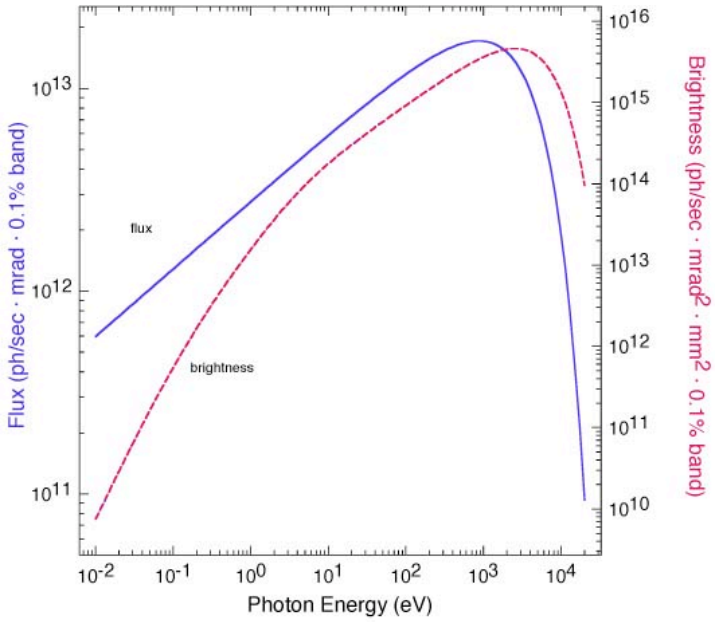

Figure 3.1: Flux and brightness curves for bending magnets at the Advanced Light Source synchrotron [16].

Bending magnets are characterized according to a quantity known as their critical photon energy (E_C), which is defined as the energy at which half of the energy emitted as photons has energy below E_C. For any bend magnet with a magnetic field B, this energy is given by the expression [15]:

$$E_C = 3e\hbar B\gamma^2 2m_e \tag{3.3}$$

where γ is the Lorentz factor in the laboratory frame, and e and m_e are the charge and mass of an electron, respectively. Substituting the values of the constants, an expression for E_C in units of keV can be written in terms of the ring energy as follows:

$$E_C = 0.6650 E_{ring}^2 [GeV] B[T] \tag{3.4}$$

The full spectrum of light from the bending magnet enters the experimental beamline, and so energy selection must be achieved entirely via the beamline's monochromator, which will be discussed in Section 3.3.1.

3.2.5. Insertion Devices

Insertion devices are arrays of magnets contained in the straight sections of storage rings. The electrons leaving an insertion device have the same trajectory as they did upon entering; the purpose of the insertion device is entirely to produce intense synchrotron radiation for use in experiments. The nature of insertion devices means that the light produced by them can have significantly different properties than what is generated by a bending magnet. This is particularly true for undulator insertion devices, as will be shown shortly.

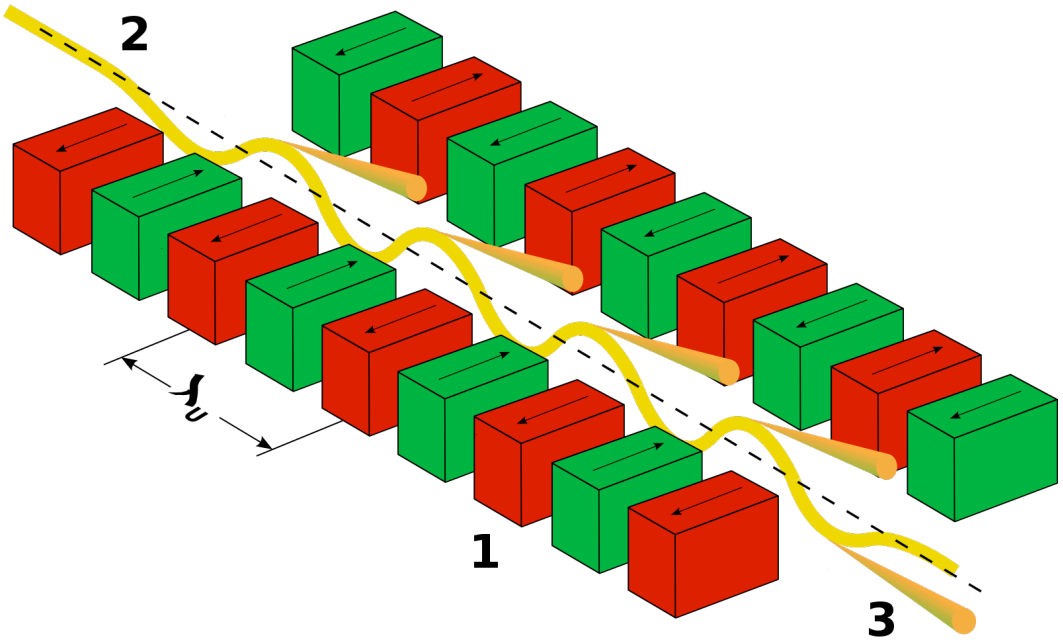

Figure 3.2: Basic layout of synchrotron insertion device.

A schematic of an insertion device [17] is shown in Figure 3.2. The permanent magnets (**1**) are arranged such that the electron beam (**2**) oscillates sinusoidally as it travels through the length of the device. As was discussed earlier, the emitted photons (**3**) are contained in a tight cone in the direction of the electron propagation as a result of the high energy of the electron beam. The two parameters that are generally used to describe an insertion device are the undulator wavelength (λ_U) and the field in the centre of the device (B_U).

While λ_U and B_U describe the design characteristics of an insertion device, on their own they are not particularly useful for quantifying the light that is produced when the device is operating. Instead, the two are often combined into a single non-dimensional magnetic strength parameter [15]:

$$K = \frac{eB_U\lambda_U}{2\pi m_e c} = 0.9337 B_U[T]\lambda_U[cm] \tag{3.5}$$

Insertion devices are classified according to the magnitude of this parameter. If K is much greater than one then the device is referred to as a wiggler; if it is approximately equal to one then it is referred to as an undulator. The distinction extends beyond simple nomenclature – the light produced by the two types of insertion devices has significantly different characteristics. In a wiggler, the sinusoidal oscillations of the electrons have a relatively large amplitude, and the emitted fan of radiation has a continuous spectrum, quite similar to that of a bending magnet, although significantly brighter. In an undulator, the oscillations are much smaller in amplitude, and the radiation cones emitted at all points within the undulator point very nearly along the axis of the device. As a result, for a particular value of K, the emitted radiation at a particular energy will undergo constructive interference, resulting in a tremendous increase in intensity over a small energy bandwidth. The relationship between the magnetic strength parameter and the radiation that is produced by the undulator is most clearly observable when described in terms of the wavelength of light that undergoes constructive interference [15]:

$$\lambda = \frac{\lambda_U}{2\gamma^2}\left(1 + \frac{K^2}{2} + \gamma^2\theta^2\right) \tag{3.6}$$

In this equation, the third term describes the energy shifts that occur off-axis as a function; in practice, beamlines are designed to minimize these effects, and so the term is usually excluded. Harmonics of the above wavelength will also undergo constructive interference; dropping the angular dependence from Equation (3.6) and rewriting it in terms of the energy of the n^{th} harmonic gives the following useful expression:

$$E_n = \frac{0.950 n E_{ring}^2 [GeV]}{\lambda_U [cm]\left(1 + \frac{K^2}{2}\right)}; \quad n = 1,2,3... \tag{3.7}$$

Selecting the desired energy from the undulator could be accomplished by physically altering any of the parameters described in Equation (3.7). Practically, however, tuning of the energy can only be easily accomplished by varying the magnetic field within the undulator causing a consequent variation in *K*. The change in the magnetic field is accomplished by altering the gap between the two sets of permanent magnets in the undulator. For any insertion device, there will be some practical limits to the possible variations in the field, and so extending the useful energy range of the device is accomplished by making use of higher harmonics; the relative brightness of the different harmonics also has an energy dependence. It should be noted that only odd-numbered harmonics are useful for experiments, as the even-numbered harmonics will have a node along the axis of the undulator, and so most of the radiation will occur off-axis [15].

3.3. Beamlines

In the previous sections, the production of synchrotron radiation via the acceleration of high-energy electrons was discussed. The production of this radiation is the responsibility of the operations group of the facility, and it can be thought of as a source of raw material for use in scientific experiments. Control of the components of the storage ring by users is limited to alteration of the gap of a particular insertion device. All further conditioning of the synchrotron radiation is performed in the beamline, which encompasses all of the equipment in the experimental area of the synchrotron facility. The two beamlines used in this study are the Spherical Grating Monochromator (SGM) [18] at the CLS and Beamline 8.0.1 (BL8) [19] at the ALS. As they are both used for soft X-ray spectroscopy, the two beamlines have similar design. The following discussion will address the general features of the beamlines, as well as including beamline-specific information where appropriate.

3.3.1. Monochromators

The synchrotron radiation that enters the beamlines from the storage ring is either broad-spectrum or "white" light, in the cases of bending magnets or wigglers, or has a few sharp intensity maxima combined with a less intense background signal in the case of undulators. In both cases, the light must in general be conditioned before it can be used in experiments. The primary processing that is performed is monochromatization, in which a particular energy of X-rays is selected, and all other energies outside of a narrow bandwidth are rejected. This step is necessary even in the case of undulator radiation, as the combined intensity due to harmonics, background signals, off-axis radiation, and the finite bandwidth of the light is significant enough to adversely affect experiments, even when the desired energy is selected by tuning the undulator gap.

Monochromatization is achieved through controlled diffraction of the incoming radiation. The design of the monochromator is largely dependent on the energy range of interest. The soft X-ray regime has a unique set of challenges, mostly related to the tendency of the photons to be strongly absorbed by most materials, which must be overcome when performing experiments. Unlike hard X-rays, soft X-ray radiation cannot travel through air, and so all beamline components must be maintained at very high vacuum levels (on the order of 10^{-9} to 10^{-10} Torr). The high absorption cross section of soft X-rays in all materials also complicates instrumentation design, as diffraction and reflection can only occur at extremely grazing angles of incidence [15].

Both of the beamlines in the current study employ grazing-incidence spherical grating designs for their monochromators. The layout of the major components of BL8 is shown in Figure 3.3 [20]; the main components of the monochromator are the three interchangeable gratings, a fixed entrance slit, and a movable exit slit. The three diffraction gratings have different line spacings that allow energies ranging from 80 eV to 1400 eV to be selected. The SGM employs a similar design, covering the energy range from 250 eV to 2000 eV.

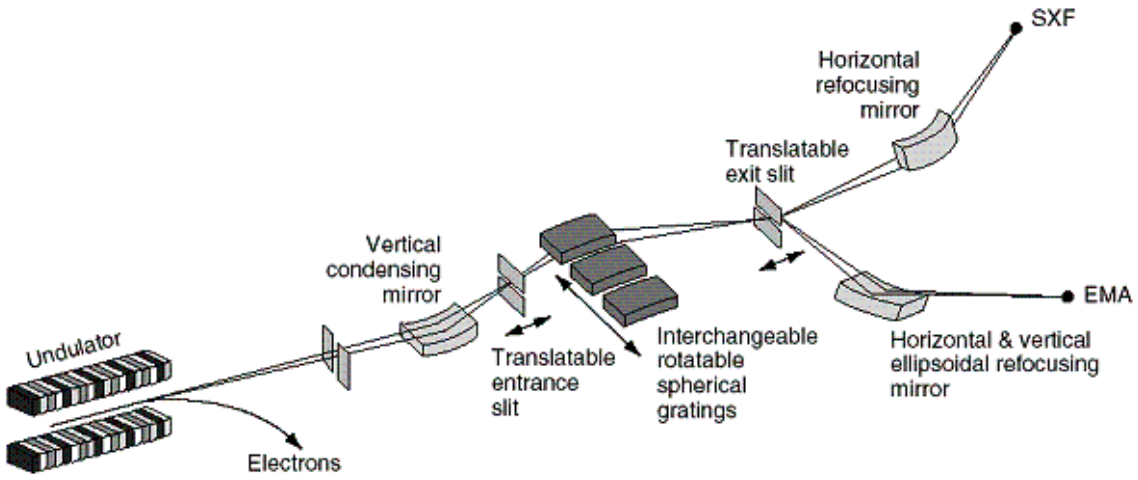

Figure 3.3: Schematic layout of the major components of Beamline 8.0.1 at the Advanced Light Source [20].

The diffraction of soft X-rays by the gratings is governed by the grating equation [21]

$$Nk\lambda - \left(\sin\alpha + \sin\beta\right) = 0 \tag{3.8}$$

where N is the line density of the diffraction grating, k is the diffraction order, α is the angle of incidence on the grating, and β is the diffraction angle. By rotating the gratings about a horizontal axis perpendicular to the longitudinal axis of the beamline, the angle of incidence of the incoming photons can be changed, and energy can be selected.

The resolution of the monochromator is quoted in terms of the bandwidth of the outcoming X-rays. There are several practical concerns affecting the resolution, most of which are beyond the control of the user for various reasons. The major limiting factor, however, is the size of the openings of the entrance and exit slits. By decreasing the sizes of these slits, the energy bandwidth can be decreased. The effect of decreasing the slit size is to increase energy selectivity by eliminating the effects of imperfect collimation, off-axis radiation from the undulator, the natural bandwidth of the undulator radiation, imperfections in the monochromator gratings, and other non-ideal properties by decreasing the acceptance angles at the entrance and exits of the monochromator.

Beyond the relation between the slit location and the selected energy, the position of the slits has an important role in the focusing of the soft X-rays. It has been shown that for spherical diffraction gratings of constant line density, optimal focusing of the X-rays is achieved when the slits and gratings are arranged such that they obey what is known as the Rowland circle condition. In this simple arrangement, the two slits and the grating are located along a circle having a radius equal to $R/2$, where R is the radius of curvature of the spherical diffraction grating, with the grating surface being tangent to the circle. The precise location of the elements along the Rowland circle is varied such that they obey the diffraction equation.

The other elements shown in Figure 3.3 are intended to focus and direct the X-rays to the experimental endstation. Because of the high absorption coefficients, it is desirable to have the soft X-rays come into contact with the fewest possible optical elements. As such, there are mirrors to condense the light in the vertical direction as it enters the monochromator, and in the horizontal direction after it exits. This arrangement produces a spot approximately 100 μm high and 50 μm wide at the sample.

The focusing at the SGM is different: there are two horizontal mirrors and one vertical focusing mirror to direct the undulator light through the entrance slit of the monochromator. The focusing provided by these mirrors has been found to provide sufficiently well-behaved light that the monochromator entrance slit can be left open (200 μm) during measurements, with the resolution of the monochromator as a whole being governed only by the size of the exit slit. The increased photon flux provided by this arrangement helps the user obtain very high-quality data. After the monochromator exit slit, two toroidal focusing mirrors focus the beam onto the sample. The spot at the sample is approximately 100 μm high and 1000 μm wide.

The final optical element in both beamlines is a highly-transparent gold mesh that is used to measure the photon flux. When the X-rays are incident on the mesh, a photocurrent that is proportional to the number of photons is produced and recorded. This current is primarily used to normalize X-ray absorption measurements, as will be discussed in greater detail in Section 4.7.

3.3.2. Beamline 8.0.1 SXF Spectrometer

The soft X-ray emission spectra at beamline 8.0.1 are recorded using an energy-dispersive detector. The general optical design of the spectrometer is not altogether different from that of the monochromator, with three elements arranged in a Rowland Circle geometry. In this case, the three elements are the spectrometer entrance slit, one of four interchangeable spherical diffraction gratings, and a multi-channel plate detector [22]. The layout of the spectrometer endstation is shown in Figure 3.4. The sample chamber, gratings, and detector are kept under Ultra High Vacuum (UHV) conditions to increase efficiency and prevent degradation of the optical elements.

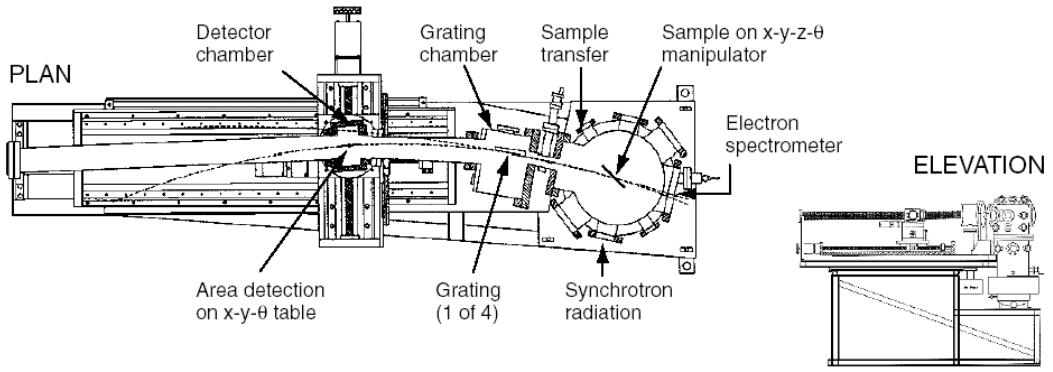

Figure 3.4: Diagram of the Soft X-ray Fluorescence spectrometer at Beamline 8.0.1 of the Advanced Light Source, available on ALS website [22]

The monochromatic synchrotron radiation enters the measurement chamber and is incident on the sample. The sample will then emit fluorescence photons – this process is described in much greater detail in Section 4.2 – some of which enter the entrance slit of the spectrometer. The size of the entrance slit is variable from 0 μm to approximately 150 μm; the size is changed to reflect the optimal balance between spectral resolution and intensity for a given sample system. The spectrometer entrance slit is treated as the source in the optical system, allowing Rowland circle geometry to be maintained when the sample position is varied.

The four selectable spherical gratings are used to measure spectra over the entire range of excitation energies that can be provided by the monochromator. In some cases there is

overlap in the energy ranges covered by the gratings, allowing further optimization of the experimental setup for a particular experiment: gratings with higher line densities will provide higher resolution, but with a trade off in efficiency.

The diffraction gratings produce an energy-dispersed image of the entrance slit – which is illuminated by the fluorescence photons from the sample – on the detector. The detector in this case is a stacked array of three multi-channel plates (MCP), each consisting of an X-Y array of biased silicon channels. An electron cascade is produced when an incident photon produces a photoelectron in a channel, and the electron pulse is amplified and recorded by a personal computer. The surface of the first MCP is coated with CsI to increase the quantum efficiency of the detector to between 10% and 20%, and a biased, transparent gold mesh is located in front of the detector to force the photoelectrons produced at the detector surface back onto the MCP.

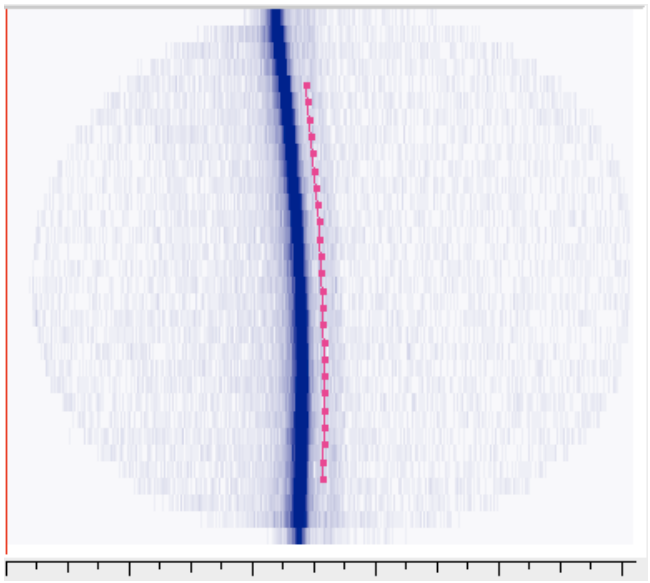

Figure 3.5: Image formed by largely monochromatic X-rays on Beamline 8.0.1 multi-channel plate detector (blue), along with line describing the shift file used in post-processing (red).

Because the diffraction gratings are spherical, the image of the spectrometer slit produced on the detector will be curved accordingly, meaning that the horizontal energy dispersion of the fluorescence photons will vary along the vertical dimension of the detector. An

example of the raw image produced on the detector by largely monochromatic photons is shown in Figure 3.5. Post-processing software is used to translate the raw image into an energy-resolved spectrum; processing this particular image would result in a spectrum dominated by a single peak associated with the blue line. This procedure will be discussed in more detail when energy calibration is described in Section 4.6.

4. Experimental Techniques

In this manuscript, soft X-ray spectroscopy is used as a general term referring to two complementary techniques: soft X-ray emission spectroscopy (XES) and soft X-ray absorption spectroscopy (XAS). These techniques provide a picture of the local partial densities of occupied and unoccupied electronic states, respectively.

Soft X-ray spectroscopy methods involve the production and monitoring of radiative transitions between ground and excited states. In a simple one-electron picture, X-ray absorption involves the interaction between a photon and a core-level electron. The photon is absorbed by the electron, which is then either promoted to a bound, previously unoccupied state, or is ejected into the continuum. If the energy of the absorbed photon is known, then it provides a measure of the energy separation between the core level and the unoccupied level. In the same simple model, X-ray emission measurements involve the detection of the photon that may be emitted when a valence electron refills the core hole that was created during the absorption process. The energy of this photon is equivalent to the energy that is dissipated during the transition, and therefore to the energy difference between the core level and the valence level. Both absorption and emission spectroscopy are governed by the final state rule [24,25], which says that the energy level of the transition is governed by the energy of the final state, meaning that the perturbations to the electronic structure caused by the presence of the core hole are significant in absorption spectra, but not in emission spectra. The following sections will describe the absorption and emission processes in significantly more detail, including the development of a more physically valid multi-electron description of the processes, which will motivate the need for the numerical models of electronic structures discussed in Section 2.4.

4.1. Near Edge X-ray Absorption Fine Structure

It is likely worthwhile at this point to begin with a note about nomenclature. A number of acronyms are currently in use to describe X-ray absorption techniques. In this thesis I will describe the technique as Near Edge X-ray Absorption Fine Structure (NEXAFS) spectroscopy, in no small part because it neatly distinguishes such measurements from

the more well-known Extended X-ray Absorption Fine Structure (EXAFS) measurements. The near-edge will be loosely defined as the area within a few eV of the ionization threshold, characterized by the presence of fine structure associated with resonant transition between ground and excited states of the material. It is this fine structure that will be analysed to provide chemical and structural information about the material being studied.

Before beginning the discussion of the basic physics involved in NEXAFS spectroscopy, it will be useful to provide a basic introduction to the measurements procedure. The monochromator is used to select the energy of the photons that will be used to excite the sample, with the energy being scanned over a region of a few tens of eV around the core ionization threshold in a series of discrete steps. When the energy of the X-rays matches the energy of a transition between a ground and excited state, they will be strongly absorbed, producing a peak in the plot of absorption vs. photon energy. Because the ground state of all such transitions is the same, the plot of absorption vs. photon energy provides an energy-resolved map of the unoccupied electronic states.

4.1.1. Interactions of X-rays with Bound Electrons

The absorption measurement begins with the interaction between the impinging photon and the bound core level electron. The electron is accelerated by the photon's oscillating electric field; the measure of an electron's likelihood to interact with a photon is given by the absorption cross section of the electron, defined as the ratio of the number of electrons excited per unit time to the number on incoming photons per unit time per unit area [1]. An in-depth derivation of the absorption cross section was presented by Stöhr in *NEXAFS Spectroscopy* [1]; the very limited description contained herein is adapted from that work.

The absorption cross section is derived from Fermi's well-known "Golden Rule," which describes the probability per unit time that a transition between initial state $|i\rangle$ and a final state $|f\rangle$ will be induced via the action of a harmonically oscillating potential given by the generic expression:

$$V(t) = \overline{V}e^{-iwt} \tag{4.1}$$

The Golden Rule can be expressed in terms of the density of final states, given by the set of final state eigenvectors $\Psi_f(E)$; the characteristics of the density of states are discussed in detail in Section 2:

$$P_{if} = \frac{2\pi}{\hbar}\left|\langle f|\overline{V}|i\rangle\right|^2 \Psi_f(E)\delta\left(E_f - E_i - h\nu\right) \tag{4.2}$$

It is, essentially, this probability that is being measured in NEXAFS spectroscopy; dividing it by an expression for the incoming photon flux and applying a first order (dipole) approximation for the potential yields a valid expression for the absorption cross section:

$$\sigma_x = \frac{4\pi^2 e^2}{m^2 c\omega}\left|\langle f|\hat{\mathbf{e}}\cdot\mathbf{p}|i\rangle\right|^2 \Psi_f(E)\delta\left(E_f - E_i - h\nu\right) \tag{4.3}$$

In this expression, $\hat{\mathbf{e}}$ is a unit vector describing the electromagnetic wave polarization and $\mathbf{p}$ represents the electron linear momentum operators. NEXAFS measurements produce a plot of the absorption cross-section as a function of energy by detecting the number of photons that are absorbed at a large number of closely-spaced excitation energies.

4.1.2. Angle-Resolved Absorption

Varying the angle of incidence in a soft X-ray absorption measurement can affect the type of information that is obtained. It is well-established that for a given excitation energy, the absorption cross-section of a material is dependent on the projection of the polarization vector onto the final-state orbitals involved in the resonant transition. In the NEXAFS experiments in this study, the incoming X-rays were horizontally polarized, and so the angular-dependent NEXAFS spectra can be used to probe the orientation of orbitals, and hence provide structural information about a molecule [1]. The origin of the angle-dependence of NEXAFS measurements can be understood in terms of the expression for the absorption coefficient developed in the previous section.

The key mathematical parameter is the relationship between the unit vector **ê** and the momentum operator **p**. The latter can be shown to be a function of the electron position **r** [1], and therefore the behaviour of the absorption coefficient is governed by:

$$\sigma_x \propto \left|\langle f|\hat{\mathbf{e}}\cdot\mathbf{r}|i\rangle\right|^2 \Psi_f(E) \tag{4.4}$$

The magnitude of the absorption coefficient for a given energy is therefore dependent on the angle between the X-ray polarization vector and the electron position vector, a quantity that can be experimentally varied by altering the angle of an ordered sample with respect to the incoming X-rays. In practice, the intensity of certain spectral features is monitored as a function of the sample angle in order to determine the orientation of the orbitals, and thus the bonds associated with them, within a macroscopic sample. This is precisely what was done in the studies of molecular semiconductor materials presented in Sections 10 and 11. The specifics of the application of this angle-resolved analysis will be demonstrated in the introduction to that study contained in Section 9.

4.1.3. Total Electron Yield

Total electron yield (TEY) measurements involve measuring the number of electrons that are ejected from a sample as a function of excitation energy. This quantity is proportional to the number of photons absorbed by the sample at a given energy. The outgoing electrons can be detected through either direct or indirect means.

In this study, all TEY spectra were measured by recording the current that was induced in the sample upon irradiation. The removal of electron from the sample as a direct or indirect result of photon absorption causes the sample to gain a net positive charge that must be neutralized by electrons provided by the sample holder. The flow of electrons from the holder to the sample results in a measurable positive current flowing out from the sample holder. Although resonant excitation from a ground state to an excited state is a charge neutral transition in which there is no primary ejection of photoelectrons, the relaxation of the excited state will lead to the ejection of secondary (Auger) electrons, and so TEY measurements can be used to detect these resonant absorptions. As the

excited states of low-Z elements primarily relax via Auger decay, TEY measurements are typically quite easy to obtain and result in high-quality spectra.

The sampling depth of TEY measurements is limited by the mean free path of the electrons that are freed in the absorption process. The electrons produced have energies that are, at most, equal to that of the soft X-rays, and in this energy range the escape depth of an electron is on the order of 10 nm [23]. This surface sensitivity can be problematic when studying reactive materials, such as the transition metal oxides discussed in Section 7.1, as surface oxidation and contamination can lead to unusable data or inaccurate conclusions. However, in certain cases the combination of TEY measurements with more depth sensitive fluorescence yield measurements can be used to provide a more complete view of the electronic structure of a material. The strength of this sort of approach is clearly seen in the study of radiation damage in glycine in Section 6 and in the study of molecular photovoltaic films described in Section 11.

Total electron yield measurements can be distorted if the sample under study is strongly insulating. This distortion is associated with the build-up of charge on the surface of the sample. When electron flow to the irradiated surface of the sample is impaired, the intensity of the electron yield measurement is suppressed, as electrons are removed from the sample more quickly than they can be replaced, resulting in a build-up of positive charge on the surface. This effect is known as sample charging. Sample charging can often be overcome by careful preparation and mounting of the samples. Thin films mounted on thick substrates are often prone to charging effects, but providing a conductive link between the film and the sample holder can often minimize these difficulties. Powder samples, particularly organic materials, are also troublesome in many cases; sample charging can usually be overcome in these materials by casting thin films onto a conductive substrate. This procedure eliminates the larger pieces of powder and reduces the length of the path that electrons need to travel from the sample holder to replace those that are removed as a result of the absorption and relaxation processes.

Sample charging effects can also be minimized by using methods that directly detect the electrons leaving the surface of the sample. These electrons can be detected using a

biased cascade detector located near the sample, and so there is no direct effect on the measurement if the rate of replacement of electrons from the sample holder is impeded.

4.1.4. Fluorescence Yield

Fluorescence yield (FY) measurements rely on the detection of photons emitted from the sample when the excited state relaxes. If no energy discrimination of the outcoming photons is employed in the detection method, then the term total fluorescence yield (TFY) is used to describe the technique. Monitoring a particular fluorescence transition or set of transitions using an energy dispersive detector is called partial fluorescence yield (PFY). The primary strength of FY measurements lies in their bulk sensitivity. The sampling depth of FY measurements is governed by the attenuation length of the X-rays in the material. This quantity varies according to the photon energy and the composition of the sample, but is generally on the order of 100 nm in the soft X-ray regime [23].

One of the advantages of bulk sensitive measurements is the ease of sample preparation. Effective measurements using surface-sensitive techniques can require complicated *in situ* preparation techniques in order to obtain a clean surface. In the study of transition metal oxides described in Section 7.1, it is seen that FY measurements can provide useful information without these requirements.

Another advantage of this bulk sensitivity is that the effective sampling depth can be controlled by changing the angle of incidence of the incoming photons. This technique is employed in the study of the molecular photovoltaic materials in Section 11, where the dual layer nature of the drop cast materials is probed.

4.2. Soft X-ray Emission Spectroscopy

The complementary technique to X-ray absorption is X-ray emission. Whereas the absorption measurements provide an energy-resolved picture of the density of unoccupied states in the material, the X-ray emission measurements probe the occupied states [26]. The first step in the emission process is the same as for the absorption measurements, namely the creation of an excited state through the interaction of a photon with a core electron, but the quantity that is measured is the photons that are emitted

when this site decays via fluorescence. Like soft X-ray absorption, emission measurements are element-selective, site-selective, and symmetry-selective. They are also inherently bulk-sensitive, except at very grazing angles of incidence. Soft X-ray emission techniques can be split into two general categories based on the choice of excitation energy. The simplest case is non-resonant X-ray emission spectroscopy, which will be referred to here as XES, in which the excitation energy is sufficient to completely remove the core electron to the continuum. The other case involves resonant excitation, in which the excitation energy corresponds to an absorption resonance, and so the electron is promoted to a bound state. Resonant excitation is used in resonant inelastic X-ray scattering (RIXS) measurements. Both resonant and non-resonant techniques will be introduced in the following sections.

4.3. Non-Resonant X-ray Emission

X-ray emission spectroscopy (XES) provides a relatively perturbation-free illustration of the occupied partial density of states; its use in the study of materials is facilitated by the extremely bright soft X-ray radiation produced in third-generation synchrotron sources, which is needed in order to overcome the inherently low fluorescence yields in lighter elements [27]. The mathematical description of the fluorescent decay of a valence electron into an unoccupied core hole is, unsurprisingly, quite similar to the model for the absorption of a photon by a core electron discussed in Section 4.1.1. The intensity of the fluorescence emission at a particular photon energy $h\nu_{\text{out}}$ is governed by a form of the Golden Rule expressed as [26]:

$$I(h\nu_{out}) \propto \nu_{out}^{3} \left| \langle i | \mathbf{p} \cdot \mathbf{A} | f \rangle \right|^{2} \Psi_{f}(h\nu_{out}) \delta\left(E_{f} - E_{i} - h\nu\right) \tag{4.5}$$

In this expression, **A** is the electromagnetic vector potential. This expression assumes that the processes of absorption and emission are decoupled, as the core electron has been promoted to the continuum, and the fluorescence occurs as a result of the decay of the excited state. However, the same assumption cannot be made in the case of resonantly excited emission, as will be shown in the following section.

4.4. Resonant X-ray Emission

For excitation on or near an absorption resonance, the excitation and emission processes are coupled, and must be described as a single inelastic scattering process [26]. This scattering process is similar to Raman scattering in the optical or hard X-ray regime, and spectroscopy employing the technique in the soft X-ray regime is usually referred to as resonant inelastic X-ray scattering (RIXS). The processes involved are described by the Kramers-Heisenberg formula [28,29]:

$$I\left(h\nu_{in},h\nu_{out}\right) \propto \sum_{f}\left|\sum_{m}\frac{\langle f|\mathbf{p}\cdot\mathbf{A}|m\rangle\langle m|\mathbf{p}\cdot\mathbf{A}|i\rangle}{E_m - E_i - h\nu_{in} - i\frac{\Gamma}{2}}\right|^2 \cdot \delta\left(E_f + h\nu_{out} - E_i - h\nu_{in}\right) \qquad (4.6)$$

In this expression, $|i\rangle$ is an initial state with energy E_i, $|m\rangle$ is an intermediate state with energy E_m, $|f\rangle$ is the final state with energy E_f, and Γ is the element-specific lifetime broadening of the intermediate state. The lifetime broadening term is necessary mathematically to prevent the equation from becoming infinite when the excitation energy exactly corresponds to a resonant absorption transition, and in terms of observable parameters it describes an inherent resolution limit for soft X-ray emission spectroscopy.

When exciting precisely on-resonance, RIXS effects will occur at the same time as regular fluorescence processes, although some site-selectivity or other effects may be observed [26]. This sort of measurement is better described as RXES (resonantly-excited XES), rather than RIXS. The RIXS processes that give rise to energy loss features in spectra are dominant when exciting pre-resonance, although their intensity decreases rapidly as the excitation energy moves away from the resonance energy.

Usually, a NEXAFS spectrum is measured prior to the RIXS or RXES measurements in order to determine the appropriate excitation energies from the location of the absorption peaks. Separating RXES from RIXS processes requires careful data analysis, and both processes can provide interesting insight into the electronic structure of a material. XES (both regular non-resonant XES – or NXES – and RXES) provides a relatively

unperturbed depiction of the partial density of occupied states, while the energy loss features seen in RIXS spectra can give information about several fundamental properties such as charge transfer and electron band structure. RIXS analysis generally involves subtracting the excitation energy from the energy axis of the measured spectrum; if a peak due to elastically scattered radiation is present in the spectrum – as is often the case – it will occur at the 0 eV location and all spectral weight will occur at negative energies on the axis. When an entire set of RIXS spectra is treated in this manner and plotted, it is said to be displayed on an energy loss scale. Any feature that occurs at a consistent energy loss location on the energy loss scale is assumed to arise from a RIXS process, because it tracks the excitation energy. The location of features associated with the XES will change location when displayed on the energy loss scale, they are generally better analysed on the scale of their fluorescence energy.

4.5. Selection Rules and Labelling Conventions

Both soft X-ray absorption and soft X-ray emission spectra are governed by the dipole selection rules. These rules place limits on the excited states that can be created via the absorption of a photon in absorption measurements, and the excited-state decay paths that can result in the emission of photons. The dipole selection rules are described in terms of the allowable changes in the various quantum numbers, and are summarized in Table 4.1.

Table 4.1: Dipole selection rules for soft X-ray spectroscopy in single-electron notation.

Quantum Number	Selection Rule
Δn	(not constrained)
Δl	± 1
Δs	$= 0$
Δj	$= 0$ or ± 1
Δm_j	$= 0$ or ± 1; m_j=0 to m_j=0 are forbidden if Δj=0

These selection rules mean that only certain electronic states contribute to the measured spectra, and so the measurements are not indicative of the total density of states but rather the partial density of states. In general, absorption and emission measurements involving excitation of a particular core level will involve transitions to excited states of only one

type – for example, measurements of carbon spectra in the soft X-ray regime always involve transitions between *1s* levels and *2p*-like states – and the spectra are labelled according to the identity of the core level, with no explicit reference to the type of states that are actually being studied. Soft X-ray absorption spectra are most often described with atomic notation, using the quantum numbers of the core electron, in the format nl_j, and this is the format that will be used throughout this manuscript (although the *j* will be excluded from the notation of *1s* levels, as there is no ambiguity). Emission spectra use X-ray notation, which, for historical reasons, denotes excitations from particular core levels with a capital letter denoting the principal quantum number, along with a subscript that increases with the total angular momentum of the level. Occasionally in this manuscript, the complementary XES and NEXAFS spectra of a particular sample will be collectively described as, for example *K*-shell absorption and emission, denoting the complete set of measurements involving the creation of a *1s* core level. The notation used to describe several relevant absorption and emission edges is summarised in Table 4.2.

Table 4.2: Notation used in soft X-ray spectroscopy

X-ray Notation	Atomic Notation	Quantum Numbers		
n_m	nl_j	n	l	j
K	$1s$	1	0	1/2
L_1	$2s$	2	0	1/2
$L_{2,3}$	$2p_{1/2,3/2}$	2	1	1/2, 3/2
M_1	$3s$	3	0	1/2
$M_{2,3}$	$3p_{1/2,3/2}$	3	1	1/2, 3/2
$M_{4,5}$	$3d_{3/2,5/2}$	3	2	3/2, 5/2

4.6. Energy Calibration

When soft X-ray absorption and emission spectra are measured, the energy of the photons that leave the monochromator and the photons that enter the spectrometer cannot be directly determined, and so there is an inherent degree of uncertainty in the measured energy scales of the emission and absorption spectra. The photon energy is determined mathematically from a number of fixed and variable parameters of the beamline. Particularly, the positions of the diffraction gratings in the monochromator and

spectrometer relative to the slits and detector are used to elucidate the energy of the photons.

In theory, if the position of every optical element of the beamline was precisely known, then the energy of all photons that contribute to the measured absorption and emission spectra could be determined with a level of accuracy that would make further processing of the measured spectra unnecessary. However, all of the mechanical systems that control the movement of the various optical elements and the monitoring systems that determine the accuracy of their positioning have a margin of error associated with them, meaning that the inputs to the grating equation – or more accurately, a lookup table derived from the equation – will depart slightly from reality, and so the energy values obtained will be correspondingly affected. In addition to the uncertainties involved in accurately and repetitively positioning the moving optical elements, there may be changes in the positions of optical elements assumed to be fixed, such as the entrance slit to the soft X-ray spectrometer, that will not be reflected in the calculated energy values. As a result, special experimental procedures and a degree of post-processing are required to accurately calibrate the spectra.

The general procedure for calibration is to measure the spectrum of a known reference sample along with the spectra of the samples being studied. The spectrum of the reference sample is then examined and, if necessary, shifted such that the positions of prominent spectral features align with accepted values. This procedure is imperfect in that the accepted energy values in the reference spectrum are subject to the same uncertainty as were the experimental results. This is an inherent problem with X-ray spectroscopy, however, and the procedures described will at least provide a consistent calibration that will enable data from multiple experiments to be compared.

4.6.1. Calibrating NEXAFS Spectra

If X-ray absorption spectra are measured in transmission mode, as is often the case with hard X-ray absorption, then the spectrum of a reference sample can often be recorded simultaneously, and so each measurement will have a mechanism for internal calibration. Unfortunately, transmission mode absorption measurements are rarely practical in

experiments using the soft X-ray regime, and so reference spectra must be measured separately. This procedure assumes that the positioning of the monochromator's optical elements is reproducible over the small range of motion that is required for multiple consecutive scans of the same energy region, or at least the uncertainty in the positioning for each step is random and not progressive and will not result in a systematic variation between measurements. In practice, this has proven to be a reliable assumption at the facilities used in this study over the relatively small energy ranges associated with soft X-ray absorption spectra.

The details of the reference samples used to calibrate the C, N, and O *1s* NEXAFS and $K\alpha$ XES spectra are given in Table 4.3. In general, it has been found that at the SGM beamline at the CLS and BL8 at the ALS, the positions of the NEXAFS spectra are very reproducible and close to the tabulated reference values. As a result of the small energy shifts – typically less than 0.5 eV – that are required to bring the measurements into agreement with the tabulated values, a linear energy shift provides a sufficiently accurate correction to the energy axis. This method would be insufficient, however, if either the energy range of the spectrum or the required shift were very large, in which case the measured data points would need to be reinterpreted by applying a mathematical correction to the assumed position of the diffraction grating and reinterpreting the energy axis of the measured spectra subject to this correction. This procedure will be discussed in more detail in the following section, as a similar procedure has proven to be necessary for the accurate calibration of XES data.

Table 4.3: Reference samples for NEXAFS and XES calibration

Element	Reference Material	NEXAFS Peak Position (eV)	XES Peak Position (eV)	Reference
Carbon	Highly-Oriented Pyrolytic Graphite (HOPG)	285.5	277.0	[30]
Nitrogen	Hexagonal Boron Nitride (h-BN)	402.1	394.7	[31]
Oxygen	$Bi_4Ge_3O_{12}$ (BGO)	532.7	526.4	[32]

4.6.2. Calibrating XES and RIXS Data

The general concept of energy calibration via comparison with the spectrum of a known reference sample applies when analyzing emission data as it does when analyzing absorption data. It has become clear, however, that applying linear corrections to the measured energy axes of the measured emission spectra is not sufficient for proper calibration, for a number of reasons related to the design of the soft X-ray spectrometer.

As was described in Section 3.3.2, the energy-dispersed X-rays that form an emission spectrum are eventually incident on the multi-channel-plate detector, and the detector image is processed, converting the spatially resolved intensity into an energy-resolved spectrum. The calculations involved in this conversion are based on the grating equation (3.8), and so the variable parameters are those that describe the geometry of the optical system for a given experiment. The user interface software for the soft X-ray spectrometer at BL8 was designed in such a way that it could be used to view completed spectra and also to alter the parameters that translate the image from the detector into a spectrum, allowing the "true" geometric parameters to be determined by optimizing the shape of a reference spectrum, and then applying these parameters to the other spectra in the data set.

The main parameter that is used to interpret the detector image is the central energy to which the detector is set. This energy is set prior to the measurements, and most of the errors in calibration stem from differences between the ideal positions of the grating and the detector and where they truly are when the spectra are measured. After the measurement, the value of the central energy can be changed, and the detector image reinterpreted as if the spectrometer had actually been set to this particular energy. By systematically varying this parameter until the position of the reference peak in the spectrum occurs at the proper energy, the value of the central energy that corresponds to the actual position of the spectrometer during the measurement can be determined. In addition to the angles that relate the positions of the entrance slit and the detector to the diffraction grating, an additional parameter is the angle between the detector normal and the Rowland Circle radius. If the positions of two peaks in the reference spectrum are

known, then these two parameters – the detector position and the detector angle – can both be optimized and extremely reliable calibration can be obtained.

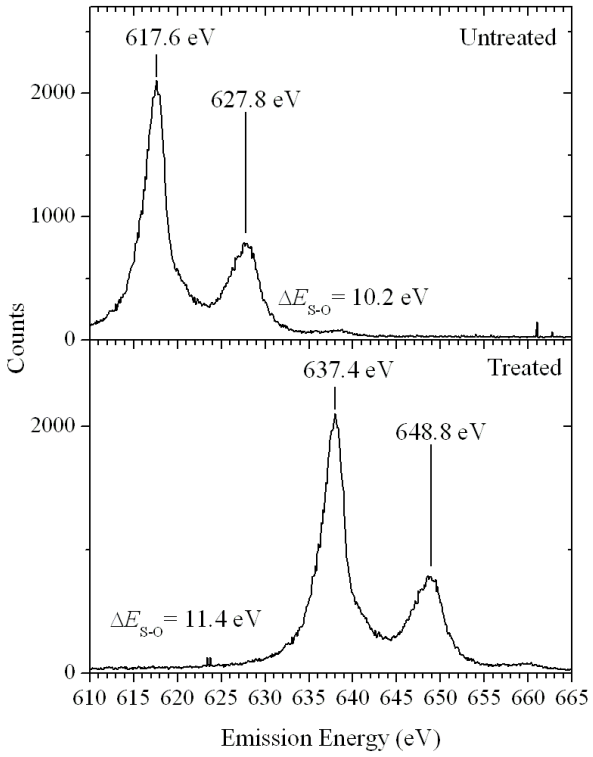

Figure 4.1: Calibration of Mn $L_{2,3}$ XES of Mn metal reference sample, showing the effects of grating and detector angle-based calibration.

Transition metals are ideal calibration samples, because they have two peaks of known energy, allowing two parameters to be optimized. Figure 4.1 shows the raw Mn $L_{2,3}$ XES spectrum in the top panel, and comparison of the locations of the peaks to accepted values [33] shows that not only is the spectrum shifted, it is distorted. The evidence for distortion lies in the value of the spin-orbit splitting between the peaks, which diverges from its ideal value of 11.4 eV by a considerable margin. If only a linear shift were applied, this disagreement would not be corrected, limiting the trustworthiness of the spectrum. Changing the value of the central detector energy from 625 eV to 645.8 eV brings the spectrum into close agreement with the tabulated values for both emission peaks, and the adjustment of the detector angle from 2.0° to 2.3° completes the

calibration. This particular reference measurement was used to calibrate a series of Mn $L_{2,3}$ RIXS spectra, and the effectiveness of the calibration technique can be observed in Figure 4.2, noting the excellent agreement between the positions of the elastic peaks in the RIXS spectra with the corresponding excitation energies marked on the absorption spectrum in the upper panel. In the absence of multiple naturally occurring peaks in an emission spectrum, elastic peaks in the spectra can be used to calibrate the data.

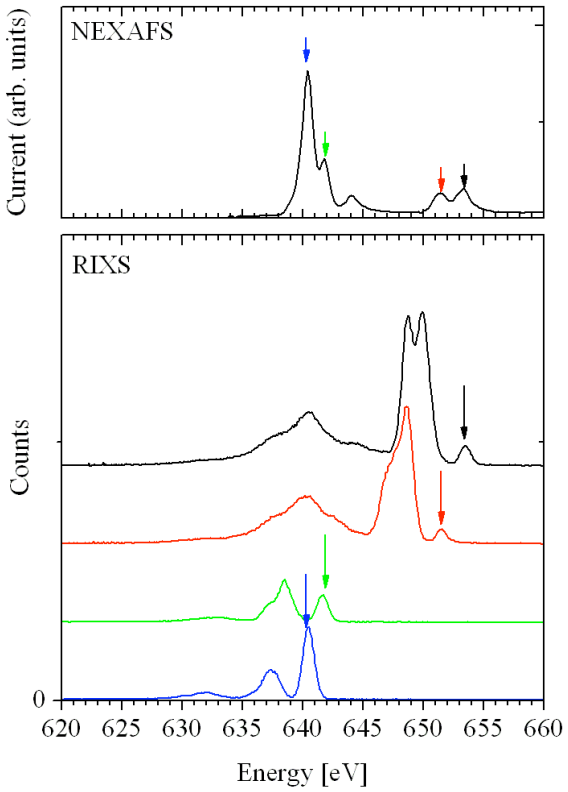

Figure 4.2: Comparison of calibrated Mn *2p* NEXAFS and $L_{2,3}$ RIXS showing agreement between the positions of the peaks due to elastically scattered radiation in the emission spectra and the energies used for excitation, which are indicated by the arrows on the NEXAFS spectrum.

4.7. Normalisation and Background Subtraction

In NEXAFS studies, the measured signal, whether recorded in electron yield or fluorescence yield modes, is a function of both the absorption coefficient of the material

and the number of photons that are incident on the sample. As it is the former quantity that is of interest, the influence of the latter quantity must be accounted for before any meaningful analysis of the data can be performed. Normalisation of the measured NEXAFS spectra is necessary to correct for variations in the incoming photon flux as a function of time or energy. The variations can arise from a number of things, including fluctuations in the ring current, variations in the behaviour of the various optical elements as the energy or angle of incidence of the light is changed, and contamination of the optical elements resulting in absorption of the synchrotron radiation between the undulator and the sample chamber.

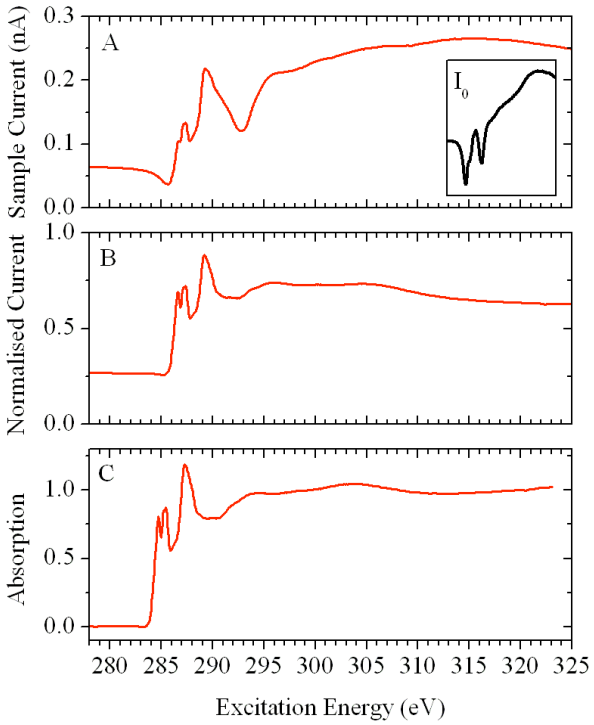

Figure 4.3: C *1s* total electron yield spectrum of organic semiconductor 4(HPBT), measured at the SGM beamline at the CLS. Panel A shows the raw TEY signal; the raw Au mesh current is plotted over the same energy range in the inset. The middle panel shows the TEY signal normalised to I_0. Panel C shows the fully-treated spectrum.

As was briefly mentioned in Section 3.3, the final optical element that the synchrotron radiation encounters before it is incident on the sample is a highly-transparent gold mesh. Because the Au absorption resonances that fall within the soft X-ray regime have very low absorption coefficients, the photocurrent produced in the Au mesh as a function of excitation energy provides an effective measurement of the relative intensity of the photons passing through the beamline during the NEXAFS measurements. It is important that this mesh be as free from contamination as possible, because contamination by any substance with resonant absorption transitions in the energy region being studied will lead to significant errors in the measured photocurrent – usually denoted I_0 – and the normalization procedure will result in distortion of the measured spectrum. At both of the beamlines used in this study, the Au mesh is periodically refreshed using a Au evaporator. However, evidence of the contamination of the Au mesh can be seen in several of the spectra in Sections 10 and 11; examples of the contaminated and uncontaminated mesh currents are contained in APPENDIX D.

In many cases, it is also useful to subtract nonuniform background signals and normalize the spectra such that the edge jump – the change in absorption intensity from well below the absorption threshold to well above the threshold – is a uniform height. Performing this post-processing of the measured spectra facilitates comparison between spectra. It is an essential first step when performing principal component analysis, such as in the study of radiation damage in glycine described in Section 6. The changes in the shape of a C *1s* NEXAFS spectrum as a result of the normalisation and background subtraction are illustrated in Figure 4.3, showing the raw sample current, the spectrum that has been normalized to the Au mesh current (shown in the inset), and finally the spectrum as it appears after background subtraction and edge jump normalisation were performed using the Athena software [34] and the spectrum was calibrated using the HOPG reference spectrum.

4.8. Principal Component Analysis

Principal component analysis (PCA) is a numerical technique that uses single value decomposition to determine the number of independent contributions to a data set. When a series of spectra taken at a particular edge are input to the PCA routine, the output is a

set of eigenvectors equal to the number of input spectra. PCA requires as input a series of *m* spectra, each having *n* data points. The spectra are placed in an *n*x*m* matrix, here designated as **A**. This matrix is then decomposed as follows:

$$\vec{\mathbf{A}} = \vec{\mathbf{U}} \cdot \vec{V} \cdot \vec{W}^{t} \tag{4.7}$$

where **U** is an *n*x*m* matrix of eigenvectors, **V** is diagonal *m*x*m* matrix of eigenvalues, and $\mathbf{W}^{\mathbf{t}}$ is an *m*x*m* matrix of scaling coefficients. All of the spectra in the original data set can be expressed as a superposition of the individual eigenvectors. The usefulness of PCA comes from the fact that not all of the eigenvectors are needed to reproduce the spectra if they have any similarities in their compositions. Therefore, by systematically removing each eigenvector from the equation and attempting the reconstruction of the measured spectra, the minimum number of necessary eigenvectors can be determined. This number is equal to the minimum number of individual spectral signatures needed to reproduce the spectra of the measured mixtures, and therefore is equal to the number of individual components in the mixture. This proved to be extremely useful in the study of radiation damage in glycine (Section 6), as it provided a basis for determining the number of product molecules that were produced as a result of the irradiation.

Principal component analysis is a statistical analysis technique that is used in a variety of areas. It has been applied in X-ray absorption analysis of soils [35], atmospheric contaminants [35], metallic catalysts [36,37], and as a tool for identifying representative spectra and removing noise in NEXAFS spectromicroscopy studies [39].

4.9. X-ray Excited Optical Luminescence

X-ray excited optical luminescence (XEOL) is a much less common technique than soft X-ray absorption and emission, and little work has been done to provide a theoretical basis for the analysis. It has, however, proved to be a valuable technique in the analysis of luminescent materials, whether they are molecular [40,41,42] or solid state [43,44,45,46]. The procedure for measuring XEOL spectra is fairly simple: an excitation energy is chosen near an absorption edge, and the energy-resolved optical luminescence spectrum is measured for either a constant excitation energy or for a sequence of energies

as in fluorescence yield absorption measurements. Spectra recorded in photoluminescence yield (PLY) mode generally appear upside down compared to TEY or TFY measurements [41,44,46], suggesting that the luminescence processes are quenched when the excitation energy corresponds to a resonant absorption. This observation is in keeping with the explanation of the XEOL measurements that will be presented in Sections 8 and 10. The advantages of XEOL over other luminescence techniques are based on the possibilities of element-selectivity and the examination of the energy-dependence of the conversion of X-ray photons to luminescence photons. Used in conjunction with XES or RIXS and NEXAFS, it has the potential to provide a high-resolution complement to the X-ray spectra.

5. Numerical Simulations of Soft X-ray Spectra

The analysis of the soft X-ray absorption and emission spectra of molecules in this study is aided by the numerical simulation of the spectra. StoBe DFT [6,7] employs the methods discussed in Sections 2.4-2.7 to simulate the XES and NEXAFS spectra. The simulations are used to assign the various spectral features, establish the feasibility and applicability of the experimental techniques, and confirm the observations that are made in the analysis of the experimental data.

5.1. Simulation of NEXAFS Spectra

Because NEXAFS spectroscopy involves the creation of a core hole, the spectral simulation must take this perturbation into account. The potential due to the presence of the screened core hole in the structure is modelled using the transition state approximation [47], in which the core electron is replaced by a half-occupied state and the virtual orbitals are left unoccupied. The relative energies of the virtual orbitals and the oscillator strengths of the transitions between them and the core levels are governed by the initial state rule [48] meaning that leaving them empty in the calculation is justified. It will be shown in Section 5.1.3 that the transition state approximation does not provide the most accurate description of the absolute energy scale of the NEXAFS spectra, which is unsurprising given that the absence of the promoted electron from the model violates the final-state rule [24,25]. Fortunately, this shortcoming can be corrected using some simple additional calculations.

The basis sets used in NEXAFS simulations are those which were described in Section 2.7, with the exception of the addition of a much larger, higher-quality *iglo_iii* basis set [49] at the location of the site that is undergoing excitation. The density of states of the excited configuration is calculated using the self consistent field method in the same way as are ground state densities of states. After the electronic structure is simulated, the oscillator strengths of all of the transitions between the orbital containing the core hole and the virtual orbitals are calculated. The oscillator strength is expressed in terms of the excitation energy E_{EX} as:

$$Osc = \frac{2}{3} E_{EX} \left(D_x^2 + D_y^2 + D_z^2 \right) \tag{5.1}$$

Individual dipole transition moments D are described in terms of the core (φ_{core}) and destination (φ_{final}) orbitals as in the example for D_x below.

$$D_x = \left\langle \varphi_{core} \middle| x \middle| \varphi_{final} \right\rangle \tag{5.2}$$

The individual oscillator strengths in the x, y, and z directions are also calculated and saved in the *filename*.xas output file. These components of the overall oscillator strength can be used to determine the angle dependence of the NEXAFS spectrum, as will be discussed in Section 5.1.5.

5.1.1. Effective Core Potentials

In a molecule with more than one atom of a particular element, it is necessary to calculate the absorption spectrum from each site separately. As a result, it is necessary to ensure that the core hole is located on a particular atom, and because of the way in which StoBe models energy levels, some extra steps need to be taken. The core hole is modelled by altering the charge associated with a particular orbital, specified numerically according to its energy. However, if there are multiple nearly degenerate orbitals – as is the case with the core levels of different sites of the same element – the act of changing the charge associated with one of them will be sufficient to cause them to reorder in energy. As a result, it is not possible to control where the core hole will occur, as the index used to describe it will not change when the orbitals reorder, causing the core hole to move around between sites during the SCF procedure.

To ensure that the location of the core hole can be specified unambiguously, the equivalent core orbitals of the atoms of the same element are removed; an effective core potential (ECP) is used to compensate for their absence. The simplest description of this approximation is that the charge of the inner-shell electrons is combined with that of the nucleus, similar to simple Z-1 or Z-2 screening models. Additional basis set input is included to improve the model and provide a more accurate approximation of the

interaction between the core levels and the more loosely bound electrons. The remaining electrons in the system are constrained to have their correct symmetries. As an example, when the *1s* levels of a C atom are removed and a +4 ECP is employed, the most tightly bound of the remaining electrons will still behave as *2s* states, not as *1s* states.

5.1.2. Modelling Open Shell Systems

The calculation of open shell systems is relatively simple with StoBe. Each spin channel is treated separately; there is no included modelling of the quantum mechanical interaction between the channels, except for that which is included in the exchange-correlation functionals. The procedure is identical to that which is used for closed shell systems, save that the multiplicity must be changed from one to two, and separate calculations for each spin channel must be performed. By default, StoBe will place the unpaired electron in the alfa channel; this must be kept in mind when specifying the electron configurations. Placing the core hole in the appropriate beta orbital will probe the transitions in the electron-deficient channel; the lowest energy feature of the calculated spectrum will generally be modelled by this calculation. The *filename*.xas output files resulting from each calculation must be stored, broadened, and calibrated separately and superimposed into a single spectrum when the data are displayed.

5.1.3. Energy Calibration

In order to accurately describe the relationships between the absorption spectra of nonequivalent sites in a molecule, extra calculations must be performed to aid in energy calibration. The transition state approximation gives the best results for the calculated intensities and relative energies of the features in the NEXAFS spectrum, but it does not provide the most accurate and consistent absolute energy scale. To rectify this shortcoming, a more accurate description of the relaxation effects that occur upon excitation is needed [50].

The X-ray absorption transition can be described as:

$$E_0 + h\nu = E^* \tag{5.3}$$

where E_0 is the ground state of the molecule, E^* is an excited state, and $h\nu$ is the energy of the incoming photon. In the transition state approximation, the excited state, E^*, contains a half-occupied core level and completely unoccupied virtual orbitals. As was discussed above, this approximation does not reflect a true state that occurs during the absorption process. To give a better description of the relaxation effects, a completely empty core state is introduced along with an extra electron in the lowest unoccupied orbital. The total energy of this system is the lowest value of E^*, and when the ground state energy – the second extra calculation – is found, it can be used to determine the energy of the lowest XAS transition. With this information available, the spectrum calculated in the transition state is then shifted so that the lowest energy transition occurs at the appropriate energy.

The modifications of the input files that are necessary for this procedure are minor. To calculate the energy of the first excited state, the number of electrons in the system is increased by one, and the occupancy of the core level is changed to zero as compared to 0.5 in the transition state calculation. The rest of the input file is identical to that which is used for the transition state calculation. An example of the changes that need to be made to the input file is included along with the NEXAFS input file in APPENDIX A. The ground state calculation also requires only small modifications; in this case the occupations are not specified. The total energy of the state is found in the output file directly after the last step of the SCF procedure.

It is important that, except for the changes described in the previous paragraph, the parameters in the input files remain the same as for the transition state calculation. It is necessary to perform a separate ground state calculation for each nonequivalent site in the molecule, because the transition energies must be determined in the presence of the effective core potentials used in the absorption calculations. The basis sets must also be identical, because the total Kohn-Sham energy of the system is affected by the number of basis functions. Because the site of the excitation is represented by a larger *iglo_iii* orbital basis set, as well as having the large, diffuse augmentation basis set in place to describe the unoccupied orbitals, the ground state energies of the various sites will generally differ in the StoBe calculations; although this of course does not reflect the physical reality of

the system. This discrepancy is one of the factors that necessitate the correction described here, as it is also present in the transition state calculations.

In the case of open-shell systems, the correction must be applied to each spin channel separately. Correct energy calibration can lead to shifts on the order of one eV in the relative excitation energy scales. The total number of calculations needed in this case is reduced by one due to the fact that the ground state electron and basis set configuration is the same in each case.

5.1.4. Broadening NEXAFS Simulations

The broadening scheme that is applied to the simulated spectra can have a significant effect on the resulting lineshape, and so it is important to adhere to a standard procedure and also to keep in mind that the broadening is meant only to improve the visual agreement between the simulation and the measurement. Comparisons between the simulations and the measurements should be based on the relative energy positions of the features, with relatively little regard given to whether or not peak ratios and other broadening-influenced factors are in agreement.

The spectra in this study have been broadened with Gaussian functions with widths that vary as a function of energy. The sharp, near-edge resonance features below the ionization threshold are broadened with relatively narrow functions, typically in the range of 0.2-0.5 eV depending on the absorption edge in question. The high-energy shape resonances are convoluted with much broader functions, typically ranging from 4-6 eV. Near the ionization threshold, the widths of the Gaussian functions increases linearly from the sharp below-edge functions to the wide above-edge functions. It is necessary to include this region of transitional broadening so that the high intensity near edge features do not inadvertently overlap with the broad high-energy features. The transitional region must therefore be at least as wide as the sum of the full-width at half-maximums of the Gaussian functions at the boundaries of the region. A sample broadening file is included in APPENDIX C.

5.1.5. Simulating Angle Resolved NEXAFS

Simulating the angle-dependence of NEXAFS spectra using StoBe is rather simple, and it is done after all of the intensive calculations are complete. The angle resolved oscillator strengths are tabulated along with the overall oscillator strength in the *filename*.xas file, and these can be selectively included in the broadening routine to produce the angle-dependent NEXAFS spectrum. The direction of the incoming photons relative to the cartesian coordinates of the input atomic structure are specified in terms of two angles, and the broadening routine weights the individual *x*, *y*, and *z* contributions accordingly. This procedure is made much easier if the atomic structure coordinates of the original input file have been aligned as well as possible with the cartesian axes, but this is not imperative. An example of an angle-resolved broadening file is included in APPENDIX C.

5.2. Simulating Soft X-ray Emission Spectra

The simulation of XES spectra using StoBe is considerably simpler than the simulation of NEXAFS spectra, owing largely to the absence of a core hole in the model. The emission spectra are assumed to reflect the ground state of the molecule, with the core level refilled. The effects of the valence hole on the energy and relative intensities of the transitions are assumed to be minimal and are ignored. As such, the procedure for calculating the XES spectrum of a molecule is the same as for a DOS calculation; it requires only additional keyword input to calculate the oscillator strengths of transitions into specified core levels. A sample XES input file is included in APPENDIX B. For XES simulations, there is no need for the use of ECPs or for the large diffuse basis functions that are used to model the high-energy unoccupied states in the NEXAFS calculations.

6. Radiation Damage in Glycine

The damage that occurs when amino acids are subjected to intense soft X-ray radiation is a matter of concern to both the medical and physical chemistry communities. Understanding the mechanisms that lead to such damage is vital if methods to avoid or repair such damage are to be developed. There are many synchrotron-based techniques that use soft X-rays to determine structural, electronic, and magnetic properties. However, many systems including large biological molecules such as proteins and DNA are prone to radiation damage, and the effects on the obtained data cannot be neglected. Amino acids are the building blocks of proteins, and their simplicity and availability make them ideal candidates to study the effects of radiation. Glycine is the simplest amino acid, and so the effects of ionizing radiation on its structure represent the best opportunity for drawing general conclusions. The structure of the glycine zwitterion, which has an overall neutral charge but localized positive and negative charges on the N and O termini respectively, is shown below. All other amino acids are formed by attaching various chemical groups to this structure, generally as a substituent for the H on the C_α site, which is adjacent to the N.

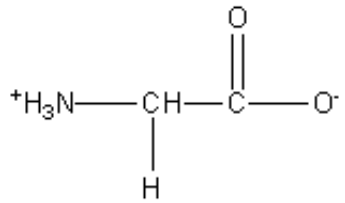

Figure 6.1: Structure of zwitterionic glycine.

Several EPR-based studies of radical formation in glycine have tackled this topic in the past [51-56], and the structures and other properties of the radicals have been modelled using density functional theory with a fair degree of success [56,57]. Electrochemical measurements of amino acids in solution have shown that the main effect of low-energy (i.e. UV) ionizing radiation is the deprotonation of the C_α site [58], which leads to the production of the radical species that are detected in EPR studies. Zubavichus *et al*. documented the effects of radiation damage on the NEXAFS spectra of several complex amino acids, employing X-ray Photoelectron Spectroscopy and mass spectrometry as

complementary experimental techniques [59,60]. Several decay mechanisms were proposed, including deprotonation and the removal of carbon dioxide; the importance of these mechanisms is reinforced in the current study. Studies of polymer materials have suggested that the primary mechanism for radiation damage is the removal of the carbonyl [61,62]. It has been found that X-ray spectroscopic techniques are effective probes of the electronic structure of amino acids including glycine [63-68].

A variety of theoretical techniques have been used in the past to model the measured near-edge soft X-ray absorption spectra of glycine. StoBe DFT [6] was used to model the spectra of glycine adsorbed onto substrates by Nyberg and Hasselström [69-72]. Gordon et al. performed NEXAFS measurements and complementary Hartree-Fock simulations to analyze the effects of the conformation of glycine and glycine peptides on the measured spectra [64]. Plashkevych et al. compared DFT simulations with measurements of glycine near-edge spectra, extending the work to include circular dichroism measurements [73]. In this study, we will present a series of NEXAFS measurements at the C *1s* and N *1s* edges showing the effects of irradiation on a primarily zwitterionic glycine sample. The identities of the product molecules will be determined through comparison with StoBe-simulated NEXAFS spectra of numerous candidate molecules, and the details of the induced reactions will be discussed.

6.1. Experimental Details

Glycine powder was purchased from Alfa-Aesar, and was used as delivered in powder form, without further purification. The sample was mounted on the holder by pressing the powder onto a freshly scraped indium foil surface. The soft X-ray absorption spectra of the C and N *1s* edges were measured at the SGM beamline at the Canadian Light Source. The monochromator resolution was approximately 100 meV, similar to the energy step size used to record the spectra (100 meV for the C spectra, 200 meV for N). The absorption spectra were measured in both total electron yield (TEY), in which absorption is monitored via measurement of the sample current, and total fluorescence yield (TFY), in which absorption is monitored through detection of photons produced through relaxation of the excited states. A new layer of gold was condensed onto the mesh used for normalisation immediately prior to our measurements to minimize the effects of

contamination on the normalization procedure. No resonance absorption peaks were seen upon examination of the measured mesh current spectrum, indicating that the mesh itself was not contaminated during the performance of the experiment. However, large dips in the intensity of the current unavoidably occur at 284.2 eV and 291.0 eV due to carbon contamination of the opticl elements found upstream of the Au mesh; these dips can sometimes lead to spectral artefacts. Although we have no reason to believe that there are any normalization problems at the C edge in the current experiment, the possibility of spectral distortion due to very low photon flux in the region around 284.4 eV, corresponding to features in the C *1s* NEXAFS spectra cannot be entirely dismissed. By examining the raw electron yield spectra, however, it was clear that a signal associated with the material being measured did indeed occur at the energy of feature *a'*, and so we carry on under the assumption that any effects associated with normalization would have no significant impact on the conclusions reached in this study.

This experiment involved using synchrotron radiation to irradiate the glycine sample and monitor the damage induced by measuring element-selective absorption spectra. The carbon NEXAFS spectra were collected at ~180 mA ring current and each scan took 416 seconds. The nitrogen NEXAFS spectra were collected at ~140 mA and each scan took 220 seconds. The π*-region-only scans for the N edge were measured at ~130 mA and took 49 seconds. A new spot on the sample was measured for each set of measurements; and all of the spectra for a given edge were measured successively, except where otherwise noted. This procedure allowed the effects of radiation damage to be studied as a function of time and radiation dose. Unfortunately, several factors make it difficult to estimate the radiation dose, particularly the variable intensity of the X-rays at each energy step: when the excitation energy is stepped, the undulator and monochromator do not move in a synchronized manner, leading to a temporary drop in intensity. A very rough estimate suggests that each scan delivers a radiation dose of 200-400 Gy, although it should be noted that for the purposes of this manuscript, several scans, particularly in the latter stages of the experiment where the changes occurred slowly and predictably, were omitted from the plots. The scans were repeated until a saturation of the damage effects was observed, with the last spectrum in each series measured after the monochromator

slits had been opened for five minutes, delivering an extremely large radiation dose to the material.

The absorption spectra were simulated using the general procedure described in Section 5.1. For comparison with the measured spectra the oscillator strengths were convoluted with Gaussian functions of varying widths. The C spectra had line widths of 0.6 eV (FWHM) up to the vacuum level and then linearly increasing to 4.5 eV (FWHM) over the next 10 eV; the N spectra had line widths of 0.6 eV (FWHM) up to the ionization potential and then linearly increasing to 5.5 eV (FWHM) over the next 10 eV The geometry of the zwitterionic α-glycine was taken from the experimental findings of Langan *et al* [75]; all other geometries were optimized with StoBe DFT.

The measured spectra were calibrated by comparing them to the spectra of reference samples that were measured with the same monochromator settings. Because absolute no method exists for achieving absolute energy calibration, it was assumed that the measured spectra were correct, and a uniform shift was applied to all simulated spectra (preserving the relative calculation determined using the method described in the preceding paragraphs) to bring them in line with the measurements. The simulated N spectra were shifted 1.9 eV to higher energy so that the centre of the broad resonance in the spectrum of zwitterionic glycine occurred at 407.5 eV. The C spectra were shifted 2.1 eV to higher energy so that the main carbonyl feature appeared at 290.0 eV.

Principal Component Analysis (PCA) was performed using the *exafspak* software [76] in order to determine the number of molecules that contributed spectral signatures to the measured spectra. The input to the PCA routine was the set of measured data taken at each edge, and the output is a series of eigenfunctions that are needed to reconstruct each spectrum in the dataset. By systematically testing whether an eigenfunction is necessary to the reconstruction, the minimum number of components in the data set can be determined. Although the eigenfunctions do not resemble the individual spectral components, the number of necessary eigenfunctions is identical to the number of individual contributing components.

6.2. N *1s* NEXAFS

Consecutive measurements of the nitrogen near edge absorption spectrum of glycine show a clear evolution as a function of radiation dose, particularly in the π* region of the spectra. The most significant changes are seen when the exposure time is relatively low, between the first and second spectra. This dramatic change is clearly visible in Figure 6.2. The N *1s* NEXAFS spectrum should not exhibit any π* features in the 400-403 eV range due to the absence of any N double bonding or peptide bonding. In light of the significant damage that occurs almost immediately upon irradiation, it can be assumed that this is the source of the minor features seen in this region of the first measured spectrum.

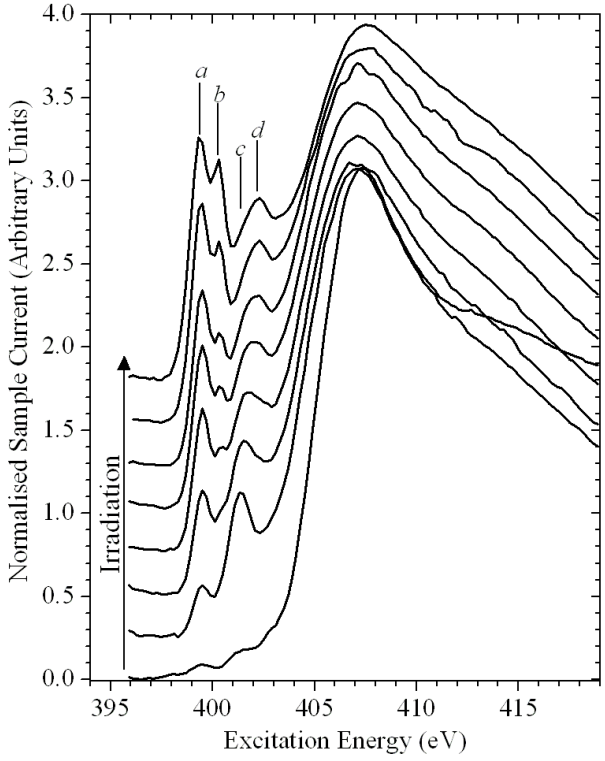

Figure 6.2: Nitrogen near-edge absorption spectra of glycine recorded in TEY mode, showing the evolution of the spectral features as a function of irradiation. The bottom spectrum represents the least exposure to soft X-rays. The background signal has been subtracted, the spectra were normalized to unity at 418 eV, and a horizontal offset has been added for clarity.

In order to confirm this assumption and to better investigate the early stages of the damage processes a second set of scans of only the π* region from 398-404 eV was performed; these scans are combined with the full-range scans in Figure 6.3. As expected, the π* features that were present at the beginning of the scans evolve upon irradiation. It is also clear from the changes in the peak ratios that there are time- or dose-dependent factors in the radiation damage process, and that several product molecules are involved.

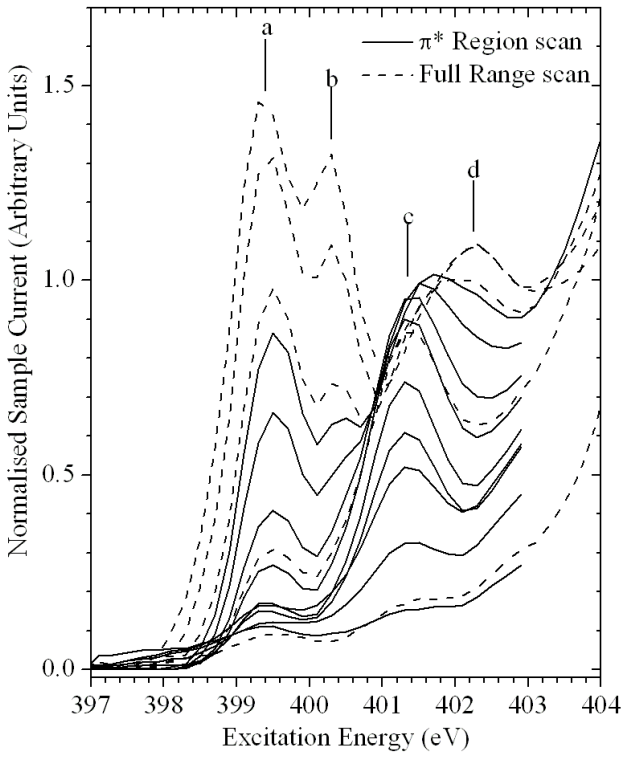

Figure 6.3: N π* region near edge absorption spectra recorded in TEY mode showing radiation damage. The dashed lines are reproduced from the full range spectra of Figure 6.2.

Some assumptions about the system needed to be made in order to analyse the data using principal component analysis. It was assumed that the irradiated glycine samples could be effectively modelled as mixtures of undamaged glycine zwitterions, which have no π* absorption features, and various product molecules. Given that intermolecular interactions have little effect on the shapes of the C and N edge spectra [64,70,74], it appears to be safe to proceed as if this were indeed the case. This assumption does not hold true for the O *1s* NEXAFS spectra, as will be discussed Section 6.4. A potential complication could occur if multiple components of the mixtures had identical spectral signatures. If this were the case, then they would not be distinguishable, and the PCA would underestimate the true number of components to the mixture. Fortunately, as will be shown shortly, the conclusions drawn from the analysis of the C and N edge spectra

are in agreement, providing a greater degree of confidence than would analysis of a single data set.

The principal component analysis of the full-range N *1s* NEXAFS spectra identified four separate spectral contributions to the data set. However, in light of the evidence that the full-range spectra do not provide an adequate description of the early stages of the radiation damage processes, the PCA was repeated using the π* region scans in Figure 6.3. The eigenfunctions are plotted in Figure 6.4.

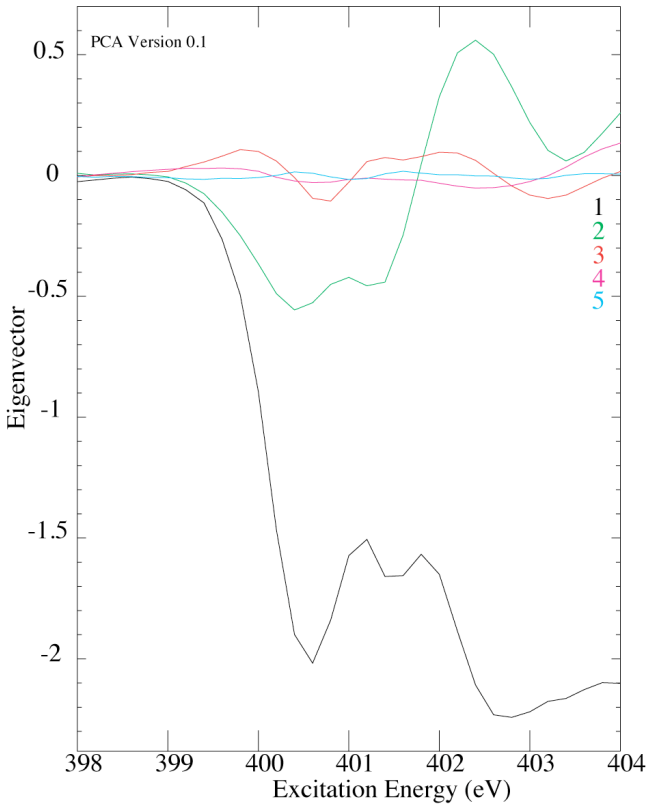

Figure 6.4: Eigenvector output of principal component analysis of N *1s* NEXAFS of π* region scans of glycine.

The contribution of eigenvector 5 is minor in Figure 6.4, but it is an essential part of the fitting routine, as it is required to reproduce the shapes of the first few measured spectra. The inclusion of six or more eigenvectors in the analysis did nothing to improve the agreement, as they displayed no regular structure. The analysis indicates that there are five separate contributions to the data set, suggesting that in addition to the glycine

zwitterion of the ground state, there are four product molecules that are stable long enough, and found in sufficient quantities, to make contributions to the spectra.

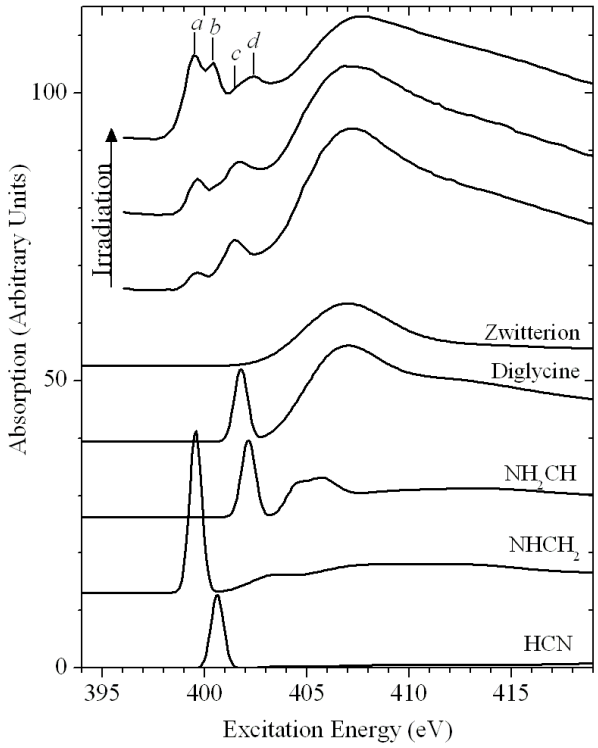

Figure 6.5: Measured N *1s* NEXAFS spectra of glycine showing increasing degrees of radiation damage compared to the StoBe DFT simulations of the spectra of zwitterionic glycine, diglycine, NH_2CH, $NHCH_2$, and HCN (absorption/5 for display purposes).

The pre-edge regions of the N absorption spectra consist of four peaks, the intensities of which vary independently over the course of the experiment, suggesting that each can be used to identify a separate component. In Figure 6.2 and Figure 6.3, peak c appears to migrate to higher energy as a function of irradiation, from 401.3 eV to 402.3 eV. This migration is an illusion, however, as close examination of the spectra show that it is in fact caused by the emergence of a competing, higher-energy peak. The proposed assignments of these peaks – as well as the other features appearing in the measured spectra – are based on the comparison with the DFT simulations. Figure 6.5 shows a

representative sample of the measured spectra compared to the simulated spectra of the proposed product molecules, and the peak energies and proposed assignments are summarized in Table 6.1. Table 6.2 shows the atom positions that were used in the StoBe DFT simulations. The numbering scheme has been kept consistent throughout, with the origin placed at the N-terminus.

Table 6.1: Proposed assignments of main spectral features observed in N *1s* NEXAFS spectra of irradiated glycine, based on models produced by StoBe DFT calculations.

Feature	Energy [eV]		Chemical Group	Model Compound
	Exp.	Theor.*		
a	399.5	399.5	Imine	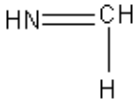 $NHCH_2$
b	400.5	400.6	Nitrile	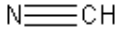 HCN
c	401.3	401.6	Peptide	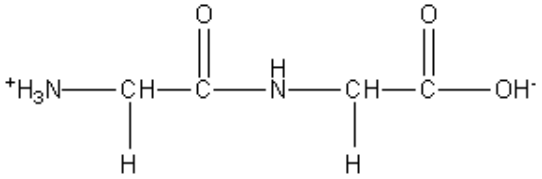 diglycine
d	402.3	402.1	Amine (surface-bound, reactive)	 NH_2CH
**after 0.9 eV shift to higher energy*				

Feature *c* corresponds closely in energy to the characteristic absorption peak of the peptide bond of diglycine (401.5 eV) [64]. Peptide formation via a condensation reaction is the proposed mechanism. Carbonyl groups have been shown to be very susceptible to radiation damage [59,60,61,62], and it appears that irradiation leads directly to the removal of an oxygen ion. Rapid peptide formation through interaction with an adjacent glycine, coupled with the expulsion of H_2O from the sample, would complete the reaction. The absorption spectrum of the N-terminus of the peptide is identical to that of the glycine zwitterion, and so feature *c* reflects the contribution of amide bonds, rather than the contribution of peptides. If only diglycine is formed as a result of irradiation,

then this distinction is academic. It is likely that larger peptides – triglycine, etc. – are formed, and so the distinction becomes important, as the proportion of N sites participating in peptide bonds will increase accordingly. The principal component analysis would not likely be able to distinguish the presence of separate contributions from diglycine and larger peptides, and we assume that larger aggregations are present in the sample. The formation of a diketopiperazine cannot be entirely ruled out, however the simulation of its absorption spectra (not shown) did not suggest that it is present in any significant quantity.

The above assumptions can in fact be generally applied to the comparison of the simulated spectra of the model compounds to the measured data. The N *1s* NEXAFS spectra of particular N-containing chemical groups will not be particularly sensitive to the nature of the extended structure to which it is attached; if the energy shift in the characteristic peak position is less than the resolution of the measurement, the presence of multiple closely-related structures would not be indicated by the principal component analysis. The set of reaction products proposed here is internally consistent, effectively reproducing all features in the measured N-edge and, as will be discussed in the following sections, C-edge spectra. However, in light of the inherent uncertainty involved, the conclusions will be restricted to the identification of the functional groups present in the sample.

The removal of the entire carbonyl would lead to the expulsion of CO_2; desorption of H_2 would lead to the formation of $NHCH_2$ and NH_2CH. The StoBe simulations of their absorption spectra produce peaks at 399.5 eV and at 402.1 eV, respectively, in agreement with the positions of features *a* and *d* in the measured spectrum.

Another possible origin for feature *c* is suggested by previous studies [77,78] in which trapped N_2 gas was found in irradiated materials. We attempted high-resolution scans of the energy region around features *c* and *d* and saw no evidence of vibrational structure that would suggest the presence of trapped N_2 gas [78]. Although we cannot rule out the presence of trapped N_2 gas in the sample, the mechanism for peptide formation above seems to give a much more plausible assignment of the origin of peak *c*.

Table 6.2: Atom positions used in DFT simulation of N and C edge NEXAFS spectra

	x (Å)	y (Å)	z (Å)
Zwitterion			
N1	0.000	0.000	0.000
C1	1.475	0.000	0.000
C2	2.040	1.416	0.000
O1	1.279	2.340	0.360
O2	3.237	1.554	-0.347
Diglycine			
N1	0.000	0.000	0.000
C1	1.492	0.000	0.000
C2	1.806	1.527	0.000
O1	5.406	1.157	0.000
N2	3.078	1.785	0.000
C3	3.881	3.003	0.000
C4	5.370	2.448	0.000
O2	6.282	3.290	0.000
O3	0.782	2.284	0.000
NH_2CH			
N1	0.000	0.000	0.000
C1	1.320	0.000	0.000
$NHCH_2$			
N1	0.000	0.000	0.000
C1	1.279	0.000	0.000
HCN			
N1	0.000	0.000	0.000
C1	1.160	0.000	0.000

Fluorescence yield measurements have depth sensitivity on the order of 100 nm at this energy – an order of magnitude larger than that of electron yield measurements – and so the spectra shown in Figure 6.6 indicate that there is a depth dependence on the composition of the damaged material. Peaks *a* and *d* are particularly suppressed in the fluorescence measurements, suggesting that the NH_2CH and $NHCH_2$ are primarily produced near the surface of the material; this may reflect the relative ease at which CO_2 can be expelled from the surface of the material, leading to decreased opportunity for recombination. The near disappearance of peak *d* in the bulk-sensitive fluorescence yield measurements is consistent with the model of a highly-reactive structure derivative isolated on the sample surface under UHV conditions. The TFY spectra indicate that the $NHCH_2$ group is not present in the bulk of the sample in any detectable quantity. The

suppression of peak *a* suggests that the imine group, represented by NH_2CH, is also more abundant on the surface than in the bulk, although the contrast is significantly less pronounced.

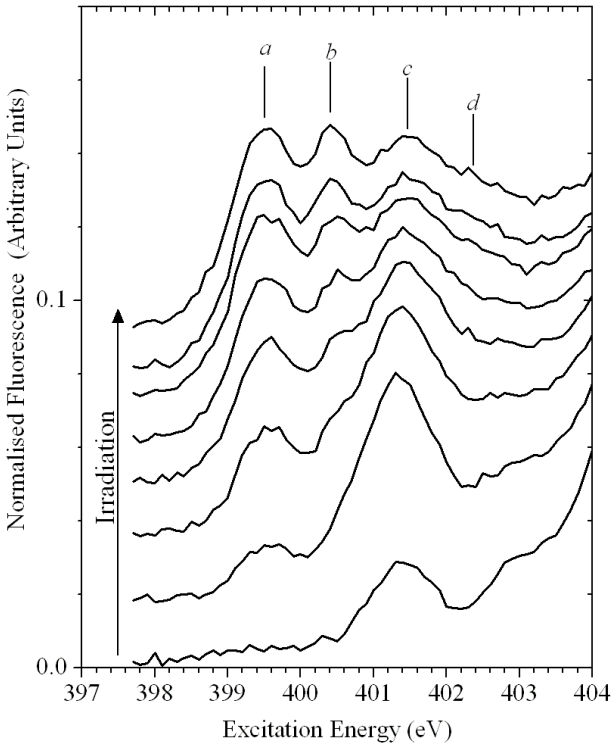

Figure 6.6: N *1s* absorption spectra measured in depth-sensitive TFY mode showing evolution of spectral features associated with increasing radiation dose.

Some of the changes in peak ratios may be due to self-absorption of the fluorescence photons, but this is unlikely to be the primary cause, as self-absorption more strongly affects intense, sharp resonance absorption features and would not explain the near-disappearance of peak *d*. The relatively late emergence of peak *b*, which is attributed to absorption by HCN, suggests that the nitrile groups may be produced via a secondary reaction involving the breakdown of one of the other products. It is also entirely possible that the peak is due to a more complex nitrile, such as NH_2CN, with a similar N≡C bond length. Although the relative prominence of peak *b* in the fluorescence yield spectra as compared to the electron yield spectra is consistent with the model of a trapped gas, we

cannot claim to have unambiguously identified the presence of HCN in the irradiated sample.

6.3. C *1s* NEXAFS

The measured C *1s* NEXAFS spectra in Figure 6.7 show the effects of the increasing radiation dose in the evolution of the spectral features. The general trend that was observed in the measurements of the N-edge spectra – that of increasing π* resonance intensity – is reproduced, although the dynamic behaviour at the C-edge is less complex. The decrease in the intensity of feature *e′* is indicative of the expected [59,60,61,62] damage to the carbonyl, providing an indirect confirmation of the conclusions drawn from the N absorption spectra. The combined evidence of the C and N absorption spectra suggest that the removal of all or part of the carbonyl group is the primary damage mechanism under soft X-ray irradiation, regardless of the specific energy of the incoming photons.

The simulated C spectra of the proposed radiation products are shown in Figure 6.8. The PCA of the C edge spectra was in agreement with the analysis of the N edge spectra, suggesting the presence of five components to the data set. The majority of the measured spectra can be adequately reproduced using only four of the eigenvectors, but modelling the final few spectra requires a fifth eigenfunction to be included. In further agreement with the modelling of the N edge spectra, the simulated C edge spectra predict resonance absorption peaks at energies corresponding to all major features in the measured spectra. There is also evidence of energy dependence in the relative abundance of the products. Compared to the N edge absorption, the intensities of the peaks associated with molecules having deprotonated N sites – especially the completely deprotonated HCN – are suppressed in the C edge spectra. This observation suggests a possible connection between the resonant absorption of photons and the nature of the induced reaction, which would imply that removal of electrons from the bonding orbitals plays a dominant role in the decomposition process. The current methods are not sufficiently quantitative to determine unambiguously whether this is the case, however, and a more directed study of the relationship between resonant excitation and the induced chemical reactions would be required to draw any firm conclusions.

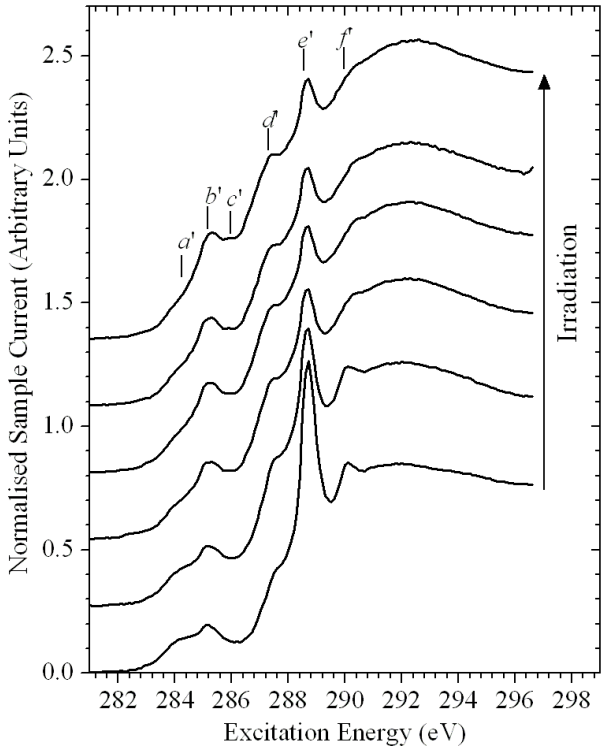

Figure 6.7: Measured C *1s* NEXAFS spectra of glycine. The least-irradiated spectrum is at the bottom, and the most irradiated spectrum is at the top. The background signal has been subtracted, the spectra were normalized to unity at 294 eV, and a horizontal offset has been added for clarity.

As somewhat of an aside, we feel that it is worthwhile at this point to discuss a matter concerning the calculated C absorption spectrum of the glycine zwitterion. Although peak *f″* is clearly associated with the spectrum of zwitterionic glycine, we must at this point discuss a small degree of uncertainty about the exact origin of the feature. As can be seen from Figure 6.8, the simulated spectrum of the zwitterion has two features, at 289.8 eV and 291.0 eV, that have the basic shape of feature *f″* and are located near it on the energy scale. In our model, it appears that the lower-energy peak in the simulation is the source of this feature, but the case could be argued either way. Although it does not have a direct bearing on the conclusions of this study, the point is worth addressing at this point, as the fit to the measured data would be improved by shifting the simulated absorption spectrum of the C_α site of the glycine zwitterion to lower energy by 0.9 eV will cause the higher-

energy of the two peaks to align with feature *f′* and also lead to an increase in the intensity in the region of feature *d′*. Varying the bond lengths and angles around the C_α site could conceivably cause such a shift in the relative energies of the two C site spectra; however, we did not wish to manipulate our results in this way, choosing rather to use the geometry that was experimentally determined by Langan et al. [75] for the spectral simulations. Also, because of the uncertainty surrounding the nature of *d′*, we have elected to leave it out of Table 6.3.

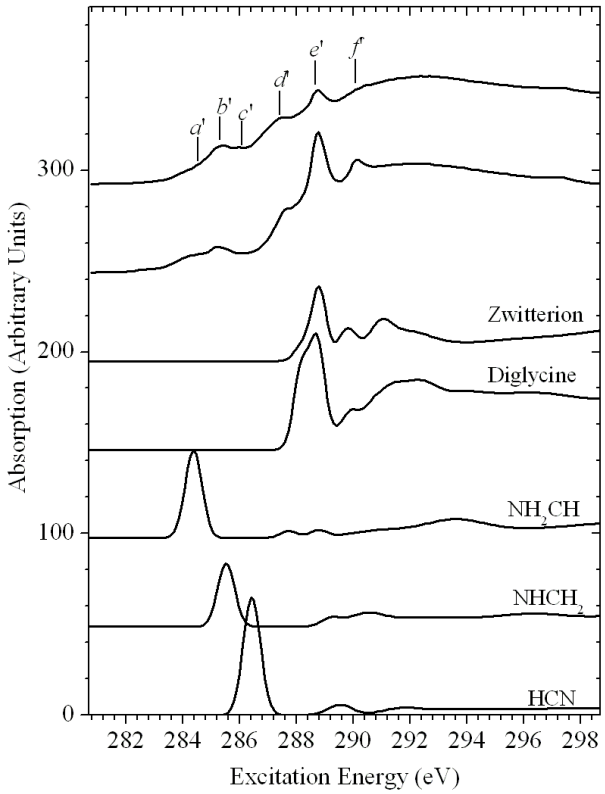

Figure 6.8: Measured C *1s* NEXAFS spectra of damaged glycine (top two spectra) compared to the StoBe DFT simulations of the spectra of zwitterionic glycine, diglycine, NH_2CH, $NHCH_2$, and HCN.

Table 6.3: Proposed assignments of main spectral features observed in C *1s* NEXAFS spectra of irradiated glycine, based on models produced by StoBe DFT calculations.

Feature	Energy [eV] (calculated*)	Assignment
a'	284.6 (284.4)	NH_2CH
b'	285.3 (285.5)	$NHCH_2$
c'	286.2 (286.4)	HCN
e'	288.8 (288.8)	glycine zwitterion carbonyl
f'	290.1 (289.9)	Glycine zwitterion
**after 2.1 eV shift to higher energy*		

6.4. O *1s* NEXAFS

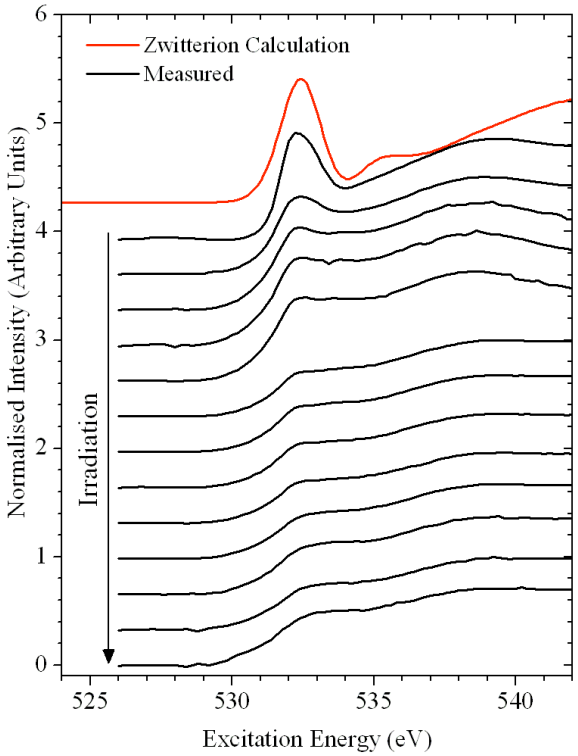

Figure 6.9: O *1s* NEXAFS of glycine showing effects of radiation damage and comparison with StoBe simulation of glycine zwitterion spectrum. A vertical offset is added for clarity.

The O *1s* NEXAFS spectra of glycine (Figure 6.9) show clear and rapid changes due to irradiation, but the nature of the changes and the inherent broadness of the O-edge measurements meant that they would add little information to the study. The spectra are presented here as supporting information, as they do agree with the results of the analysis of the N- and C-edge NEXAFS. Calibration was performed by shifting the spectra such that the energy of the main π* resonance absorption feature appears a 532.4 eV, in agreement with previously published values for solid glycine [64]. The measured spectra were shifted 4.0 eV to lower energy; the calculated spectrum was shifted 0.4 eV to lower energy.

The general shape of the simulated NEXAFS spectrum shown in Figure 6.9, particularly above 534 eV, differs significantly from that of the measured spectrum. The disagreement between the simulation and the measurement reflects previously reported experimental findings [64] that show similar differences between the O *1s* NEXAFS spectra of glycine in solid and gas phases. The use of the atomic coordinates that were determined experimentally by Langan et al. [75] precludes any possibility that the simulated spectrum will accurately reflect the experimental gas phase absorption spectra shown by Gordon et al. [64], but the similarities in the shapes of the high-energy regions of the spectra indicate that this region of the spectrum is greatly influenced by intermolecular interactions. Because the O sites are involved in H-bonding with the N sites of adjacent molecules, this observation raised concerns regarding the energy calibration of the N-edge simulations. Fortunately, there are no related shifts observed in the experimental comparison of the N *1s* absorption edges of solid and gas phase glycine, and so this was not deemed to be a matter of great concern. However, the clear and unpredictable influence of the extramolecular environment on the shape of O *1s* NEXAFS spectra does make it unsuitable for use in the current study, especially considering that there is only a single, broad π* resonance that could be used as a spectral marker.

The main radiation-induced effect is the overall decline in the intensity of the main π* absorption feature at 532.4 eV, an effect which is in keeping with a damage model focused on the complete or partial removal of the carbonyl group. The spectra in Figure

6.9 have had their background signals subtracted using Athena, but it is clear from observing the unprocessed data (APPENDIX E) that the overall amount of oxygen in the sample decreases, as evidenced by a decline in both the overall intensity of the absorption signal and by the decrease in the intensity of the absorption resonance features relative to the pre-edge (i.e. below ~530 eV) region. This is in marked contrast to the unprocessed N *1s* and C *1s* NEXAFS data shown in APPENDIX E, in which there is little change in the overall signal strength or contrast ratio, indicating that the overall concentrations of N and C in the sample remain constant over the course of the experiment. This observation supports the proposed damage processes, as most of the products retain C and N while losing O.

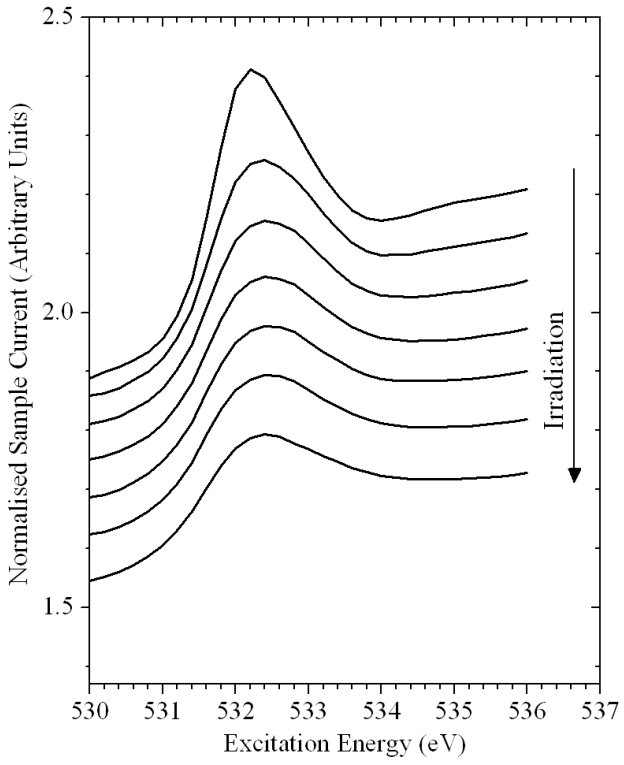

Figure 6.10: Scans of the early-onset region of the O *1s* edge of glycine showing the first stages of radiation damage.

As was observed in the N and C NEXAFS spectra, the most rapid change in the spectral lineshapes occurs between the first measurement and the second. An attempt was made to

study the early stage of the reaction using quick scans of the early onset region, shown in Figure 6.10. The scans do show the changes that occur in the early stages of irradiation, but no significant information about the identity of the product molecules can be gleaned from them.

6.5. Discussion and Conclusions

As a qualitative test of the numerical models, weighted sums of the individual components were used to reproduce the shape of three representative N absorption spectra; the results are displayed in Figure 6.11. Because the intensity of the calculated peaks is strongly dependent on the broadening scheme that is used, it is not possible to make absolute determinations of the relative abundance of each respective material, and so it must be made clear to the reader that the percentages referenced in the following discussion should be viewed as qualitative guides, reflecting no more than the order of magnitude of the relative abundance of any material. Notwithstanding this caveat, however, a few useful observations can be inferred from the fitting procedure. It is clear that, despite the prominence of the resonance absorption features in the near-edge region, the concentrations of several of the various product molecules are very small, considering the large level of energy introduced into a very small portion of the sample. For example, the HCN contributes approximately 4% to the fit made to the topmost spectrum, which had been subjected to an extremely high radiation dose in an attempt to produce a saturation of the effect. 4% HCN concentration would be a very large concentration, even given the extremely high radiation dose that this region receives, which lends further support to the presence of multiple nitriles which have similar spectra. Furthermore, no relaxation time was allowed between the irradiation and the measurement, and so it is likely that several of the product molecules would dissipate rapidly. Additional stability may be lent to the products due to the fact that they are produced in situ in a very high vacuum environment.

The simulated diglycine spectrum contributes 16% to the fit of the topmost spectrum in Figure 6.11. It is possible that that may overstate the presence of peptides in the material, because, as was previously discussed, it is likely that larger peptides are formed as a

result of irradiation. As it is not possible to determine the relative abundance of diglycine, triglycine, etc. we have used only diglycine in the analysis.

Both NH_2CH and $NHCH_2$ contribute 20% to the topmost fit in Figure 6.11. Because of the depth profile of the products that was discussed earlier, this number overestimates the contribution of the NH_2 and NH groups. Assuming that self-absorption does not have a significant effect on the relative intensities of the peaks in Figure 6.6, a better approximation of their concentrations is on the order of 10%.

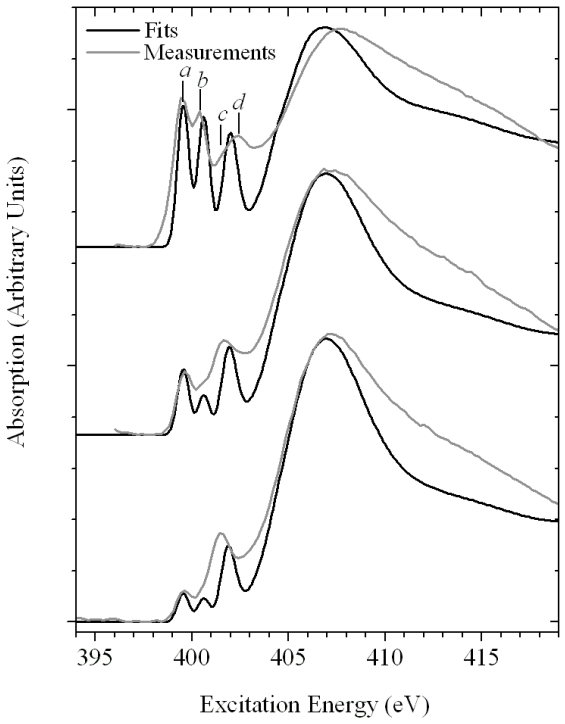

Figure 6.11: Fits produced by superposition of simulated spectra, compared with measured N edge absorption spectra of glycine

In this study, we have used the N edge NEXAFS spectra to attempt to determine the nature of the products that are produced in irradiated glycine samples. Because of the clear evolution of the spectra as a function of increasing radiation dose and the relatively few possible bonding environments for the N site, we can assign the observed features in the N edge spectra to particular chemical groups with a fair degree of confidence.

However, the analysis of the C edge spectra is inherently more ambiguous, due to the multiple non-equivalent groups in the majority of the products and to the less spectacular evolution of the measured spectra. We have therefore used the C edge spectra primarily to confirm the conclusions drawn from the analysis of the N edge spectra. The comparison of the simulated spectra of the proposed products provides a self-consistent result with the same molecules used to assign the peaks in both the C and N *1s* NEXAFS spectra. The proposed set of products is also consistent with the results of the principal component analysis, which suggested that five distinct spectral signatures were present in the measured data sets. The products included in the simulations of the spectra are model compounds that represent general classes of materials.

A large number of possible products were considered as possible contributors to the measured spectrum and were modelled in the same manner as those described above before being ruled out because they did not match the measured data. The spectra of several ionic and radical species were modelled and no evidence was found to warrant their inclusion in the proposed model. Due to the highly reactive nature of such compounds, it is unlikely that they could be stable in a solid state in sufficient quantities to be detectable. The possibility of a transition from zwitterionic glycine to neutral glycine was considered, and cannot be entirely ruled out, due to the similarity of the C *1s* and N *1s* NEXAFS spectra of the two forms.

This study utilizes soft X-ray absorption spectroscopy to monitor the radiation-induced reactions that occur in solid-state glycine in very high vacuum conditions. By analyzing the evolution of the spectra using a combination of principal component analysis and density functional theory simulations, a possible model of the damage process in terms of the chemical classes present in the sample is obtained. In agreement with previous studies of the effects of soft X-ray irradiation on organic materials, it is observed that the carbonyl group is highly sensitive to the effects of irradiation, and is largely removed from the material over the course of the experiment. Our results suggest that removal of an oxygen ion from the carbonyl group induces the formation of peptides in the sample. By comparing the surface-sensitive electron yield and the bulk-sensitive fluorescence

yield NEXAFS spectra, we conclude that removal of CO_2 from the sample occurs upon irradiation, and that it is more likely to occur near the surface of the sample.

7. HOMO-LUMO and Band Gaps

The relative positions of the occupied and unoccupied electronic levels in materials is of particular interest in materials science, as it is involved in many of a material's macroscopic properties, such as conductivity, electronegativity, optical absorption, and reactivity. There are significant differences between the gaps that characterize molecules and the gaps that characterize crystalline materials. The large number of electrons, high symmetry, and periodic structure of crystals means that the energy bands form a manifold of states, with each band varying in energy as a function of k. Molecules are much smaller, and the molecular orbital approximation suggests that the electron energy levels have discrete energies, subject to thermal broadening and other perturbative considerations.

The picture of occupied and unoccupied states provided by the combination of X-ray emission and absorption measurements can be used to provide an indication of the energy differences between the states, although there are a number of concerns to be addressed in such analysis. Most obvious is the inherent need for careful and correct energy calibration, or at the very least correct relative calibration of the absorption and emission spectra, as is described in Section 4.6. This having been accomplished, the appropriate definitions of the "top" of the valence states and the "bottom" of the conduction states is still a matter of uncertainty, as there are numerous experimental effects (particularly the limited energy resolution and the uncertainty in energy calibrations) and physical effects (most notably the effect of the core and valence vacancies in the final states, as well as asymmetric broadening due to vibronic coupling) that create uncertainty in the energy scales, most obviously through simple broadening of the states or the spectra. The influence of the core hole on the absorption measurements must also be taken into account, because of its clear effect on the relative energies of the states [24,25].

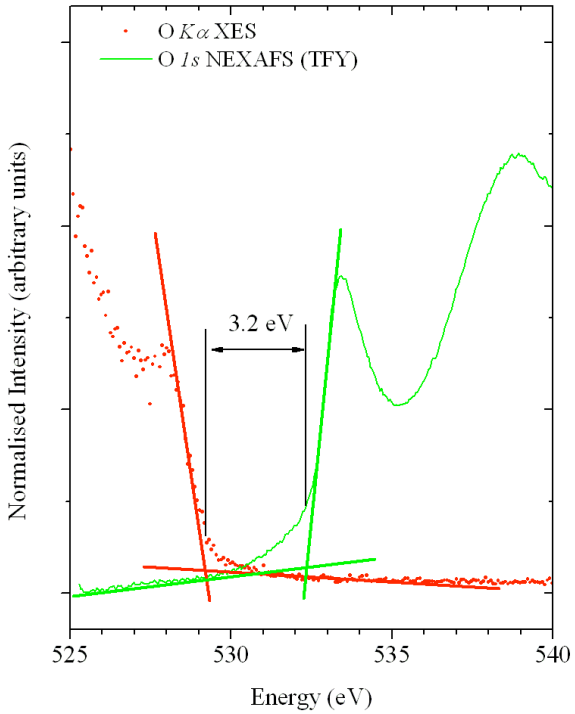

Figure 7.1: O *K*-edge XES and NEXAFS spectra of NiO, with lines drawn to illustrate the common method for band gap determination.

Generally, when the combination of soft X-ray emission and absorption spectroscopy has been used to study energy gaps in materials, the goal has been to determine the location of the onset of the valence or conduction states, the point at which the measured signal emerges from the background. This approach has been used to study such diverse materials as DNA [79,80], nanocrystalline Si [81] and CdS [82], ultrahard materials [83,84], photovoltaic chalcopyrite films [85], Si-oxynitride films [86], large molecular forms of silicon-nitride [87], and doped magnetic ZnO nanorods [88]. There are seemingly as many motivations behind the studying of energy gaps in materials as there are studies themselves. The use of the combination of XES and NEXAFS in the study of nanocrystalline materials purported to show the effects of quantum confinement which is predicted to cause function-modifying shifts in the band gap as a function of particle size [81,82]. As it is exactly this sort of property that nanotechnology seeks to exploit, experimental studies that can help refine theoretical models of such behaviour are vital.

The sudden interest in the use of non-traditional materials, such as DNA, in electronics applications can lead, on occasion, to wildly disparate accounts of the materials' properties, which may be greatly and unpredictably influenced by the sample treatment and the experimental geometry. Soft X-ray spectroscopy was used to supply a measure of the gap between occupied and unoccupied states in a bulk sample of commercially available DNA [79,80], in an attempt to reconcile the results of various seemingly contradictory studies. Some studies have made attempts to correct for the core hole effect by removing peaks at the onset of the NEXAFS spectra that they attribute to the creation of core exciton states [82, 83].

The most common way of determining the location of the edges of the energy gap is to fit straight lines to the background signal and the onset of the emission or absorption signal; the edge of the gap is said to occur at the intersection of the two lines. To illustrate this technique, it has been applied to the O $K\alpha$ XES and O *1s* NEXAFS spectra of NiO, plotted in Figure 7.1 – these spectra will be analyzed more fully in Section 7.1, where an improved method for band gap determination will be presented. The band gap that is obtained via this method is approximately 0.7 eV smaller than what has been reported previously [89], but given the uncertainties involved in all methods for determining gaps this is not in itself an indication of the inadequacy of the method. More worrisome is that the fitting of the lines to the spectra is somewhat subjective and can therefore be influenced to some extent by the experimenter. In this case, the positions of the various lines could be varied to alter the gap by 0.1-0.2 eV without causing a visible disagreement with the measured spectra. Additionally, fitting a straight line to the onset of a total fluorescence yield spectrum is complicated by the varying likelihood of RIXS processes – the probability of these processes increases as the excitation energy approaches the energy of the transition resonance [26], and so the pre-edge region can have a lineshape that does not reflect the density of unoccupied states. It will be argued in the following section that this method can be improved upon, removing some of its uncertainties.

7.1. Band Gaps of Transition Metal Oxides

A study of the O *K*-edge XES and NEXAFS spectra of several transition metal (TM) monoxides [90] resulted in a novel approach to the study of the electronic structures of these materials. Modelling these materials is complicated by the large correlation effects, the common local density approximation (LDA) approach does not produce a satisfactory model of the electronic structure of these systems; it drastically underestimates the band gaps for MnO, CoO, and NiO, for example [91]. Because of the difficulties associated with the numerical simulations, experimental studies are vital to determine various parameters and to evaluate the accuracy of numerical electronic structure models. X-ray emission and absorption spectroscopy is ideally suited to modelling the local density of electronic states, with the only major possible complication arising from the modification of these states as a result of the presence of the core hole that is created during the absorption process [24,25]. As discussed in Section 4, absorption measurements, in which the core hole is part of the final state, are more strongly affected than are emission measurements, in which the final state vacancy is in a valence state. In the case of the transition metal oxides, the O *1s* core hole created during the XAS measurements is expected to interact weakly with the TM *3d* states [92]. These states appear in the O *1s* XAS spectra as transitions into hybridized O *2p*/TM *3d* states, and so it is expected that these measurements should provide a relatively unperturbed probe of the TM DOS. Support for these assumptions comes from the comparison of the O *K*-edge absorption and emission spectra of NiO and the results of LDA+DMFT [93] density of states calculations, both of which are shown in Figure 7.2. In contrast, the Ni *2p* NEXAFS spectrum is strongly influenced by the presence of the core hole, and the broadness of the Ni $L_{2,3}$ XES spectrum makes it a poor candidate for comparison with numerical simulations.

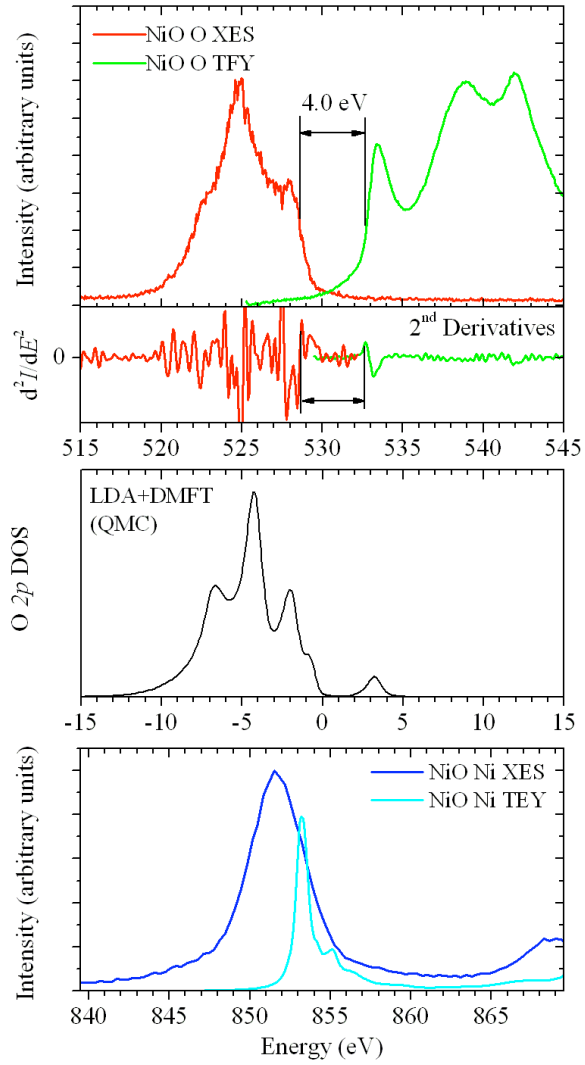

Figure 7.2: XES and NEXAFS measurements at the O *K*-edge and Ni $L_{2,3}$-edge of NiO, used to determine the band gap. Also shown is the density of states calculation performed by Dr. Jan Kuneš [93], based on the LDA+DMFT procedure.

The method that is used to determine the band gaps of the transition metal monoxides, including NiO, from the measured XES and NEXAFS spectra is relatively simple and straightforward. The second derivative of the XES and XAS spectra of a sample are plotted on a common energy scale, and the distance between the highest energy peak of the XES derivative and the lowest energy peak of the XAS derivative is determined. The peak in the second derivative does not have any special physical significance, except to

mark the location of a sudden increase in the intensity of the measured spectrum. Taking derivatives also serves as a means of removing a second-order fit of the background signal in the pre-edge region, minimizing the effects of RIXS contributions to the absorption signal in this energy region. This effect can be very clearly seen if one compares the pre-edge region of the NiO O *1s* TFY (NEXAFS) spectrum to the plot of its second derivative. For this study, the TFY measurements were used in order to avoid the effects of surface oxidation and contamination that could affect TEY measurements. The value for the band gap obtained using this method is 4.0 eV, in good agreement with the previously published value of 3.9 eV [89] and in contrast with the value that was obtained by fitting tangent lines to the background and onset regions in Figure 7.1 (3.2 eV).

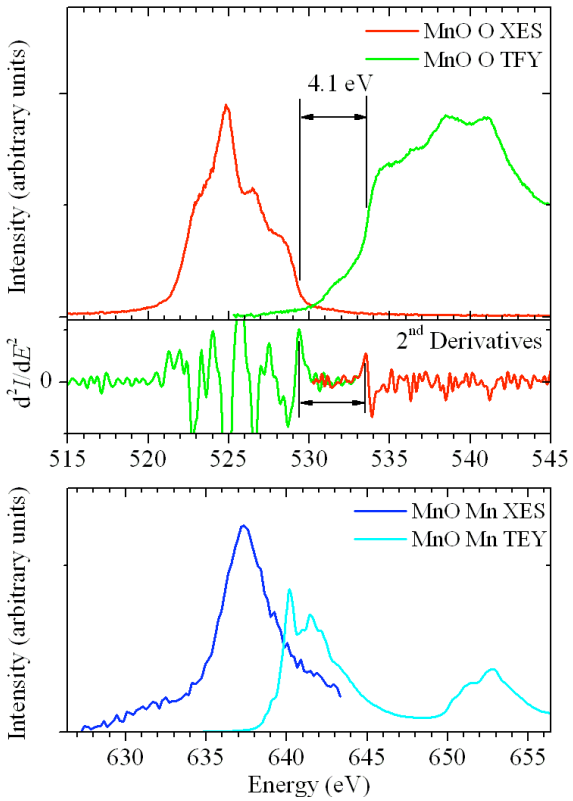

Figure 7.3: XES and NEXAFS measurements at the *K*-edge and $L_{2,3}$-edge of MnO, used to determine the band gap.

The analysis of the spectra of MnO in Figure 7.3 is very much the same as the analysis of the NiO spectra. Once again, the metal edge absorption spectrum, in this case the Mn *2p*

TFY, is shifted to significantly lower energy as a result of the presence of the core hole. The shapes of the O $K\alpha$ XES and O *1s* TFY spectra are quite similar to the corresponding spectra of MnO. The band gap obtained from the examination of the second derivatives of these spectra is 4.1 eV, again in close agreement with the previously reported band gap of 4.0 eV [94].

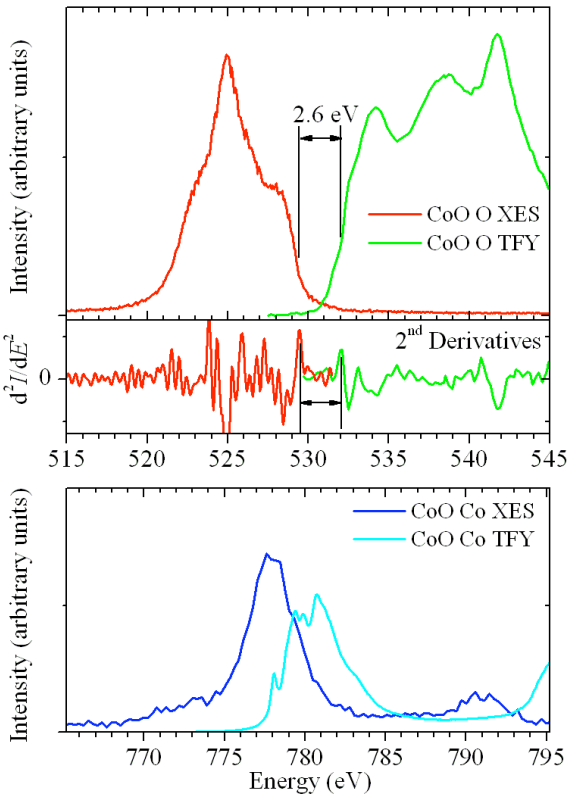

Figure 7.4: XES and NEXAFS measurements at the *K*-edge and $L_{2,3}$-edge of CoO, used to determine the band gap.

The plots of the CoO spectra in Figure 7.4 yield results entirely consistent with what is seen in the analysis of NiO and MnO. The Co *2p* NEXAFS spectrum has again undergone a significant shift due to the presence of the core hole in the final state. The band gap that is obtained from the O *K*-edge spectra is 2.6 eV, in agreement with the published value of 2.5 eV [95].

One of the strengths of this method of band gap estimation is that the reactive samples can often be studied without the need for extensive surface preparation. By utilizing the

fluorescence spectra for both emission and absorption measurements and effective background elimination, a bulk-sensitive study of the electronic structures can be performed.

7.2. HOMO-LUMO Gaps in Organic Materials

In photoactive molecular materials, the wavelength of light that is required to reach the lowest excited state – to move an electron from the HOMO to the LUMO in a one-electron picture – is of particular interest due to the direct relation that it has to the device properties of the material. Note that because of the discrete nature of the molecular energy states, this energy is described by the mean separation between the HOMO and LUMO levels, rather than between the uppermost and lowermost edges of the valence and conduction bands, as is the case in crystalline materials. It is generally a simple matter to locate the lowest-energy transition in the *1s* NEXAFS spectrum of a molecule, due to the usual presence of sharp resonance transitions, but the analysis of molecular XES spectra is not so simple. In this study, a similar method to that which was employed in the study of transition metal oxides is used, and the conclusions are supported by comparisons with simulations of the XES and NEXAFS spectra.

To illustrate the method that is employed, the C *K*-edge XES and NEXAFS spectra of pentacene ($C_{22}H_{14}$, see inset for structure) are displayed in Figure 7.5, along with the spectra that were simulated using StoBe and the second derivatives of the measured spectra. The structure used in the spectral simulations was that determined for a thin film of pentacene [96]. The samples that were measured consisted of a thin layer of pentacene on a Si substrate, with a 10 nm capping layer of Au to prevent oxidation. Because of the presence of the Au layer and contamination on its surface, total fluorescence yield measurements were used to characterize the buried pentacene layer. The comparison with the simulated spectra confirms that this method yields a useful spectrum of the organic layer, without any significant contributions from the surface.

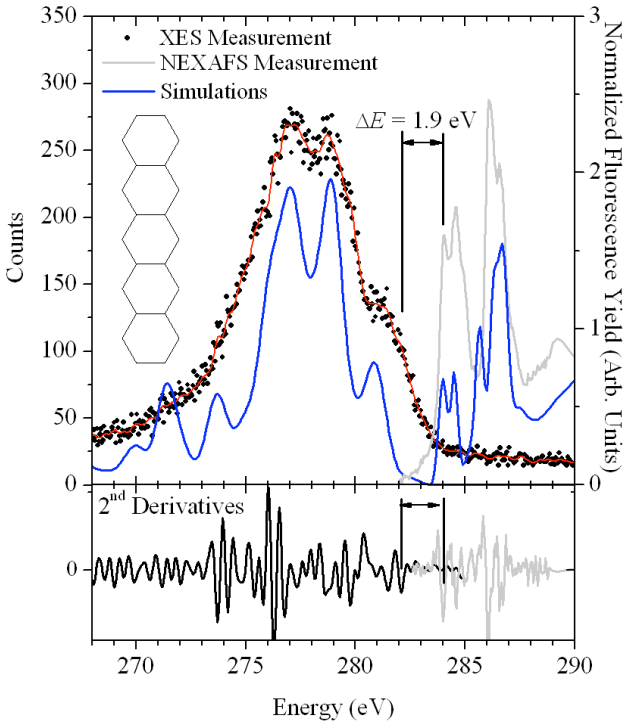

Figure 7.5: Measured and simulated C *Kα* XES and C *1s* NEXAFS spectra of pentacene. The plot of the second derivatives of the measured emission and absorption spectra is used to locate the transitions associated with the HOMO and LUMO, respectively.

Although the location of the lowest-energy π* resonance transition in the measured C *1s* NEXAFS spectrum of pentacene can be easily determined directly from the plot, the second derivative of the spectrum is included in order to illustrate the correspondence between the peak locations and the features in the derivative plot. The minima of the second derivative are located at the centres of the absorption features, even in the case of minor shoulder features such as the one at approximately 285.5 eV, which also appears as a peak in the simulated spectrum. Not explicitly required for the analysis of the NEXAFS spectrum, the second derivative is indispensable for determining the location of the resonance transitions in the XES spectrum. This is particularly useful in the current analysis, as otherwise it would not be at all clear where the highest energy transition occurs, as it shows up as a shoulder on a more distinct resonance. The presence of this

less-intense feature that we attribute to transitions from decay of the highest occupied molecular orbital into the *1s* core state is confirmed by the simulations, which predicts a minor transition in this region.

Having located the highest-energy and lowest-energy transitions in the emission and absorption spectra, respectively, we obtain from their energy difference a HOMO-LUMO gap of approximately 1.9 eV. Considering the limits in resolution and uncertainties introduced by calibration and the core hole effects, this value is in very good agreement with previously reported values, which tend to range from 1.75-1.85 eV [97,98,99].

8. TBPe

A study of a blue-emitting OLED material – 2,5,8,11-tetra-*t*-butyl-perylene (TBPe), the structure of which is shown in Figure 8.1 – was undertaken in collaboration with Dr. T.K. Sham of the University of Western Ontario. The motivation behind the study is to examine any differences that can be seen between molecular (poly)crystalline TBPe and nanoscale structures of the molecule. The study is currently ongoing, but an examination of some of the completed work on the molecular crystalline powder is a useful illustration of some of the techniques that will be employed in later sections, as well as being of scientific interest in and of themselves. The coordinates of the C atoms used in the calculations are contained in APPENDIX F.

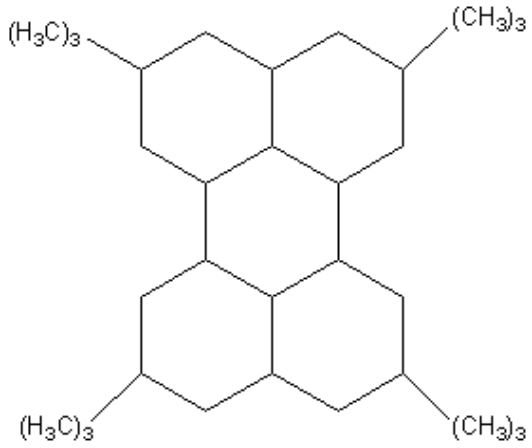

Figure 8.1: Structure of TBPe molecule.

As an aside, the spectra of TBPe make an interesting comparison to pentacene, as the primary structure of both molecules contains five aromatic ring structures, although their arrangement differs markedly. The general shapes of the measured and simulated spectra are similar, but as we will see the specific characteristics of the two molecules' electronic structures are different.

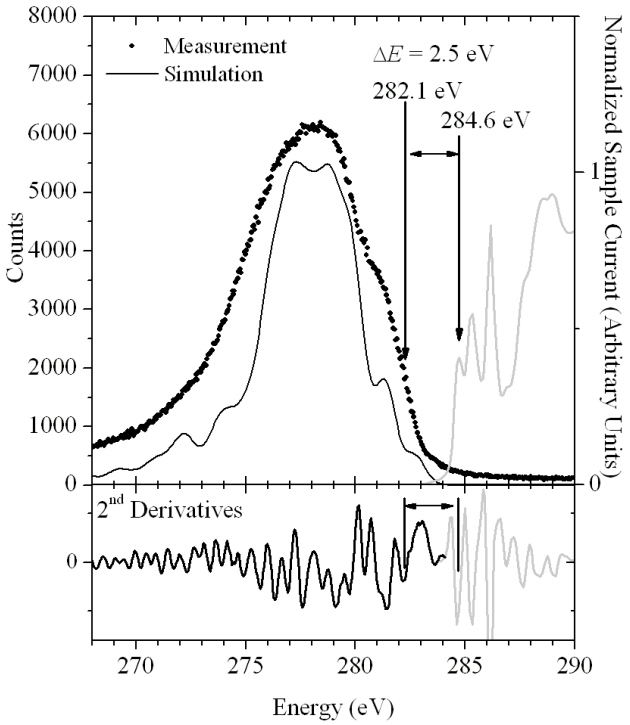

Figure 8.2: Measured and simulated C *Kα* XES and C *1s* NEXAFS spectra of TBPe. The plot of the second derivatives of the measured emission and absorption spectra is used to locate the transitions associated with the HOMO and LUMO, respectively.

The HOMO-LUMO gap estimated from the combination of absorption and emission spectroscopy is 2.5 eV. This is a good approximation of the value of 2.7 eV that is expected from studies of light emitting devices incorporating TBPe [100,101,102]. The reason that this example bears specific attention is that it has also been studied using XEOL, and the main emission peak in the XEOL spectrum in Figure 8.3 [103] is found at approximately the same energy as would be suggested by the HOMO-LUMO gap determined from Figure 8.2. Studies employing a combination of soft X-ray emission, absorption, and optical luminescence are therefore shown to provide a potentially powerful tool for characterizing the optical properties of molecular semiconductor materials.

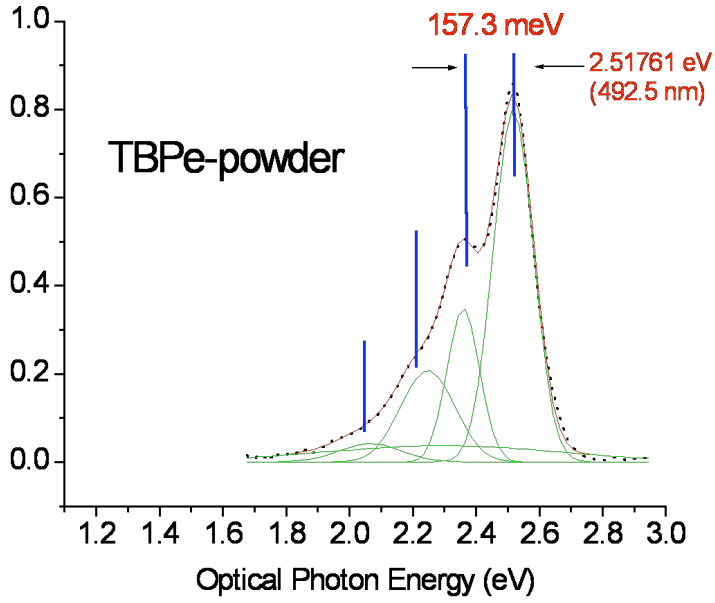

Figure 8.3: X-ray excited optical luminescence spectrum of TBPe powder, measured by the group of Dr. T.K. Sham.

9. Angle-Resolved NEXAFS of Organic Semiconductors

Near-edge X-ray absorption fine structure (NEXAFS) measurements have been used extensively to study the electronic structures of molecular electronics materials. Because it is non-destructive and element-specific, NEXAFS spectroscopy has been used in combination with other characterization techniques such as X-ray diffraction [104], X-ray photoelectron spectroscopy [105,106,107,108,109], and X-ray excited optical luminescence [42]. Angle-resolved NEXAFS measurements have proven to be particularly useful in the characterization of a variety of molecular electronic materials, including phthalocyanine [42,108,109], thiophene [104,110,111,112], and perylene [106,113] derived materials. The information about their structure is of great interest, as it has been shown that the nature of the excitons in molecular semiconductor materials is dependent on the intermolecular interactions [114,115]. The extensive use of this technique to characterize the geometry of molecules on various surfaces has led to carefully refined techniques for measurements and data analysis, as well as a wealth of published spectra that can be used to identify the features observed in the spectra of complex molecules.

The information provided by angle-resolved NEXAFS analysis can be directly related to the observed behaviour of the materials in devices. The charge transport characteristics in molecular semiconductors can exhibit largely anisotropic behaviour [116]. Most of these materials rely on π-conjugation between units or groups within the same molecule for charge transport, and so their efficiency is greatly reliant on the relative orientations of the groups [117] as well as the alignment of the molecules with respect to the applied field [110]. Elucidation of these properties using angle-resolved NEXAFS provides key insight into the structure-function relationships of a particular material, with the goal of tailoring materials and devices to improve efficiency.

9.1. Benzene on Surfaces

Benzene is one of the simplest and most ideal examples of how the dichroism observed in the NEXAFS spectra can be used to elucidate its orientation, and so it is used here as an illustrative example; the dichroic signal observed in the molecular semiconductor 4(HPBT) (Section 10) is directly analogous to what is seen in benzene. As is seen in the simulated spectra in Figure 9.1, the absorption spectrum of a benzene molecule with ideal geometry will demonstrate complete extinction of the lowest-energy π^* resonance feature when the X-ray polarization vector is perpendicular to the molecule's normal plane. Since this property of ordered benzene samples was first reported [118,119] it has formed the basis of a wide variety of studies; the structural distortions of benzene on certain highly-ordered surfaces [120] is based on a comparison with the initial studies. For example, detailed knowledge of the spectral signature of benzene allowed the identities of intermediate products formed during chemical reactions to be determined [121] by monitoring the changes in the benzene spectra over time as the surface was exposed to oxygen. As it is a common ester used as an endgroup for molecules, the ability to determine the orientation of a benzene ester attached to a larger molecule adsorbed on a surface provides a means to infer the orientation of the larger molecule, which may not have a dichroic signal associated with it [122]. It will be shown in Section 10 that its dichroic signal can also be used in conjunction with another component of the same molecule to provide some indication of how planar the structure is.

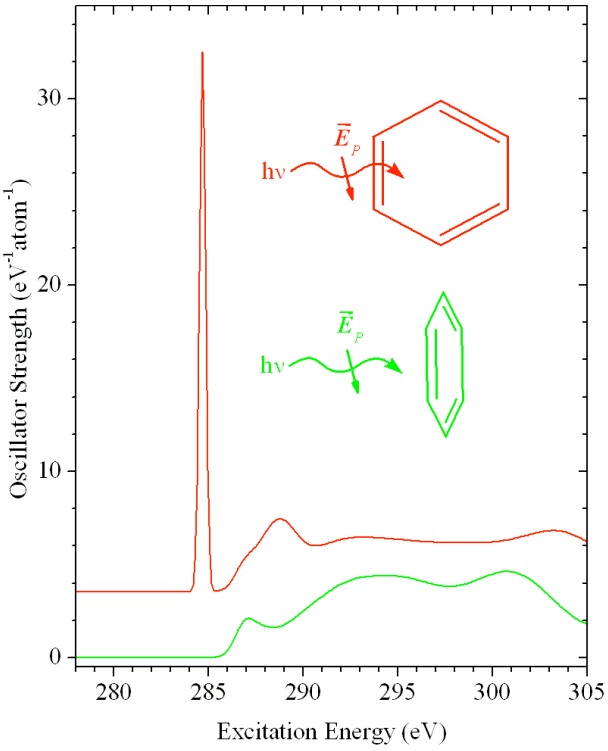

Figure 9.1: Simulation of the C *1s* NEXAFS spectra of benzene excited by linearly polarized light at grazing and normal incidence. The polarization of the (modelled) incoming radiation is into the page. A vertical offset is added for clarity.

9.2. Thiophene on Surfaces

The examination of the geometry of thiophene on a surface was one of the examples of the usefulness of angle-resolved NEXAFS to study a specific surface-science problem, namely the thermally-induced desulfurization of thiophene on a Pt surface [107]. Temperature- and angle-dependent NEXAFS were used to study the cleaving of the C-S bond and the formation of a metallocycle in which the S atom was replaced with a Pt that had been removed from the surface, leaving an isolated S atom adsorbed onto the surface. Thiophene's aromatic structure makes it ideal for angle-resolved studies, as it demonstrates strong dichroic shifts in the resonances associated with the C-C and C-S bonds, as is seen in Figure 9.2.

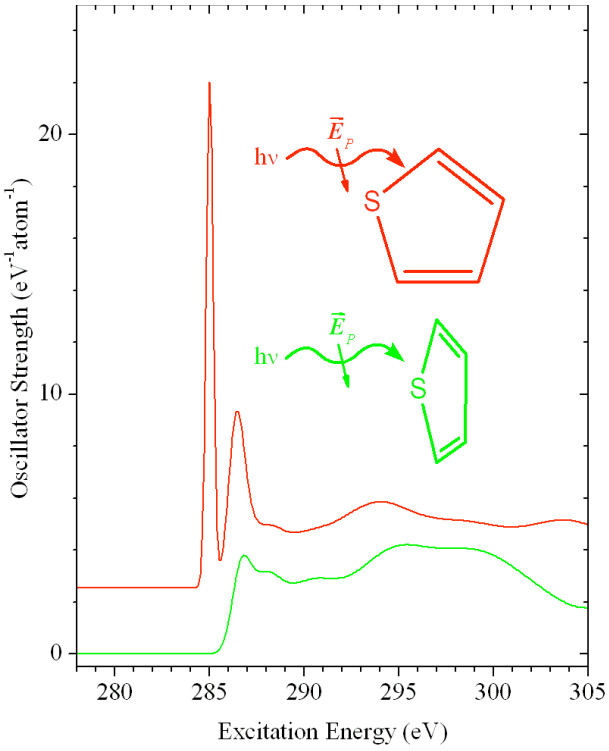

Figure 9.2: Simulation of the C *1s* NEXAFS spectra of thiophene excited by linearly polarized light at grazing and normal incidence. The polarization of the (modelled) incoming radiation is into the page. A vertical offset is added for clarity.

9.3. Molecular Orientation of Molecular Semiconductors

The various connections between the function, molecular orientation, and electronic structure of molecular semiconductor materials means that their NEXAFS spectra can be used to obtain information that is directly relevant to the process of tailoring their structures. As an example of the application of these techniques to molecular optical materials, it is worthwhile to describe the work that has been done to characterise pthalocyanine (Pc), which is a good analogue to the 4(HPBT) study that will be presented in detail in Section 10. Pthalocyanine has a planar structure composed of several aromatic groups. In its most basic form, two of the inner N sites are protonated; deprotonation of these sites produces a ligand with -2 charge, allowing a variety of metal ions to be incorporated in the centre. Anisotropic charge transfer characteristics have been observed in this molecule, which provides the motivation for studies of the orientation of the

molecules on surfaces. The simulated angle-dependent N *1s* NEXAFS spectra of CuPc is plotted in Figure 9.3; it shows the strong dichroic behaviour of the π* features below 405 eV. The survival of the lowest energy peak in the bottom spectrum is likely due to hybridization with the unoccupied *3s* states of the Cu^{2+} ion, which would not exhibit a strong preferential orientation.

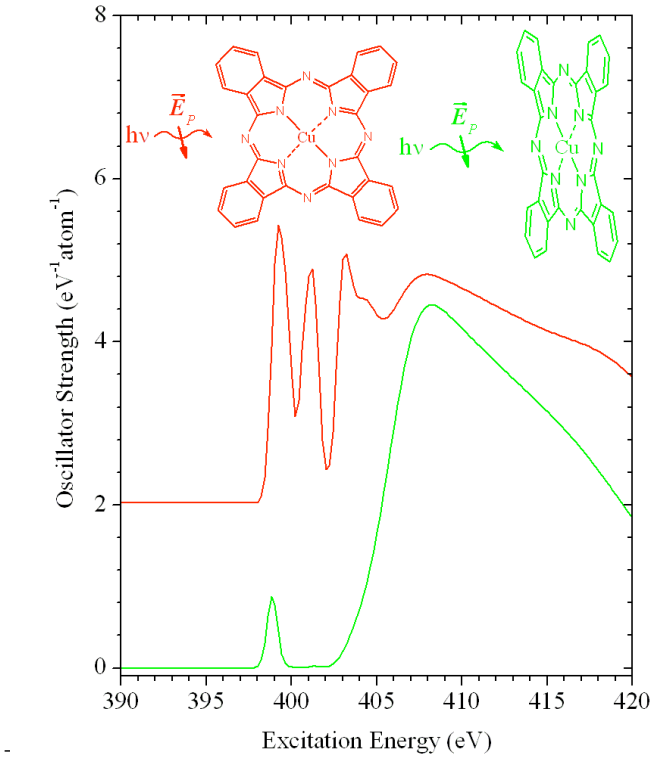

Figure 9.3: Simulation of the N *1s* NEXAFS spectra of pthalocyanine excited by linearly polarized light at grazing and normal incidence. The polarization of the (modelled) incoming radiation is into the page. A vertical offset is added for clarity.

The simulated spectra in Figure 9.3 agree well with measured spectra [124,125], and were calculated as part of a collaboration with Dr. C. McGuinness, Trinity College, Dublin [123]. The film-forming behaviour of Pc provides an indication of the factors that must be accounted for in the study of 4(HPBT). It has been observed that the orientation of the Pc molecules depends strongly on the thickness of the films and on the nature of the substrate [109,124,125,126,127,128,129]. Of particular interest is the contrast between the alignment of Pc on well-defined crystal plane surfaces and its alignment on

polycrystalline or rough surfaces. When deposited on an ordered surface, the substrate-molecule interaction is high and the bottommost layers of the molecule are flat-lying. On other substrates, including layers of other organic molecules, the molecule-molecule reaction dominates and the Pc aligns itself in an ordered, upright position.

9.3.1. Oligothiophenes

Molecular semiconductors based on oligothiophene structures show a great deal of promise for future applications, particularly in electron transporting materials. The conjugated thiophene backbones show a strong general tendency to order, leading to high electron mobilities. A specific challenge of dealing with oligothiophene devices is to overcome their naturally low solubility. This is achieved by the attachment of specific esters to enhance solubility without having a direct effect on the electronic properties of the molecule. In order to further minimize any possible effects on device operation, several oligothiophene molecules have been developed that employ solubilizing groups that can be removed by thermolysis [130,110]; this annealing of samples leads to increased molecular and crystalline ordering. Enhanced solubility can also be achieved by forming dendritic or star shaped oligothiophene materials in which three [131,132] or four [133,134,135,136] identical arms are attached to a central conjugated core, with solubilizing esters at the end of each arm.

10. 4(HPBT)

A series of soluble, star-shaped molecules based on the coupling of dithiophene groups to a central benzene has been recently fabricated [133,136] and have shown to exhibit good device properties in OLED [133], photovoltaic [135], and photocontrolled transistor [134] devices. The solubility of the molecules overcomes one of the limitations of oligothophene-based materials, which have been extensively utilized in molecular electronic applications due to their high level of π-conjugation. We have used a combination of characterization techniques to demonstrate that the molecules have good film-forming properties, resulting in highly-ordered films with the molecules sitting in a largely upright conformation.

In the current study, we use a combination of angle-resolved C *1s* NEXAFS and XEOL to determine the film-forming capabilities of 4(HPBT). The measured NEXAFS spectra are modeled using density functional theory in order to assign the observed spectral features to particular functional groups and also to provide a theoretical model of the electronic interactions within 4(HPBT).

10.1. Measurements

C *1s* NEXAFS measurements were performed at the SGM beamline at the CLS. The monochromator exit slit was set to 20 μm, giving an experimental resolution better than 10 meV. Samples were mounted on a freshly-scraped surface of indium foil. Films were formed by depositing small amounts of the materials in a chloroform solution on the indium surface with a pipette and allowing them to dry.

10.2. Calculations

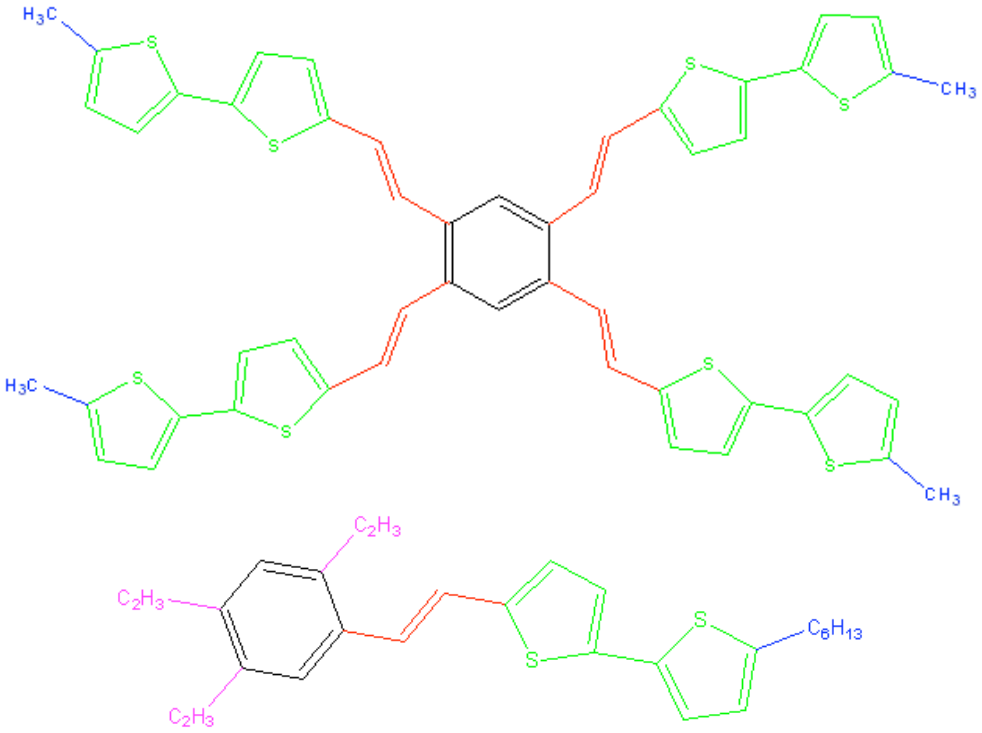

Figure 10.1: Schematics of structures used to model spectra of 4(HPBT).

Due to software limitations and difficulties in achieving convergence, it was necessary that two models be combined to produce the model of the C *1s* NEXAFS spectrum of 4(HPBT). The schematics in Figure 10.1 show the structures of the two models; the colour of each chemical group within the structure corresponds to the colour of the line used to plot the simulation of its C *1s* NEXAFS spectrum in Figure 10.2. The coordinates of the heavy atoms in each model are given in APPENDIX G. The larger model was very similar to the actual structure, the only difference being that the hexyl chain at the periphery of each branch was replaced by a methyl group. The geometry optimization was performed subject to the constraint that the molecule exhibit C_2 point group symmetry. A smaller model consisting of the central benzene ring and a single branch, including the hexyl chain group, and methyl groups replacing the other three branches, was optimized without constraints. The simulated spectra of the hexyl chain group and the substituent site of the distal thiophene group were included in the overall spectral simulation, in place of the methyl group and substituent site of the larger model. The

calculated oscillator strengths were broadened with Gaussian functions with line widths of 0.4 eV (FWHM) up to the ionization potential and then linearly increasing to 4.5 eV (FWHM) over the next 10 eV.

10.3. C *1s* NEXAFS Measurement and Simulation

The NEXAFS spectrum of 4(HPBT) – the topmost spectrum in Figure 10.2 – features the sharp resonance peaks that are generally associated with the presence of aromatic carbon structures; in order to properly interpret the measured spectra it will be necessary to assign the individual spectral features to specific groups within the molecule. To this end, StoBe DFT was used to simulate the C *1s* NEXAFS spectra of each C site individually. The π* features *A* and *B* have contributions from both the thiophene and benzene groups. Peak *A* (284.7 eV) is primarily associated with the central benzene ring and the adjacent vinyl C sites. It is possible that this peak contains a contribution from pendant alkene groups formed through deprotonation of the hexyl chain groups [110], but the analysis of the angle-resolved NEXAFS spectra, below, suggest that this is not the case. The shape of the simulated spectra of the thiophene groups is in good agreement with previously published results [107], including the prominent feature associated with the C-S σ* orbitals (peak *C*).

The role of the attached hexyl chain groups is to increase the solubility of the molecule [133], and they do not play a significant role in the electronic behaviour of the molecule. The lack of any resonant absorption features below 287 eV in their calculated absorption spectrum indicates that the hexyl chains do not have any direct effect on the lowest unoccupied molecular orbitals that are involved in the electron transporting properties of 4(HPBT).

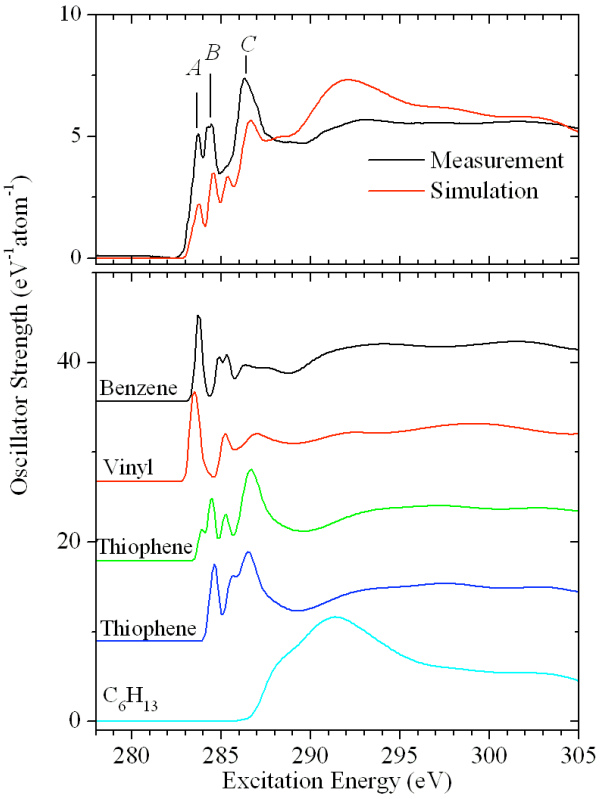

Figure 10.2: Comparison of measured C *1s* NEXAFS spectrum of 4(HPBT) powder with simulated spectra. The group-resolved NEXAFS calculations allow the features in the measured spectrum to be assigned unambiguously.

10.4. Angle-Resolved C *1s* NEXAFS

The angle-resolved C *1s* NEXAFS spectra of the 4(HPBT) samples are displayed in Figure 10.3; there is a clear dependence of the intensity of the sharp π* features on the angle of incidence θ, measured with respect to the sample normal, indicating that the 4(HPBT) becomes ordered when cast on the indium foil. The plot of the peak heights of features *A* and as a function of $\sin^2\theta$ show that the dichroic signal increases linearly; extrapolation of the curves suggests that the intensities of both peaks will be very near zero at perfectly grazing incidence, indicating that the molecules are almost perfectly upright in the film, with very little disorder. The results suggest a high-degree of intramolecular π-conjugation between the aromatic structures, facilitating electron transport through the molecule [117]. It should be noted that due to the surface-sensitivity

of the TEY measurements, we cannot rule out the presence of a flat-lying 4(HPBT) layer at the interface with the substrate or other buried disordered structures. The angular dependence of peak *C* is less pronounced and does not tend toward zero, but this is largely due to its association with the in-plane σ* orbitals of the C-S bonds.

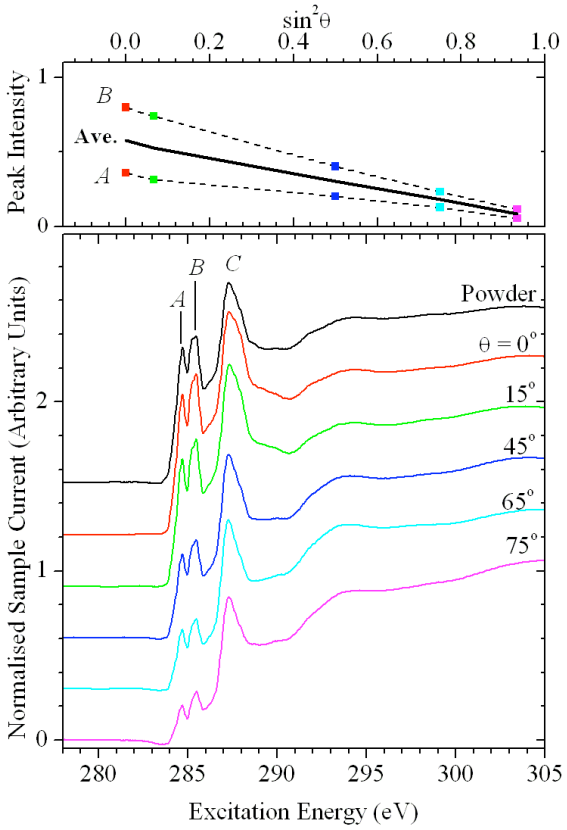

Figure 10.3: C *1s* NEXAFS spectra of 4(HPBT) powder and drop-cast films, measured at various angles of incidence. The quoted angle describes the angle between the sample normal and the X-ray polarization vector. A uniform background signal has been removed, and the spectra were normalized to unity at 325 eV. A vertical offset is added for clarity. The top panel shows the dichroic changes in the peak heights as a function of $\sin^2\theta$.

10.5. X-ray Excited Optical Luminescence

Measurement of the X-ray excited optical luminescence spectra of 4(HPBT) led to a further understanding of its electronic structure and the way that it absorbs energy from

photons. There was a distinct dependence of the luminescence spectrum on the excitation energy; the major distinction was between resonant and non-resonant excitation. This is clearly seen in Figure 10.4, in which the luminescence spectra obtained when exciting at 286.2 eV, 288.2 eV, and 303.1 eV show three distinct, non-dispersive emission peaks that are not present in the other spectra.

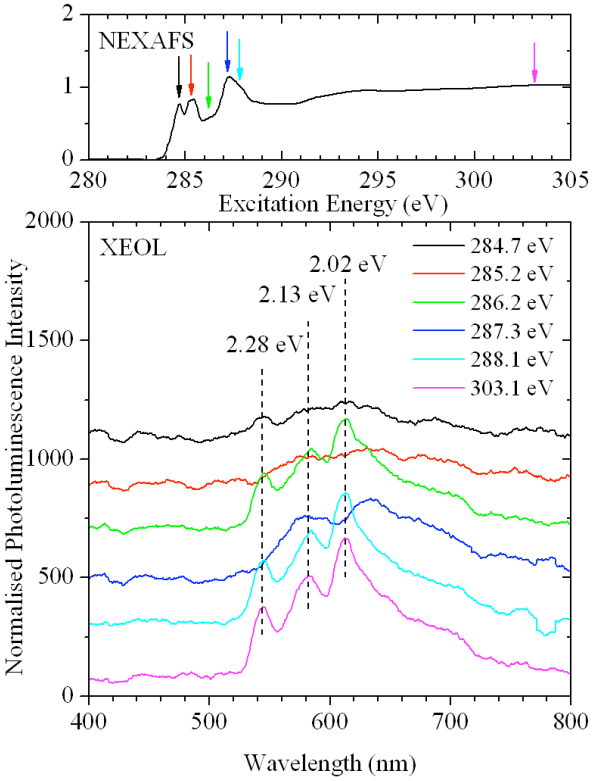

Figure 10.4: C *1s* NEXAFS (top panel) of 4(HPBT), with arrows indicating the energies used to excite the XEOL spectra (bottom panel).

The highest energy peaks in the photoluminescence spectra occur at 2.28 eV; this value is very close to the reported HOMO-LUMO gaps for 4(HPBT) films (2.20 eV) and in a chloroform solution (2.40 eV). We therefore assign this peak, with a fair degree of confidence, to photons emitted when the first excited state returns to the ground state. The two other peaks (2.13 eV and 2.02 eV) represent the (0-1) and (0-2) modes of a vibrational series. The (0-0) mode resonance in the XEOL is located very near the energy

of the lowest energy vibronic transition in the photoabsorption spectrum of the annealed film sample (2.40 eV) [133,136].

The appearance of the sharp photoluminescence features only off-resonant excitation is counterintuitive, as a strict one-electron view of resonant excitation would suggest that they directly populate the lowest unoccupied orbitals, and so one would predict that the luminescence arising from the decay of this excited state would be enhanced. This is far too simplistic a view of the processes involved, however. The core-excited state with a populated LUMO cannot decay via a direct transfer of the excited electron into the HOMO level for the simple reason that the HOMO state will be fully occupied. The detection of such a transition is not impossible, because a vacancy in the HOMO level can be present either as a result of natural thermal depopulation or as a result of multistage processes in which the core hole is refilled by less tightly-bound electrons. These processes are minor, however, and account for the very small 2.28 eV and 2.02 eV peaks that are observed when exciting at 284.7 eV.

The mechanism that leads to the creation of the first excited state – the decay of which leads to the peak at 2.28 eV – is the same mechanism that is behind RIXS processes. Exciting off-resonance does not lead to the direct creation of a core-excited state; the absence of resonant transitions requires that scattering processes must dominate [26]. As a result, the HOMO-LUMO transition is induced through an energy-loss process, and the excited state preferentially decays through photoluminescence. The peak in the XEOL spectrum can therefore be seen as complementary to an energy-loss feature in a RIXS spectrum.

10.6. C $K\alpha$ XES and RIXS of 4(HPBT)

The C $K\alpha$ XES spectrum of 4(HPBT) does not have nearly the same richness of features as does the NEXAFS spectrum. Nevertheless, it is worthwhile to examine the measured XES and RIXS spectra of 4(HPBT) as a potential source of valuable information about the electronic structure, especially considering that a considerable portion of the analysis has focused on the relative energy positions of the occupied and unoccupied states.

The non-resonantly excited C $K\alpha$ XES spectrum of 4(HPBT) is shown in Figure 10.5, along with the spectrum simulated using StoBe. The transitions predicted by the electronic structure calculations were broadened with uniform 1 eV Gaussian functions. Because of the lack of clear features in the measured spectrum, any conclusions drawn from its comparison with the simulated spectrum must be made with caution. At best, it can be said that the results of the measurement and simulation are not contradictory, with the shape of the measured spectrum being generally reproduced, including the relative locations of the most prominent shoulders relative to the main white line peak. Certainly, a more creative application of broadening schemes could result in better agreement between the two curves, but this was not undertaken as it would provide no useful information.

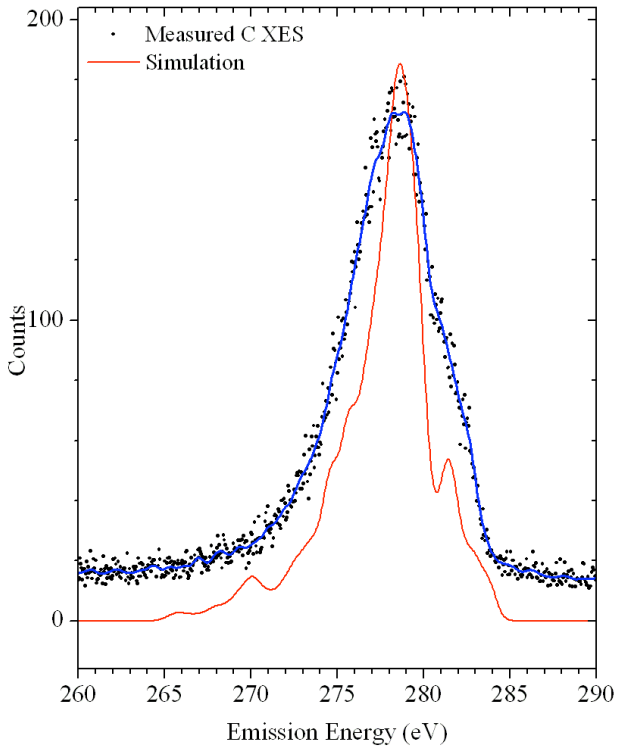

Figure 10.5: Comparison of measured C *Ka* XES spectrum of 4(HPBT) to the simulated spectrum.

The results of the XEOL measurements shown in Figure 10.4 suggested that the C *Kα* RIXS spectra might show energy loss features when exciting off resonance. Several excitation energies were chosen in the vicinity of the low-energy π* absorption features, as well as one energy slightly above the C-S bond resonance; the results of the experiment are plotted in Figure 10.6. The absorption spectrum that was measured at beamline 8.0.1 was distorted due to carbon contamination of the Au mesh and other beamline components. By comparing this spectrum with other C *1s* NEXAFS spectra measured at the beamline, it was ascertained that the feature at 288.7 eV was an artifact of produced in the normalization procedure. The contamination will not have any effect on the emission spectra, however, because they are not normalized to the incoming photon flux.

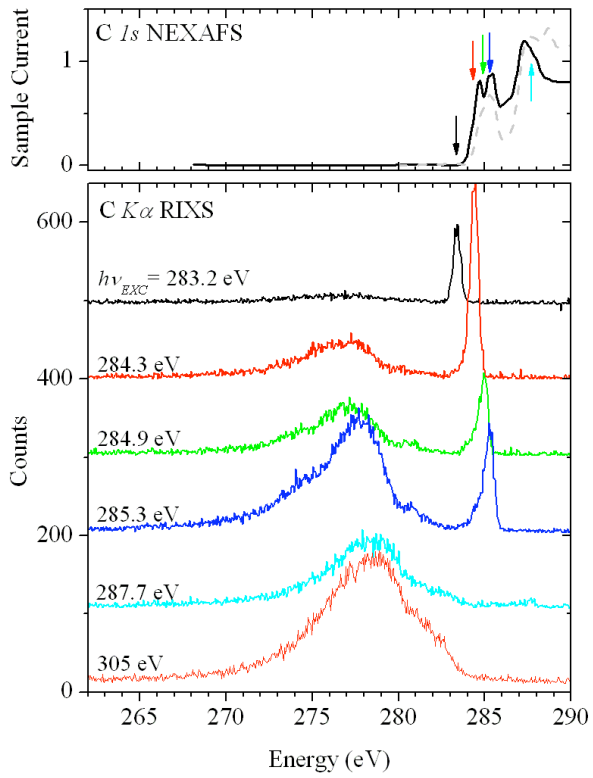

Figure 10.6: C *Ka* RIXS spectra of 4(HPBT). The dotted spectrum in the top panel is the C *1s* NEXAFS spectrum recorded at BL8, showing significant distortion due to carbon contamination of the Au mesh used to monitor the photon flux.

No clear energy-loss features can be observed in the RIXS spectra shown in Figure 10.6, although some changes in the spectral lineshape are observed. The changes are presumably related to selective excitation of particular chemical groups. Although it did not provide much insight into the electronic structure of 4(HPBT), the RIXS study provided a means for accurately calibrating the XES data using the positions of the elastic peaks as a guide.

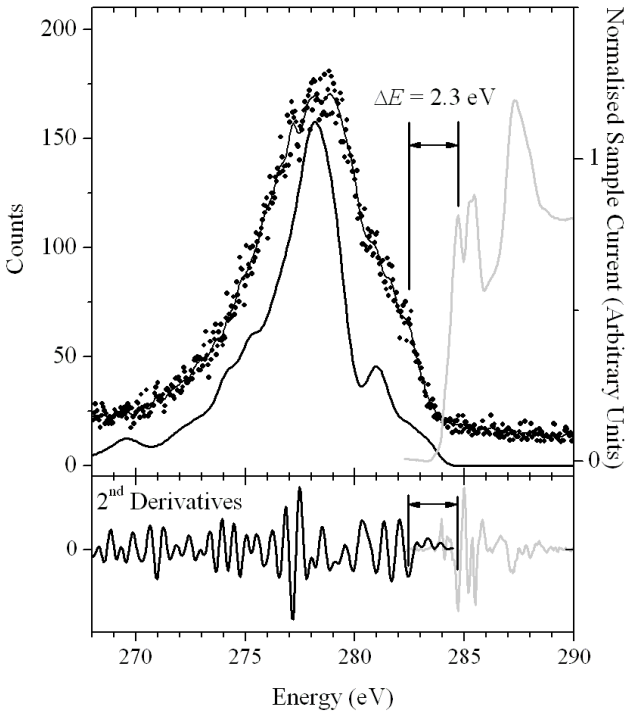

Figure 10.7: Comparison of 4(HPBT) non-resonantly excited XES spectrum with simulated spectrum. 2nd derivatives of measured XES and NEXAFS spectra are used to determine HOMO and LUMO levels.

The energy difference between the lowest-energy peak in the NEXAFS spectrum, at 284.6 eV, and the highest energy peak – approximately 282.4 eV, as best as it can be determined – in the XES spectrum is approximately 2.3 eV, in agreement with the previously determined values. However, the large possible error in the determination of the HOMO location (at least ±0.2 eV) means that the results obtained in this method are

open to analytical bias, and so this is not a particularly effective method for determining HOMO-LUMO gaps, at least without significant refinement to the method. Given the uncertainties involved, the conclusion will be limited to the statement that the HOMO-LUMO gap estimated from the comparison of the C *K*-edge XES and NEXAFS spectrum is not in disagreement with the value obtained by other methods.

10.7. Radiation Damage in 4(HPBT)

Preliminary measurements of the C *1s* NEXAFS spectrum of 4(HPBT) powder were carried out at the SGM beamline in order to evaluate the viability of the project, in particular as it pertained to possible radiation damage. Consecutive spectra were measured in the same manner that the radiation damage in glycine was studied; the spectra of 4(HPBT) are shown in Figure 10.8. Compared to the drastic changes observed in glycine, the effects of irradiation of 4(HPBT) are relatively minor. Peak *A* decreases in intensity, becoming a low-energy shoulder on peak *B*. The intensity of peak *C* decreases as a function of irradiation, representing a decrease in the number of C-S bonds. It is likely that this represents removal of thiophene groups from the sample rather than desulfurization [107] or other chemical changes, because these processes would likely result in the formation of new chemical species with their own distinct spectral fingerprints.

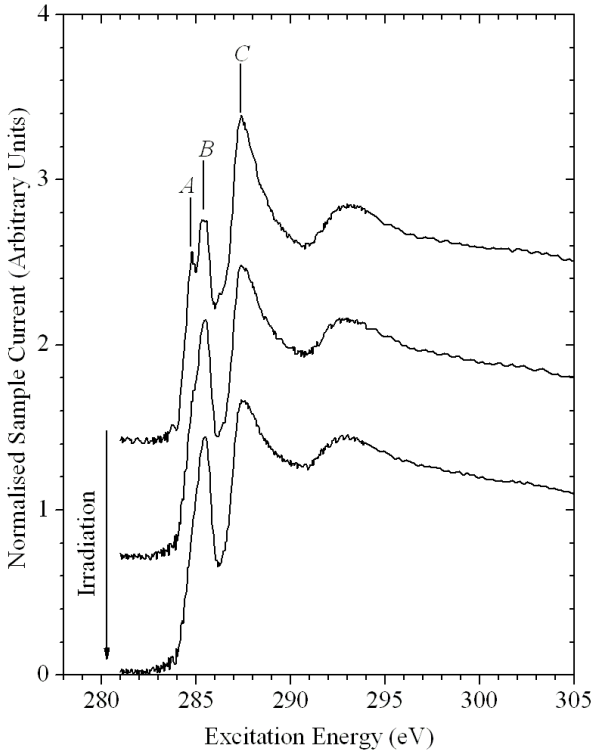

Figure 10.8: C *1s* NEXAFS spectra of 4(HPBT) powder showing the effects of radiation damage.

10.8. Conclusions

The films formed by 4(HPBT) on the amorphous indium substrates demonstrate a strong dichroic signal indicative of a highly ordered structure; the plot of the dependence of the intensity of the sharp π* features on the angle of incidence indicates that the molecules stand virtually upright on the surface. The C *K*-edge absorption and emission spectra were modelled well by the StoBe DFT simulations, allowing the origin of the measured spectral features to be determined. Measurements of the XEOL spectra excited at various resonant and non-resonant energies showed unexpected behaviour, in which a sharp vibronic series emerged when exciting off-resonance, but was quenched during resonant excitation. The highest-energy (0-0) transition in the XEOL spectra was observed at 2.28 eV, in good agreement with previous estimates of the HOMO-LUMO gap. Further confirmation of the relationship between this luminescent transition and the HOMO-

LUMO gap was provided by comparing the energy of the highest-energy feature in the C *K*α XES to the energy of the lowest-energy feature in the C *1s* NEXAFS. Supported by the spectral simulations, this energy difference was found to be 2.3 eV, closely agreeing with the other methods for estimating the HOMO-LUMO gap.

11. PCBM and 4(HPBT):PCBM Blends

The examination of the samples made by blending solutions of 4(HPBT) with PCBM (Figure 11.1) has revealed important information about the structure of the films. The motivation for the study is to characterize the structure of the film; particularly to determine if there is evidence for the formation of a bulk heterojunction region in which significant intermixing of the materials is found. This arrangement has been found to be optimal for the fabrication of molecular semiconductor devices, as it maximizes the interaction surface between the two materials. In this study, the comparison of surface-sensitive TEY and bulk-sensitive TFY clearly shows that a bilayer structure is produced in the drop-cast films, with the PCBM underneath the 4(HPBT), but the emergence of higher-energy π*-like features in some spectra suggests that there may be relatively strong chemical interaction between the two materials, especially after annealing. Aside from the clear evidence of a predominantly bilayer structure, some of the conclusions that are drawn are of a speculative nature, but they nevertheless suggest intriguing avenues for further study.

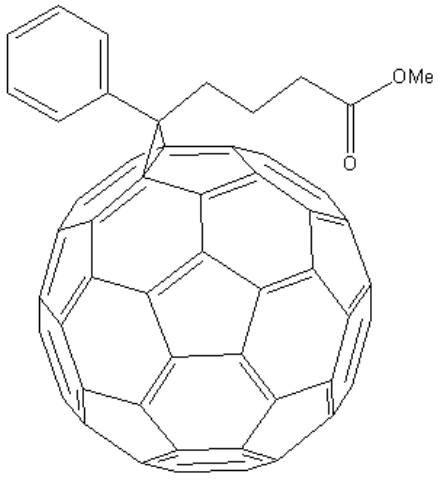

Figure 11.1: Structure of hole-transporting molecule PCBM.

11.1. C *1s* NEXAFS Spectra of PCBM

The C *1s* NEXAFS spectra of PCBM, shown in Figure 11.2 are, as expected, very similar to that of the C_{60} reference sample; very few differences between the reference sample

and the powdered PCBM are apparent. The effects of the potassium contamination of the Au mesh can be seen in these spectra. The sharp peaks associated with the K $L_{2,3}$ absorption (seen in APPENDIX D) cause an overestimation of the photon flux, and so the normalisation procedure causes corresponding sharp dips in the spectrum. The location of these dips is such that the analysis of the spectra is not affected. The shoulder on the high-energy side of the 284.4 eV peak in the PCBM is primarily associated with the benzene ring on the substituent [137]. Unfortunately, the reference sample and the PCBM samples were measured at different beamlines at different times, and so it is possible that some of the differences may arise from differences in the equipment. For example, the peaks seen at 288.6 eV and 291.1 eV in the reference spectrum are both found at slightly lower energy in the PCBM measurements (288.4 eV and 290.9 eV). Although this may in fact reflect a difference in their electronic structures caused by the structural difference, it seems equally likely, if not more so, that the difference arises from differences in the monochromator energy calibration. For all subsequent measurements of PCBM, measurements of reference samples of C_{60}, phenol, and a butyric acid compound (or related compounds) should form part of the experimental protocol.

The shapes of the spectra measured from the drop-cast films of PCBM differ significantly from that of the powder sample. The main π^* resonance is suppressed, and the shoulder appears as a distinct peak. An additional feature emerges at 287.4 eV; this peak is consistent with a characteristic feature of the σ^* absorption of benzene [137]. It is also possible that the differences are a result of surface oxidation or contamination. It may also reflect a modification of the carbonyl groups of the butyric acid and methyl ester groups that are part of PCBM.

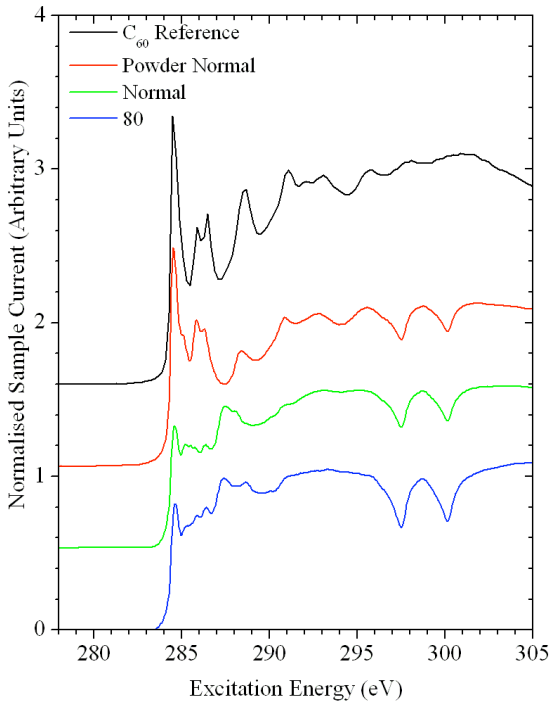

Figure 11.2: C *1s* NEXAFS spectra of C_{60} reference sample, PCBM powder, and drop-cast PCBM films. Spectra were measured in surface-sensitive total electron yield mode. A vertical offset is added for clarity.

The bulk-sensitive TFY measurements shown in Figure 11.3 differ somewhat from the electron yield measurements in Figure 11.2. The differences between the two measurements of the powder samples can be largely attributed to a decrease in contrast caused by fluorescence self-absorption, which is to be expected in a material composed primarily of the element being probed. The peak positions in the TFY spectrum of the powder do not differ from those in the TEY spectrum, nor do any new peaks appear. As a result, we conclude that there is no evidence of differing chemical compositions between the surface and the bulk of the powder sample.

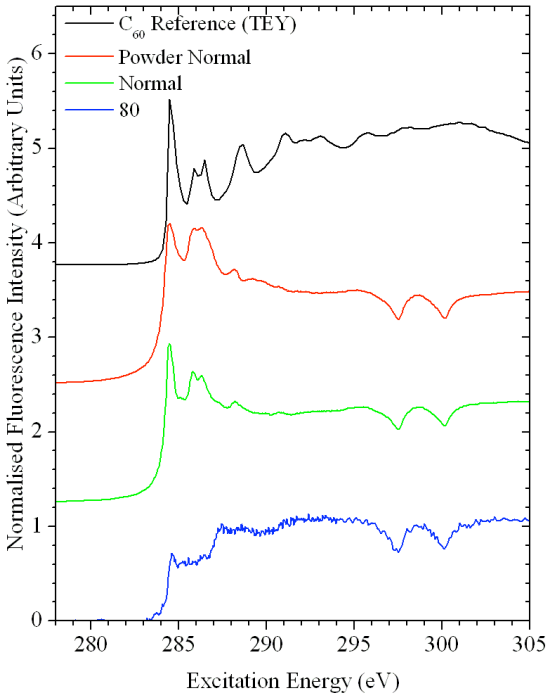

Figure 11.3: C *1s* NEXAFS spectra of C_{60} reference sample, PCBM powder, and drop-cast PCBM films. Spectra were measured in bulk-sensitive total fluorescence yield mode (except for C_{60}, as indicated). A vertical offset is added for clarity.

At normal and near-normal (not shown in Figure 11.3) angles of incidence, the TFY spectra of the film resemble that of the powder; no new features or significant angle-dependence is observed. However, at grazing angles of incidence the shape of the spectra is dramatically altered, and the TFY measurements (a spectrum was also measured at 60°) begin to closely resemble the TEY spectra. Because self absorption effects decrease upon going to grazing incidence due to the decreased normal penetration depth, this effect must be related to a difference in the composition of the sample surface, as the grazing incidence measurements will be surface-sensitive due to the geometry of the experiment.

11.2. C *1s* NEXAFS of 4(HPBT):PCBM Films

Having now examined the spectra of the PCBM and 4(HPBT) films, these observations can be used to study the structures of the drop-cast films of mixtures of the two materials.

The samples were prepared by mixing small volumes of solutions of the two molecules at room temperature, and depositing small amounts of material onto freshly-scraped indium foil. The concentrations of the individual solutions were unknown, and so no accurate estimate of the empirical formula can be made. In future studies, particular care should be taken to control the relative concentrations of the individual components. In this preliminary study, the different films are labelled according to the approximate volume ratios of the solutions used in the preparation, they are designated in the format *V*[4(HPBT)]:*V*[PCBM].

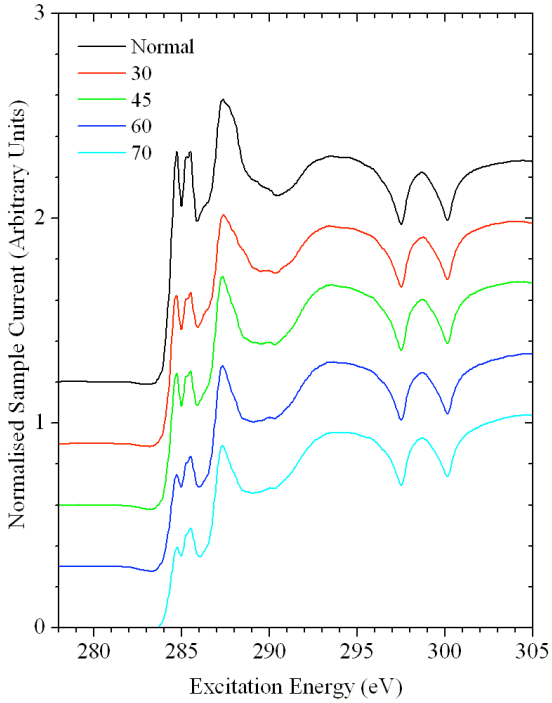

Figure 11.4: C *1s* NEXAFS TEY spectra of 1:1 (liquid volume fractions) of drop-cast 4(HPBT)/PCBM films measured at various angles of incidence with respect to the sample normal. A vertical offset is added for clarity.

In Figure 11.4, the TEY spectra of the 1:1 films as a function of the angle of incidence of the X-rays are displayed. The spectra very closely resemble the spectra of pure 4(HPBT) shown in Figure 10.3; in fact they are, for all analytical purposes, identical. The angle dependence of the spectral features is suppressed compared to that which was observed in

the measurements of the pure 4(HPBT) films, suggesting decreased ordering of the 4(HPBT) in the blend samples.

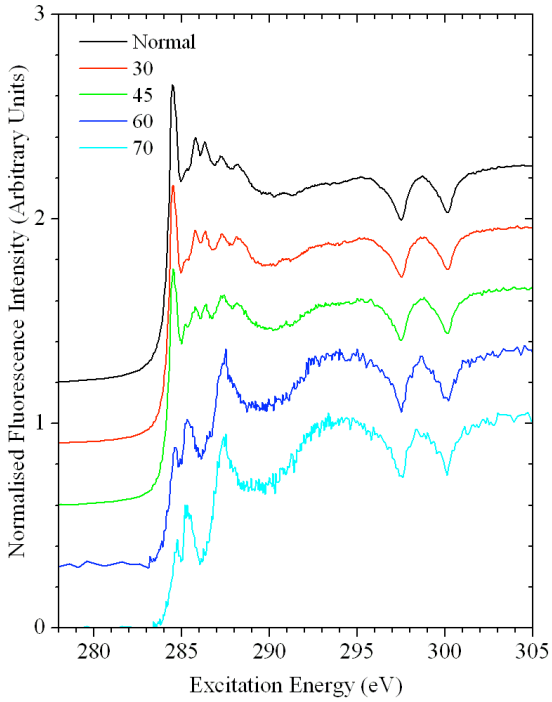

Figure 11.5: C *1s* NEXAFS TFY spectra of 1:1 (liquid volume fractions) of drop-cast 4(HPBT)/PCBM films. A vertical offset is added for clarity.

Significant differences become apparent when the TEY spectra are compared to the simultaneously-recorded TFY spectra. The spectra can be interpreted as a superposition of those of the individual components, with the relative contributions of each being dependent on the angle of incidence. At more normal incidences, the spectra are dominated by the PCBM-like contributions; in conjunction with the observations from the TEY spectra, this finding suggests that the films of the blend samples have a bilayer structure in which the PCBM is adjacent to the substrate surface. The grazing incidence TFY measurements support this model, as they are, as above, surface sensitive, and they resemble the spectra of pure 4(HPBT). It should be noted that this arrangement of the bilayers would in fact be the preferred arrangement for constructing a device based on

blends of the two materials – films are cast on an anode substrate, and it is therefore important to have the hole-transporting material in contact with the surface.

There is little in the blend spectra that can be used to probe the nature of the interaction between the two materials. The majority of the spectral features are identical to what would be expected from a superposition of the individual component spectra. The only exception is the peak at 288.3 eV, which is overrepresented in the spectra of the blend samples, particularly at more normal angles of incidence. The origin of this feature cannot be determined unambiguously; the energy suggests that it is related to a carbonyl C=O bond, but no further information about its origin can be gleaned from the spectra. One possibility is that the surface coverage of films of the blend samples is significantly worse than that of either component material and that the peak is associated with contamination of the indium substrate; further characterization of the surface must be undertaken to determine whether this is in fact the case.

11.2.1. Effects of Variation of Composition

In order to gain a better understanding of the structure that is formed when the 4(HPBT) and PCBM solutions are used to deposit films, solutions of various relative concentrations of the two materials were prepared and deposited as films. Changing the relative concentrations of the two materials in the solution used to deposit the films has direct effects on the measured spectra. Based on the findings of the previous section, it would be expected that because the films form a bilayer structure, reducing the relative concentration of the 4(HPBT) should not significantly affect the nature of the PCBM layer or the interface between the two; the major effect would be to reduce the thickness of the 4(HPBT) layer on the surface. If the thickness of this layer can be reduced sufficiently, a monolayer of 4(HPBT) will in theory be produced, and the nature of the interface can be studied directly.

The spectra displayed in Figure 11.6 were measured from films having a concentration of 4(HPBT) roughly half as high as above. There is a clear effect of the change in composition on the NEXAFS. Most striking is the emergence of the 288.3 eV feature that was seen in the TFY spectra of the 1:1 film (Figure 11.5). Proceeding under the

assumption that the change in 4(HPBT) concentration has led to a corresponding decrease in the thickness of the 4(HPBT) surface layer, we can speculate that this peak may be characteristic of the interface between the two materials. Supporting this assertion is the fact that the feature is proportionally much more intense than was seen in Figure 11.5, suggesting that its emergence is not simply associated with an increased signature of PCBM over the TEY spectra measured previously (Figure 11.4). Also, the composition of the film that was measured for Figure 11.6 is closer to pure PCBM than was the 1:1 film, and it is therefore illogical that the surface coverage for this film would be worse than for the 1:1 film, as it would tend to converge toward the good film-forming properties of PCBM as the concentration of 4(HPBT) is decreased.

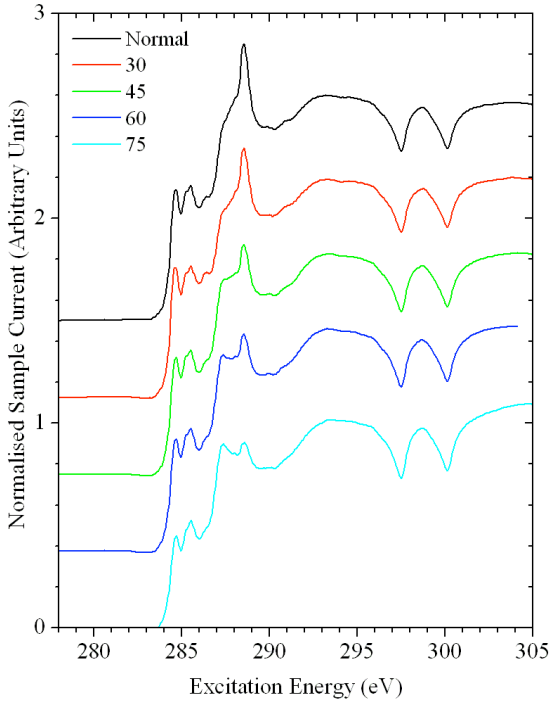

Figure 11.6: C *1s* NEXAFS TEY spectra of 1:2 (liquid volume fractions) of drop-cast 4(HPBT)/PCBM films. A vertical offset is added for clarity.

The above assumption is further borne out by the TFY spectra of the 1:2 film displayed in Figure 11.7. The peak at 288.3 eV, which we now tentatively associate with the 4(HPBT):PCBM interface, is more prominent than in the TFY spectra of the 1:1 film

(Figure 11.5), but has a lesser relative contribution than in the TEY spectra of the 1:2 film in Figure 11.6. Furthermore, the relative intensity of this peak does not change as a function of the angle of incidence, even at very grazing angles. This observation is significant, as it confirms that the peak is not a property of the bulk of the PCBM film, the spectral signature of which decreases as the angle of incidence is increased. At the most-grazing angle of incidence a convergence of sorts is achieved, and the TEY and TFY spectra have the same shape. At this angle, the measuring depth of the TFY measurements has approached the mean free path of the escaping photoexcited electrons, and so the region of the sample that is measured by both methods is the same. The overall decrease in the intensity of the 288.3 eV feature in the TEY spectra upon going to more grazing angles of incidence also suggests that it is not caused simply by surface contamination, as it would be expected to contribute more to the overall spectra in that case, unless the surface contamination had a strong orientation-related effect that overcompensates for the effect of changing penetration depth.

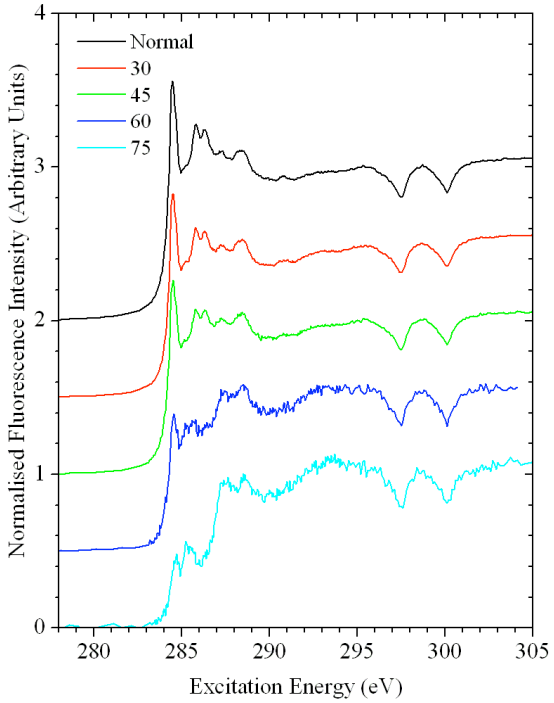

Figure 11.7: C *1s* NEXAFS TFY spectra of 1:2 (liquid volume fractions) of drop-cast 4(HPBT)/PCBM films. A vertical offset is added for clarity.

The effect of increasing the relative concentration of 4(HPBT) in the blends is, in light of the previous discussion, predictable. Compared to the TFY spectra shown in Figure 11.5 and Figure 11.7, the TFY spectra of the 2:1 films, displayed in Figure 11.8, have a larger contribution from the 4(HPBT) spectral signature; this is seen in the decreased ratio of the intensity of the main π* absorption resonance (284.5 eV) to that of the peak at 287.3 eV, as well as in the greater prominence of the 285.5 eV peak. The angular dependence of the peak ratios does not follow a trend; further studies will be needed to determine the reproducibility of these results before any conclusions can be drawn. The TEY spectra (not shown) are effectively indistinguishable from those measured from the pure 4(HPBT) film (Figure 10.3), except that the magnitude of the angle-dependent effects is significantly reduced.

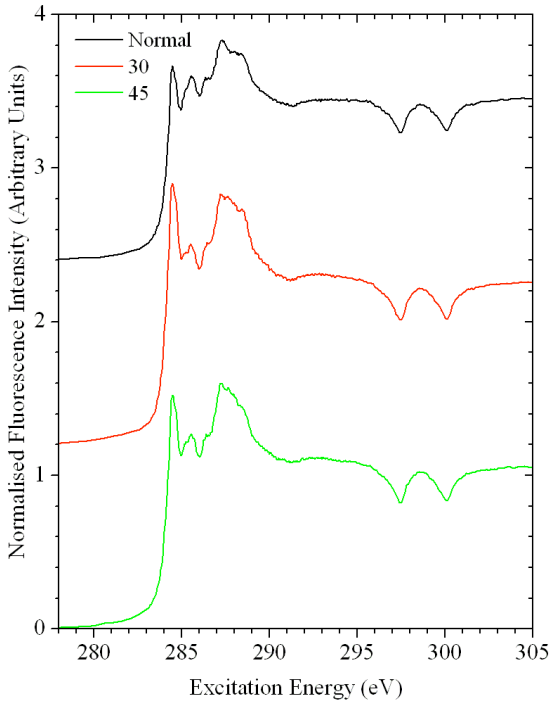

Figure 11.8: C *1s* NEXAFS TFY spectra of 2:1 (liquid volume fractions) of drop-cast 4(HPBT)/PCBM films. A vertical offset is added for clarity.

11.2.2. C *1s* NEXAFS of Annealed Samples

In order to determine what effect, if any, annealing the samples had on their NEXAFS spectra, all of the films discussed above were heated to 125°C in air for approximately one hour, and then were remeasured. The powdered PCBM and 4(HPBT) samples were also annealed at the same time for reference purposes. The results of this experiment were not conclusive, but there is enough evidence of annealing-induced structural modification that we feel it should be included in a systematic study of the blend samples.

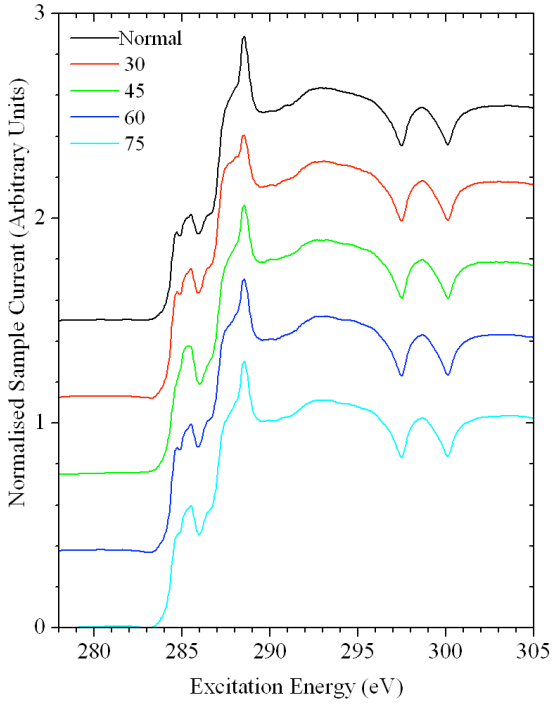

Figure 11.9: C *1s* NEXAFS TEY spectra of 1:1 (liquid volume fractions) of drop-cast 4(HPBT)/PCBM films after annealing at 125°C for one hour. A vertical offset is added for clarity.

A striking effect of annealing is observed in the C *1s* NEXAFS spectra of the 1:1 4(HPBT) and PCBM blend samples, shown in Figure 11.9. There are three main changes in the spectra that can be attributed to annealing: broadening of the sharp π* resonance features below 286 eV, diminished angle-dependence of the peak ratios, and the emergence of the prominent feature at 288.3 eV, which we have argued is characteristic

of the interface region in the bilayer film. At this point it must be reiterated that we have not identified the specific chemical group that leads to this feature, and that the possibility of surface contamination cannot be discounted, especially when the feature's position in the region in which carbonyl resonances often arise is considered.

Caveats aside, however, the spectra suggest that the annealing process has a significant effect on the structure of the 4(HPBT) layer. After annealing, the spectra of the 1:1 films closely resemble those of the 1:2 films shown in Figure 11.6. This similarity suggests the possibility that the annealing removes 4(HPBT) from the surface of the films, leaving a much thinner top layer, leading to an increased spectral signature from the interface region. This is likely to be the case, as temperature programmed desorption (TPD) has been used in the past to produce thin films of organic materials from thicker films [106,138]. It is possible that the feature is associated with heat-induced structural degradation of the 4(HPBT), but annealing the 4(HPBT) powder and films of 4(HPBT) does not have the same effect on their spectra. The spectra of the annealed 4(HPBT) spectra displayed in Figure 11.10 do show a peak near this energy, at 288.6 eV, but it is not nearly as prominent as the one in the annealed blend sample, and also does not show a variation in intensity as a function of incidence angle; the appearance of increasing prominence is associated with the reduction in the intensity of the prominent resonance at 287.3 eV.

The reproducibility of the spectra shown in Figure 11.10 must be ascertained before any firm conclusions can be drawn; the shape of the spectrum measured at 60° incidence is consistent with the effects of radiation damage shown in Figure 10.8, and the likelihood that a previously-irradiated spot was measured increases dramatically at grazing incidence because of the associated increase in the spot size.

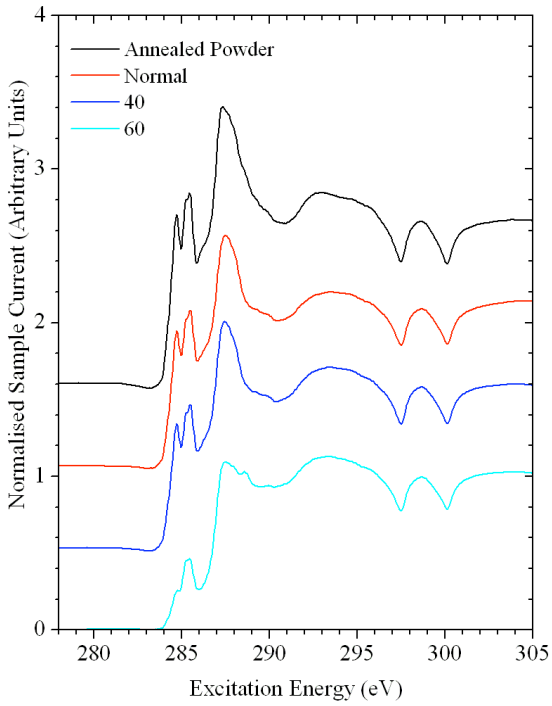

Figure 11.10: C *1s* NEXAFS TEY spectra of drop-cast 4(HPBT) films and powdered reference sample after annealing at 125°C for one hour. A vertical offset is added for clarity.

If we assume that the annealing causes ablation of the 4(HPBT) surface, as is suggested by the spectra of the annealed blend samples, then the spectra of the annealed samples in Figure 11.10 should represent the electronic structure of a thin layer of 4(HPBT), perhaps approaching a monolayer, on a metallic surface. If this is the case, then the peak at 288.6 eV can still be assumed to represent the interface region, except in this case the interface is with the indium surface rather than with the PCBM layer. It should also be noted, however, that this feature may be associated with the In surface itself; it cannot be determined whether the surface was completely free of carbon contamination prior to the deposition of the film. The indium surface was scraped with a scalpel blade under a fume hood immediately before the film was deposited, but there may still have been some contamination. A study of the TPD properties of the blended material may also be of interest: if the amount of 4(HPBT) that can be removed from the surface reaches

saturation before it is removed completely, this may be considered as evidence for the formation of bulk heterojunctions in the 4(HPBT)/PCBM devices.

11.3. Conclusions

The degree of intermixing between the PCBM and 4(HPBT) could not be determined using the spectroscopic methods, but there was clear evidence that the films formed by casting a mixture of the materials from solution had a bilayer structure in which the PCBM was adjacent to the substrate. The dichroic signal of the 4(HPBT) in the mixture was suppressed in comparison to what was observed in the pure 4(HPBT) films (Figure 10.3). Annealing the samples appeared to cause desorption of 4(HPBT) from the surface, suggesting that the structure of the films could be controlled by *in situ* techniques for further experiments. An unexplained feature observed in the NEXAFS spectra may indicate the nature of the chemical interaction at the interface between the materials; a dedicated study will be needed to verify the association of this feature with the interface and produce a model of the interaction.

12. Summary and Directions for Future Research

This section is broken up into several subsections according to the main themes of the various studies, including the examination of radiation damage effects in molecules, the measurement of band gaps and HOMO-LUMO gaps using soft X-ray spectroscopy, and the use of NEXAFS spectroscopy – and angle-resolved NEXAFS in particular – in the study of molecular semiconductor materials.

12.1. Radiation Damage Summary

The study of radiation damage in glycine revealed that the onset of damage occurred almost immediately upon irradiation. The primary decay mechanism was the partial or complete removal of the carbonyl group from the molecule. The remaining fragment of glycine reacted with adjacent molecules to form peptides. There was also evidence for the formation of small amounts of HCN or other nitriles. The need for numerical simulations in the analysis of the measured spectra led to refinement of these techniques, and as a whole the study has led to increased awareness of the effects of beam damage on organic materials, which will improve the experimental methodology employed in future studies.

This study provides a clear indication that a great deal of care must be taken to minimize and account for radiation damage in soft X-ray experiments, but also indicates that not all molecules are equally susceptible to damage. Clearly, molecules that lack a carbonyl group will be less sensitive than molecules that contain this group. This conclusion was supported by the study of radiation damage in the molecular semiconductor 4(HPBT), which was largely resistant to such damage.

12.2. Further Studies of Radiation Damage

There are several possible ways that the glycine radiation damage experiment could be continued, improved, or expanded on. The most obvious possibility is to simply repeat the study with other molecules, possibly including other amino acids. This would indeed build upon the current study, but there are more interesting areas of research that could be pursued. For example, irradiation of a single crystal of glycine, or of another suitable molecule, may lead to trapped radicals in quantities sufficient to detect using NEXAFS;

the EPR studies referenced earlier were based upon the creation of such radicals using much lower levels of irradiation, and after a period of time had elapsed between irradiation and detection. An *in situ* study using high levels of soft X-rays may be able to expand upon those findings, and also serve as a test case for the use of StoBe in the modelling of open-shell materials.

Relaxation effects should be examined to confirm some of the assumptions regarding which products were unstable. The experiment would be quite simple, as it would only require that the experiment above be repeated and the sample be left in vacuum with the photon shutters closed for a period of time before being remeasured. Any changes in the spectral lineshape would be analysed in terms of possible reactions among the proposed product molecules. In addition, another interesting experiment would involve studying the effects of relaxation time on the early stages of radiation damage. It was clear that irradiation had a significant and immediate effect on the glycine sample; a follow-up experiment would involve repeating the first few quick N *1s* NEXAFS scans of the π* region, allowing a period of relaxation with the beam turned off, and then continuing the measurement. Several outcomes are possible, including complete self-repair in which the glycine returns to zwitterionic form, a progression toward the structure that would have resulted if the experiment had continued, or the formation of entirely different substances.

A practical extension of the radiation damage study would be the evaluation of methods that could be used to mitigate or eliminate it from the experiment. Beyond obvious methods revolving around minimising the radiation dose received by the part of the material being measured, there are other possibilities that could be examined. The use of cryostats is successful in controlling radiation damage in hard X-ray experiments, but it is less clear if this is the case in soft X-ray measurements. There are a few reasons why lowering the temperature of the sample would be less effective in soft X-ray measurements, chief among them being the low interaction volume of soft X-rays. All of the X-rays are absorbed very near the surface of the sample – providing of course that it is not an extremely thin film – and so the transfer of heat away from the location of the potential damage would not occur nearly fast enough to have any effect on the process.

The effect of radiation damage on thin films that are protected by a layer of, for example, gold, would also be an interesting area of study. It is possible to obtain very good measurements of such samples using fluorescence yield modes, and it is possible that the Au layer may have stabilising effects on the film. Conversely, it is equally possible that the relatively weak bonds between the film and the Au layer could be broken due to the action of the irradiation; a thin enough layer of gold could theoretically be removed entirely though these means. If this is the case, then it would suggest a possible technique for the introduction of reactive materials into vacuum: rather than attempting to keep them in an inert atmosphere until they can be loaded into the beamline, they could be coated with a thin protective layer that could then be removed by ablation by soft X-rays.

12.3. Molecular Semiconductor Summary

The study of the organic photovoltaic and organic light-emitting diode materials led to the development of new techniques, and also provided insight into possible structure-function relationships in the materials. The study of the star-shaped oligothiophene molecule 4(HPBT) showed that it had an almost perfectly upright orientation in the form of a relatively thick film on an amorphous substrate. The knowledge of the orientation is significant, as the charge transfer properties of such materials is known to be highly anisotropic.

It was observed that when 4(HPBT) was blended with the hole-transporting fullerene-based molecule, PCBM, the deposited film formed a bilayer structure with the 4(HPBT) forming a cohesive layer on top of the PCBM. There was, however, some evidence of chemical reactions between the two materials, which may have been enhanced by annealing of the samples. The source of the enhancement could have been related to desorption of 4(HPBT) from the surface of the films, which was suggested by the absorption measurements.

12.4. Further Studies in Molecular Semiconductors

There are several ways in which the study of 4(HPBT) and related materials could be improved and expanded upon, many of which were alluded to in the body of the analysis.

The suggestions given below are not simply of academic interest; the current research will be continued, expanded upon, and hopefully improved by Paul Bazylewski, a graduate student who is beginning his studies under the supervision of Dr. Gap Soo Chang at the University of Saskatchewan.

The most significant and most necessary improvements will come in the form of improved sample preparation procedures, the experimental procedures having already been well-established. Better knowledge of and control over the thickness of the films and their surface morphology will remove a great deal of uncertainty from the spectroscopic studies. These goals will be aided by preparing the samples using a spin-coating apparatus that will be located in the Physics department. Preparing samples on a variety of substrates, including well-defined crystal planes, molecular surfaces, and amorphous substrates will allow the behaviour of various molecules that are subjected to varying strengths of sample-substrate interaction to be examined. Temperature programmed desorption measurements, in which a residual gas analyser or a mass spectrometer is used to study the desorption of materials from a surface as a function of annealing temperature would be of great use in the study of blended samples such as those that were studied here. A benefit of this sort of analysis would be to give a better understanding of what structural modifications could be induced *in situ* during the course of a set of synchrotron measurements.

Further study into 4(HPBT) and several related materials synthesized by Dr. Choi's group at Korea University may provide valuable structure-function information. Two avenues for inquiry are the exploration of any dependence of the dichroic signal on small changes to the structure of the oligothiophene groups in the molecules, and a study of the structure of the trinary films made from 4(HPBT), PCBM, and P3HT. The first topic is important, because the initial study of 4(HPBT) and related molecules found a significant variation in their device parameters, and any observation of changes in the orientation of the molecules would provide a great deal of insight into their charge transport mechanisms. The second topic is a natural extension of the study of the blended samples contained here. The addition of the molecular semiconductor P3HT to the mixture from which the films are cast was shown to improve the device efficiency. The same

methodology that was used in the current study to uncover evidence of the layered structure of the binary films could be used to determine the location of P3HT in the trinary films. This knowledge would be of great help in tailoring the composition of films to improve their functionality.

12.5. Electronic Gap Determination Summary

Methods for probing both the band gaps in solid state materials and the HOMO-LUMO gaps in molecular materials were developed and tested. Derivatives of measured spectra were used to locate the onset of the density of states in solid state materials and the centres of features arising from orbital transitions in molecular materials. The method used to determine the band gaps in solid state samples is based on the comparison of fluorescence yield measurements, giving it the advantage of bulk-sensitivity. This property can either be exploited in comparisons of the surface and bulk of a material, or it can be used to eliminate the need to avoid surface contamination and oxidation of reactive samples.

The method used to determine the HOMO-LUMO gaps in molecular materials was shown to agree well with the results of optical measurements for three different systems: pentacene, TBPe, and 4(HPBT). While it is not possible to achieve the same level of resolution that can be obtained in optical measurements, the information provided in XES/NEXAFS studies has several advantages, such as site-selectivity, element-selectivity, and symmetry-selectivity. The optical and soft X-ray measurements are therefore quite complementary, as the low-resolution/high-selectivity X-ray measurements provide access to information that cannot be determined from the high-resolution/low-selectivity optical measurements.

An unexpected and interesting dependence of the shape of X-ray excited optical luminescence (XEOL) spectra was observed, namely the enhancement of scattering processes that occurs when exciting off resonance, and the extinction of those processes when exciting on sharp absorption resonances. This observation is an interesting corollary of the scattering processes that lead to energy-loss features in RIXS spectra and

their relationship with the competing processes of normal fluorescence, suggesting that further studies relating the two may be of interest.

A refinement of the technique used for calibration of X-ray emission data was developed in the course of this study; it has become part of the standard post-processing procedure for measurements taken using the soft X-ray fluorescence spectrometer at Beamline 8.0.1 at the Advanced Light Source, and has led to the calibration procedure being included in the user interface software for the REIXS spectrometer that will be located at the Canadian Light Source.

12.6. Further Studies in Electronic Gap Determination

There are several ways that the methods developed above can be improved upon, and in fact significant progress to this end has already been made in the work of Teak Boyko, a graduate student working with Dr. Alex Moewes at the University of Saskatchewan. The major advancement involves significantly improved theoretical support for the measurements, provided via in-house simulations of the density of states and soft X-ray spectra of solid state materials using the Wien2k DFT code. These calculations allow the nature of the band gap to be understood in much greater detail, including the study of direct and indirect band gaps, the magnitude and nature of the core hole effect, and any site- or symmetry-resolved variations in the band gap.

Improvements in the X-ray excited optical luminescence measurements can be obtained by a rigorous pursuit of a theoretical model to describe and predict the transitions involved, which has been lacking in most XEOL studies to date. The pursuit of this model will be aided by improvements to the measurement method, most notably the development of time-resolved XEOL (TR-XEOL), which is one of the major focuses of the beamlines associated with Dr. T.K. Sham's group at the university of Western Ontario. The addition of time-resolved measurements will allow the contributions from various processes to be examined separately; for example it would be expected that the scattering processes that we propose to explain the vibronic structure observed in XEOL spectra would occur on a faster time scale than would luminescence processes based on the creation of valence holes through refilling of the core hole by a series of cascading

transitions. In general, the development of time-resolved measurements will be of great benefit to a number of spectroscopic techniques at synchrotron light sources – the same argument that was just made regarding the benefits of TR-XEOL measurements could be applied equally well to XES and RIXS measurements.

References

1. Stöhr, J. *NEXAFS Spectroscopy* (Springer-Verlag, Berlin, 1996).

2. Chretien, S.; Salahub, D.R. in *Atomic Clusters and Nanoparticles* (New York, 2001).

3. Cramer, C.J. *Essentials of Computational Chemistry: Theories and Models* (J. Wiley and Sons Ltd., West Sussex, England, 2002).

4. Hohenberg, P.; Kohn, W. *Physical Review* **136**, B864 (1964).

5. Kohn, W.; Sham, L. *Physical Review* **140**, A1133 (1965).

6. Hermann, K.; Pettersson, L.G.M.; Casida, M.E.; Daul, C.; Goursot, A.; Koester, A.; Proynov, E.; St-Amant, A.; Salahub., D.R.; Contributing Authors: Carravetta, V.; Godbout, N.; Guan, J.; Jamorski, C.; Leboeuf, M.; Malkin, V.; Malkina, O.; Nyberg, N.; Pedocchi, L.; Sim, F.; Triguero, L.; Vela, A. StoBe Software, *StoBe-demon version 2.1* (2005).

7. Hermann, K.; Pettersson, L. *Documentation for StoBe2005 (version 2.1)* (2005).

8. Salahub, D.R.; Castro, M.E.; Proynov, E.I. in *Relativistic and electron Correlation Effects in Molecules and Solids*, **318**, edited by Malli, G.L. (Plenum Press, New York, 1994).

9. Perdew, J.; Wang, Y. *Physical Review B* **33**, 8800 (1986).

10. Sahni, V.; Gruenebaum, J.; Perdew, J. *Physical Review B* **26**, 4371 (1982).

11. Perdew, J. *Physical Review Letters* **55**, 1665 (1985).

12. Perdew, J. *Physical Review B* **33**, 8822 (1986).

13. Becke, A. *Physical Review A* **38**, 3098 (1988).

14. Huzinaga, S.; Andzelm, J.; Klobukowski, M.; Radzio-Andzelm, E.; Sakai, Y.; Tatewaki, H. *Gaussian Basis Sets for Molecular Calculations*; Elsevier: Amsterdam (1984).

15. Attwood, D. *Soft X-rays and Extreme Ultraviolet Radiation*, Cambridge, New York, (1999).

16. http://www.als.lbl.gov/als/curves/index.html *Bend Magnet* (downloaded April 2009).

17. http://commons.wikimedia.org/wiki/File:Undulator.png *Undulator* (downloaded April 2009).

18. Regier, T.; Krochak, J.; Sham, T.K.; Hu, Y.F.; Thompson, J.; Blyth, R.I.R. *Nuclear Instruments & Methods in Physics Research A* **582**, 93 (2007).

19. Jia, J.J.; Callcott, T.A.; Yurkas, J.; Ellis, A.W.; Himpsel, F.J.; Samant, M.G.; Stöhr, J.; Ederer, D.L.; Carlisle, J.A.; Hudson, E.A.; Terminello, L.J.; Shuh, D.K.; Perera, R.C.C. *Review of Scientific Instruments* **66**, 1394 (1995).

20. http://www.als.lbl.gov/als/als_users_bl/8.0.1-Overview.pdf, *High Resolution and Flux for Materials and Surface Science, Beamline 8.0.1*, (downloaded April 2009).

21. Thompson, A.C.; Vaughan, D. (*ed.*) *X-ray Data Booklet* (2001).

22. http://www.als.lbl.gov/als/als_users_bl/8.0.1-SXF.pdf, *Soft X-ray Fluorescence (SXF) Spectrometer, Beamline 8.0.1* (downloaded April 2009).

23. Henke, B.; Gullikson, E.; Davis, J. *Atomic Data and Nuclear Data Tables* **54** 181 (1993).

24. von Barth, U.; Grossman, G. *Solid State Communications* **32**, 645 (1979).

25. Mahan, G.D. *Physical Review B* **21**, 1421 (1980).

26. Calcott, T.A., in *Vacuum Ultraviolet Spectroscopy II (Experimental Methods in the Physical Sciences)*, edited by Sampson, J.A. and Ederer, D.L. **132** (Academic Press, San Diego, 1998).

27. Krause, M. *Journal of Physical and Chemical Reference Data* **8**, 307 (1979).

28. Sakurai, J.J. *Advanced Quantum Mechanics* (Addison-Wesley, U.S.A. 1967).

29. De Groot, F.M.F.; Kotani, A. *Core Level Spectroscopy of Solids* (Taylor and Francis CRC Press, U.S.A. 2008).

30. Carlisle, J.A.; Blankenship, S.R.; Terminello, L.J.; Jia, J.J.; Callcott, T.A.; Ederer, D.L; Perera, R.C.C.; Himpsel, F.J. *Journal of Electron Spectroscopy and Related Phenomena* **110**, 323 (2000).

31. Fomichev, V.A.; Rumsh, M.A. *Journal ofPhysics and Chemistry of Solids* **29**, 1015 (1968).

32. Denlinger, J.D. *Unpublished Work*, (2005).

33. Bearden, J.A. *Reviews of Modern Physics* **39**, 78 (1967).

34. Ravel, B.; Newville, M. *Journal of Synchrotron Radiation* **12**, 537 (2005).

35. Beauchemin, S.; Hesterberg, D.; Beauchemin, M. *Soil Science Society of America Journal* **66**, 83 (2002).

36. Ressler, T.; Wong, J.; Roos, J.; Smith, I.L. *Environmental Science and Technology* **34**, 950 (2000).

37. Fay, M.J.; Proctor, A.; Hoffman, D.P.; Hooualla, M.; Hercules, D.M. *Mikrochimica Acta* **109**, 281 (1992).

38. Fernández-García, M.; Márquez Alvarez, C.; Haller, G.L. *Journal of Physical Chemistry* **99**, 12565 (2002).

39. Lerotic, M.; Jacobsen, C.; Shäfer, T.; Vogt, S. *Ultramicroscopy* **100**, 35 (2004).

40. Kim, P.-S.G.; Naftel, S.J.; Sham, T.K.; Coulthard, I.; Hu, Y.-F.; Moewes, A.; Freeland, J.W. *Journal of Electron Spectroscopy and Related Phenomena* **144-147**, 901 (2005).

41. Heigl, F.; Lam, S.; Regier, T.; Coulthard, I.; Sham, T.K. *Journal of the American Chemistry Society* **128**, 3906 (2006).

42. Peltekis, N.; Holland, B.N.; Krishnamurthy, S.; McGovern, I.T.; Poolton, N.R.J.; Patel, S.; McGuinness, C. *Journal of the American Chemical Society* **130**, 13008 (2008).

43. Emura, S.; Moriga, T.; Takizawa, J.; Nomura, M.; Bauchspiess, K.R.; Murata, T.; Harada, K.; Maeda, H. *Physical Review B* **47**, 6918 (1993).

44. Evans, D.A.; Vearey-Roberts, A.R.; Poolton, N.R.J. *Applied Physics Letters* **89**, 161107 (2006)

45. Hessel, C.M.; Henderson, E.J.; Kelly, J.A.; Cavell, R.G.; Sham, T.K.; Veinot, J.G.C. *Journal of Physical Chemistry C* **112**, 14247 (2008).

46. Murphy, M.W.; Zhou, X.T.; Ko, J.Y.P.; Zhou, J.G.; Heigl, F.; Sham, T.K. *Journal of Chemical Physics* **130**, 084707 (2009).

47. Slater, J.C.; Johnson, K.H. *Physical Review B* **5**, 844 (1972).

48. Nilsson, A.; Mårtensson, N. *Physica B* **208-209**, 19 (1995).

49. Kutzelnigg, W.; Fleischer, U.; Shindler, M. In *NMR-Basic Principles and Progress*; Springer-Verlag: New York, **23**, 165 (1990).

50. Cavalleri M.; Odelius, M.; Nordlund, D.; Nilsson, A.; Pettersson, L.G.M. *Physical Chemistry Chemical Physics* **7**, 2854 (2005).

51. Bonazzola, L.; Iacona, C.; Michaut, J.; Roncin, J. *Journal of Chemical Physics* **73**, 4175 (1980).

52. Hedberg, A. and Ehrenberger, A. *Journal of Chemical Physics* **48**, 4822 (1968**)**.

53. Morton, J. *Journal of the American Chemical Society* **86**, 2325 (1964).

54. Sagstuen, E.; Sanderud, A.; Hole, E. *Radiation Research* **162**, 112 (2004).

55. Sanderud, A.; Sagstuen, E. *Journal of Physical Chemistry B* **102**, 9353 (1998).

56. Ban, F.; Gauld, J.; Boyd, R. *Journal of Physical Chemistry A* **104**, 5080 (2000).

57. Pauwels, E.; Van Speybroeck, V.; Waroquier, M. *Journal of Physical Chemistry A* **108**, 11321 (2004).

58. Jonsson, M., Kraatz, H.-B. *J. Chem. Soc., Perk. Trans.* **2,** 2675 (1997).

59. Zubavichus, Y.; Fuchs, O.; Weinhardt, L.; Heske, C.; Umbach, E.; Denlinger, J. D.; Grunze, M. *Rad. Res.* **161**, 346 (2004).

60. Zubavichus, Y.; Zharnikov, M.; Shaporenko, A.; Fuchs, O.; Weinhardt, L.; Heske, C.; Umbach, E.; Denlinger, J. D.; Grunze, M. *Journal of Physical Chemistry A **108***, 4557 (2004).

61. Wang, J.; Morin C.; Li, L.; Hitchcock, A.P.; Scholl A.; Doran, A.; *Journal of Electron Spectroscopy and Related Phenomena* (in press 2008**)**, doi:10.1016/j.elspec.2008.01.002

62. Rightor, E.G.; Hitchcock, A.P.; Ade, H.; Leapman, R.D.; Urquhart, S.G.; Smith, A.P.; Mitchell, G.; Fischer, D.; Shin, H.J.; Warwick, T. *Journal of Physical Chemistry B* **101**, 1950 (1997).

63. Kaznacheyev, K.; Osanna, A.; Jacobsen, C.; Plashkevych, O.; Vahtras, O.; Agren, H. *Journal of Physical Chemistry B* **106**, 3153 (2002).

64. Gordon, M. L.; Cooper, G.; Morin, C.; Araki, T.; Turci, C. C.; Kaznatcheev, K.; Hitchcock, A. P. *Journal of Physical Chemistry A* **107**, 6144 (2003).

65. Cooper, G.; Gordon, M.; Tulumello, D.; Turci, C.; Kaznatcheev, K.; Hitchcock, A. R. *Journal of Electron Spectroscopy and Related Phenomena* **137-140**, 795 (2004).

66. Zubavichus, Y.; Zharnikov, M.; Schaporenko, A.; Grunze, M. *Journal of Electron Spectroscopy and Related Phenomena* **134**, 25 (2004).

67. Zubavichus, Y.; Shaporenko, A.; Grunze, M.; Zharnikov, M. *Journal of Physical Chemistry A* **109**, 6998 (2005).

68. Zubavichus, Y.; Shaporenko, A.; Grunze, M.; Zharnikov, M. *Journal of Physical Chemistry B* **110**, 3420 (2006).

69. Nyberg, M.; Hasselström, J.; Karis, O.; Wassdahl, N.; Weinelt, M.; Nilsson, A.; Pettersson, L. G. M. *Journal of Chemical Physics* **112**, 5420 (2000).

70. Nyberg, M.; Odelius, M.; Nilsson, A.; Pettersson, L. G. M. *Journal of Chemical Physics* **119**, 12577 (2003).

71. Hasselström, J.; Karis, O.; Nyberg, M.; Pettersson, L. G. M.; Weinelt, M.; Wassdahl, N.; Nilsson, A. *Journal of Physical Chemistry B* **104**, 11480 (2000).

72. Hasselström, J.; Karis, O.; Weinelt, M.; Wassdahl, N.; Nilsson, A.; Nyberg, M.; Pettersson, L. G. M.; Samant, M. G.; Stöhr, J. *Surface Science* **407**, 221 (1998).

73. Plashkevych, O.; Carravetta, V.; Vahtras, O.; Agren, H. *Chem. Phys.* **232**, 49 (1998).

74. Messer, B.M.; Cappa, C.D.; Smith, J.D.; Wilson, K.R.; Gilles, M.K.; Cohen, R.C.; Saykally, R.J., *Journal of Physical Chemistry B* **109**, 5375 (2005).

75. Langan, P.; Mason, S.A.; Myles, D.; Schoenborn, B.P. *Acta Crystallographica* **B58**, 728 (2002).

76. George, G. N. *EXAFSPAK: A Suite of Programs for Analysis of X-ray Absorption Spectra* (2000).

77. Aziz, E.F.; Gråsjö, J.; Forsberg, J.; Andersson, E.; Söderström, J.; Duda, L.; Zhang, W.; Yang, J.; Eisebitt, S.; Bergström, C.; Luo, Y.; Nordgren, J.; Eberhardt, W.; Rubensson, J.E. *Journal of Physical Chemistry A* **111**, 9662 (2007).

78. Gillespie, A.W.; Walley, F.L.; Farrell, R.E.; Regier T.; Blyth, R.I.R. *Journal of Synchrotron Radiation* **15**, 532 (2008).

79. MacNaughton, J.B.; Moewes, A.; Lee, J.S.; Wettig, S.D.; Kraatz, H.-B.; Ouyang, L.Z.; Ching, W.Y.; Kurmaev, E.Z. *Journal of Physical Chemistry B* **110**, 15742 (2006).

80. MacNaughton, J.B.; Moewes, A.; Kurmaev, E.Z. *Journal of Physical Chemistry B* **109**, 7749 (2005).

81. Van Buuren, T.; Dinh, L.N.; Chase, L.L.; Siekhaus, W.J.; Terminello, L.J. *Physical Review Letters* **80**, 3803 (1998).

82. Lüning, J.; Rockenberger, J.; Eisebett, S.; Rubensson, J.-E.; Karl, A.; Kornowski, A.; Weller, H.; Eberhardt, W. *Solid State Communications* **112**, 5 (1999).

83. Leitch, S.; Moewes, A.; Ouyang, L.; Ching, W.Y.; Sekine, T. *Journal of Physics: Condensed Matter* **16**, 6469 (2004).

84. Boyko, T.; Kasap, S.; Johanson, R.; Kobayashi, S.; Aoki, T.; Moewes, A. *Physica Status Solidi A* **206**, 935 (2009).

85. Bär, M.; Nishiwaki, S.; Weinhardt, L.; Pookpanratana, S.; Fuchs, O.; Blum, N.; Yang, W.; Denlinger, J.D.; Shafarman, W.N.; Heske, C. *Applied Physics Letters* **93**, 244103 (2008).

86. McGuinness, C.; Fu, D.; Downes, J.E.; Smith, K.E.; Hughes, G.; Roche, J. *Journal of Applied Physics* **94**, 3920 (2003).

87. Muramatsu, Y.; Hayashi, T.; Perera, R.C.C. *Journal of Electron Spectroscopy and Related Phenomena* **104**, 155 (1999).

88. Chiou, J.W.; Tsai, H.M.; Pao, C.W.; Chien, F.Z.; Pong, W.F.; Chen, C.W.; Tsai, M.-H.; Wu, J.J.; Ko, C.H.; Chiang, H.H.; Lin, H.J.; Lee, J.F.; Guo, J.H. *Journal of Applied Physics* **104**, 013709 (2008).

89. van Elp, J.; Potze, R.H.; Eskes, H.; Berger, R.; Sawatzky, G.A. *Physical Review B* **44**, 1530 (1991).

90. Kurmaev, E.Z.; Wilks, R.G.; Moewes, A.; Finkelstein, L.D.; Shamin, S.N.; Kuneš *Physical Review B* **77**, 165127 (2008).

91. Terakura, K.; Oguchi, T.; Williams, A.R.; Kübler, J. *Physical Review B* **30**, 4734 (1984).

92. Dobysheva, L.V.; Potapov, P.L.; Schryvers, D. *Physical Review B* **69**, 184404 (2004).

93. J. Kuneš, V. I. Anisimov, A. V. Lukoyanov, and D. Vollhardt, *Physical Review B* **75**, 165115 (2007).

94. P. Wei and Z.Q. Qi, *Physical Review B* **49**, 10864 (1994).

95. J. van Elp, J.L. Wieland, H. Eskes, P. Kuiper, G.A. Sawatzky, F.M.F. de Groot, T.S. Turner, *Physical Review B* **44**, 6090 (1991).

96. Schiefer, S.; Huth, M.; Dobrinevski, A.; Nickel, B. *Journal of the American Chemical Society* **129**, 10316 (2007).

97. Kim, S.S.; Park, S.P.; Kim, J.H.; Im, S. *Thin Solid Films* **420-421**, 19 (2002).

98. Park, S.P.; Kim, S.S.; Kim, J.H.; Whang, C.N.; Im, S. *Applied Physics Letters* **80**, 2872 (2003).

99. Puigdollers, J.; Voz, C.; Orpella, A.; Martin, I.; Vetter, M.; Alcubilla, R. *Thin Solid Films* **427**, 167 (2003).

100. Mi, B.X.; Gao, Z.Q.; Lee, C.S.; Lee, S.T.; Kwong, H.L.; Wong, N.B. *Applied Physics Letters* **75**, 4055 (1999).

101. Shi, J.; Tang, C.W. *Applied Physics Letters* **80**, 3201 (2002).

102. Su, Z.; Li, W.; Chu, B.; Zhu, J.; Wang, D.; Han, L.; Li, X.; Be, De.; Chen, Y.; Li, B. *Journal of Applied Physics* D **41**, 125108 (2008).

103. Wilks, R.G.; Sham, T.K., Ko, J.Y.; Liu, L.; Zhang, J.-X.; Moewes, A. (*to be published*).

104. Yuan, Q.; Mannsfeld, S.C.B.; Tang, M.L.; Toney, M.F.; Lüning, J.; Bao, Z. *Journal of the American Chemical Society* **130,** 3502 (2008).

105. Casu, M.B.; Cosseddu, P.; Batchelor, D.; Bonfiglio, A.; Umbach, E. *Journal of Chemical Physics* **128**, 014705 (2008).

106. Casu, M.B.; Yu, X.; Schmitt, S.; Heske, C.; Umbach, E. *Journal of Chemical Physics* **129**, 244708 (2008).

107. Stöhr, J. Gland, J.L.; Kollin, E.B.; Koestner, R.J.; Johnson, A.L.; Muetterties, E.L.; Sette, F. *Physical Review Letters* **53**, 2161 (1984).

108. Biswas, I.; Peisert, H.; Nagel, M.; Casu, M.B.; Schuppler, S.; Nagel, P.; Pellegrin, E.; Chassé, T. *Journal of Chemical Physics* **126**, 174704 (2007).

109. Kera, S.; Casu, M.B.; Bauchspiess, K.R.; Batchelor, D.; Schmidt, Th.; Umbach, E. *Surface Science* **600** 1077 (2006).

110. deLongchamp, D.M; Sambasivan, S.; Fischer, D.A.; Lin, E.K.; Chang, P.; Murphy, A.R.; Fréchet, J.M.J.; Subramanian, V. *Advanced Materials* **17**, 2340 (2005).

111. DeLongchamp, D.M.; Ling, M.M.; Jung, Y.; Fischer, D.A.; Roberts, M.E.; Lin, E.K.; Bao, Z. *Journal of the American Chemical Society* **128**, 16579 (2006).

112. DeLongchamp, D.M.; Kline, R.J.; Lin, E.K.; Fischer, D.A.; Richter, L.J.; Lucas, L.A.; Heeney, M.; McCulloch, I.; Northrup, J.E. *Advanced Materials* **19**, 833 (2007).

113. Casu, M.B.; Biswas, I.; Schuster, B.-E.; Nagel, M.; Schuppler, S.; Chassé *Applied Physics Letters* **93**, 024103 (2008).

114. Friend, R.H.; Denton, G.J.; Halls, J.J.M.; Harrisn, N.T.; Holmes, A.B.; Köhler, A.; Lux, A.; Moratti, S.C.; Pichler, K.; Tessler, N.; Towns, K.; Wittmann, H.F. *Solid State Communications* **102**, 249 (1997).

115. Cornil, J.; Heeger, A.J.; Bredas, J.L. *Chemical Physics Letters* **272**, 463 (1997).

116. Ostrick, J.R.; Dodabalapur, A.; Torsi, L.; Lovinger, A.J.; Kwock, E.W.; Miller, T.M.; Galvin, M.; Berggren, M.; Katz, H.E. *Journal of Applied Physics* **81**, 6804 (1997).

117. Venkataraman, L.; Klare, J.E.; Nuckolls, C.; Hybertsen, M.S.; Steigerwald, M.L. *Nature* **442**, 904 (2006).

118. Liu, A.C.; Stöhr, J.; Friend, C.M.; Madix, R.J. *Surface Science* **235**, 107 (1990).

119. Solomon, J.L.; Madix, R.J.; Stöhr, J. *Surface Science* **255**, 12 (1991).

120. Witkowski, N.; Hennies, F.; Pietzsch, A.; Mattson, S.; Föhlisch, A.; Wurth, W.; Nagasono, M.; Piancastelli, M.N. *Physical Review B* **68**, 115408 (2003).

121. Marsh, A.L.; Burnett, D.J.; Fischer, D.A.; Gland, J.L. *Journal of Physical Chemistry B* **107**, 12472 (2003).

122. Luk, Y-Y.; Abbott, N.L.; Crain, J.N.; Himpsel, F.J. *Journal of Chemical Physics* **120**, 10792-10798 (2004).

123. Holland, B.N.; Peltekis, N.; Farrelly, T.; Wilks, R.G.; Gavrila, G.; Zahn, D.R.T.; McGuinness, C.; McGovern, I.T. *Physica Status Solidi B* (in press June 2009).

124. Peisert, H.; Schwieger, T.; Auerhammer, J.M.; Knupfer, M.; Golden, M.S.; Fink, J.; Bressler, P.R.; Mast, M. *Journal of Applied Physics* **90**, 466 (2001).

125. Biswas. I.; Peisert, H.; Nagel, M.; Casu, M.B.; Schuppler, S.; Nagel, P. *Journal of Chemical Physics* **126**, 17404 (2007).

126. Alfredsson, Y.; Åhlund, J.; Nilson, K.; Kjelgaard, L.; O'Shea, J.N.; Theobald, J.; Bao, Z.; Mårtensson, N.; Sandell, A.; Puglia, C.; Siegbahn, H. *Thin Solid Films* **493**, 13 (2005).

127. Barrena, E.; Ossó, J.O.; Schreiber, F.; Garriga, M.; Alonso, M.I.; Dosch, H. *Journal of Materials Research* **19**, 2061 (2004).

128. Kera, S.; Casu, M.B.; Schöll, A.; Schmidt, Th.; Batchelor, D.; Rühl, E.; Umbach, E. *Journal of Chemical Physics* **125**, 014705 (2006).

129. Ruocco, A.; Evangelista, F.; Attili, A.; Donzello, M.P.; Betti, M.G.; Giovanelli, L.; Gotter, R. *Journal of Electron Spectroscopy and Related Phenomena* **137-140**, 165 (2004).

130. DeLongchamp, D.M.; Jung, Y.; Fischer, D.A.; Lin, E.K.; Chang, P.; Subramanian, V.; Murphy, A.R.; Fréchet, J.M.J. *Journal of Physical Chemistry B* **110**, 10645 (2006).

131. Cremer, J.; Bäuerle, P. *Journal of Materials Chemistry* **16**, 874 (2006).

132. De Bettignies, R.; Nicolas, Y.; Blanchard, P.; Levillain, E.; Nunzi, J.-M.; Roncali, J. *Advanced Materials* **15**, 1939 (2003).

133. Kim, K.H.; Chi, Z.; Cho, M. J.; Jin, J.-I.; Cho, M. Y.; Kim, S. J.; Joo, J.-S.; Choi, D.H. *Chemistry of Materials* **19**, 4925 (2007).

134. Cho, M.Y.; Kim, S.J.; Han, Y.D.; Park, D.H.; Kim, K.H.; Choi, D.H.; Joo, J. *Advanced Functional Materials* **18** 2905 (2008).

135. Lee, T.W.; Kim, D.C.; Kang, N.S.; Yu, J.W.; Cho, M.J.; Kim, K.H.; Choi, D.H. *Chemistry Letters* **37**, 866 (2008).

136. Kim, K.H.; Chi, Z.; Cho, M. J.; Choi, D.H.; Kang, H.S.; Cho, M.Y.; Joo, J.-S. *Applied Physics Letters* **89**, 202109 (2006).

137. Püttner, R.; Kolczewski, C.; Martins, M.; Schlachter, A.S.; Snell, G.; Sant'Anna, M.; Viefhaus, J.; Hermann, K.; Kaindl, G. *Chemical Physics Letters* **393**, 361 (2004).

138. Lee, H.; Jeon, S.-M.; Kim, H.-D.; Lim, D.K.; Jung, S.-J.; Kim, S. *Journal of Physics: Condensed Matter* **20**, 135006 (2008).

APPENDIX A. NEXAFS INPUT FILES

The files used for the StoBe calculations all have the same basic format, with small differences in the way that, for example, the orbital occupancy is treated. Below is an example of the input file that can be used to simulate the N *1s* NEXAFS spectrum of glycine using the transition state approximation. The lines which will be varied in the energy calibration procedure are italicised, and the required changes are outlined at the end of the file.

```
ln -s $STOBEHOME/Basis/baslib.new7 fort.3
ln -s $STOBEHOME/Basis/symbasis.new fort.4
cat >help.inp <</.
title
glycine, N 1s NEXAFS
nosy
cartesian angstrom
O1     1.61392       -0.63809      -0.10324 8.0
O2     0.48941        1.27522       0.05233 8.0
N     -1.91881        0.08846      -0.13026 7.0
C1    -0.74305       -0.75348       0.16143 6.0
C2     0.55854        0.02789       0.01974 6.0
H     -1.98306        0.90090       0.51534 1.0
H     -0.82682       -1.11895       1.18612 1.0
H     -1.85347        0.47605      -1.08527 1.0
H     -0.74308       -1.60888      -0.50715 1.0
H     -2.81788       -0.45824      -0.08038 1.0
end
runtype start
scftype direct
potential nonlocal be88 pd86
grid fine
multiplicity 1
virt all
charge 0
maxcycles 1000
econvergence 0.0000001
dconvergence 0.0000001
dmixing mdens 0.06
```

```
diis new 7
orbi 5d
fsym scfocc excited
alfa 20
beta 20
sym 1
alfa 20 1 3 0.5
beta 20 0
end
xray xas
remthreshold  1.D-6
end
ctrl
end
A-OXYGEN (5,2;5,2)
A-OXYGEN (5,2;5,2)
A-NITROGEN (5,2;5,2)
A-CARBON (5,2;5,2)
A-CARBON (5,2;5,2)
A-HYDROGEN (3,1;3,1)
A-HYDROGEN (3,1;3,1)
A-HYDROGEN (3,1;3,1)
A-HYDROGEN (3,1;3,1)
A-HYDROGEN (3,1;3,1)
O-OXYGEN (7111/411/1)
O-OXYGEN (7111/411/1)
O-NITROGEN iii_iglo
O-CARBON (7111/411/1)
O-CARBON (7111/411/1)
O-HYDROGEN (41/1*)
O-HYDROGEN (41/1*)
O-HYDROGEN (41/1*)
O-HYDROGEN (41/1*)
O-HYDROGEN (41/1*)
X-DUMMY
X-DUMMY
X-FIRST
end
/.
$STOBEHOME/bin/StoBe.x <help.inp >& glycineNxas.out
mv fort.2 glycineNxas.res
mv fort.11 glycineN.xas
rm help.inp fort.*
```

The changes to the italicized block that are required to model the first core-excited states are as follows:

fsym scfocc excited
alfa 21
beta 20
sym 1
alfa 21 1 3 0.0
beta 20 0
end

The modification used to perform the ground state calculation is simpler. The keywords pertaining to the XAS calculation can be removed altogether if desired, and the entire block can be replaced with:

fsym aufbau

APPENDIX B. XES INPUT FILE

A sample input file for a StoBe XES calculation (of pentacene, in this case) is shown below.

```
ln -s $STOBEHOME/Basis/baslib.new7 fort.3
ln -s $STOBEHOME/Basis/symbasis.new fort.4
cat >help.inp <</.
title
Pentacene- Schiefer Struct C XAS
nosy
cartesian angstrom
 C1      1.247  -0.647  -0.108  6.0
 C2      0.775  -0.326   1.167  6.0
 C3      1.477  -0.610   2.344  6.0
 C4      0.973  -0.271   3.594  6.0
 C5      1.723  -0.555   4.797  6.0
 C6      1.242  -0.219   6.006  6.0
 C7     -0.042   0.431   6.128  6.0
 C8     -0.769   0.717   5.013  6.0
 C9     -0.297   0.392   3.691  6.0
 C10    -1.004   0.678   2.556  6.0
 C11    -0.516   0.340   1.278  6.0
 C12    -1.247   0.647   0.108  6.0
 C13    -0.775   0.326  -1.167  6.0
 C14    -1.477   0.610  -2.344  6.0
 C15    -0.973   0.271  -3.594  6.0
 C16    -1.723   0.555  -4.797  6.0
 C17    -1.242   0.219  -6.006  6.0
 C18     0.042  -0.431  -6.128  6.0
 C19     0.769  -0.717  -5.013  6.0
 C20     0.297  -0.392  -3.691  6.0
 C21     1.004  -0.678  -2.556  6.0
 C22     0.516  -0.340  -1.278  6.0
 H1      2.068  -1.076  -0.188  1.0
 H2      2.301  -1.037   2.287  1.0
 H3      2.549  -0.976   4.732  1.0
 H4      1.740  -0.406   6.768  1.0
 H5     -0.373   0.653   6.968  1.0
 H6     -1.594   1.135   5.108  1.0
```

```
 H7    -1.826   1.106   2.630  1.0
 H8    -2.068   1.076   0.188  1.0
 H9    -2.301   1.037  -2.287  1.0
 H10   -2.549   0.976  -4.732  1.0
 H11   -1.740   0.406  -6.768  1.0
 H12    0.373  -0.653  -6.968  1.0
 H13    1.594  -1.135  -5.108  1.0
 H14    1.826  -1.106  -2.630  1.0
end
runtype start
scftype direct
potential nonlocal be88 pd86
grid fine
multiplicity 1
virt all
charge 0
maxcycles 800
econvergence 0.0000001
dconvergence 0.0000001
dmixing mdens 0.06
diis new 5
orbi 5d
fsym scfocc
alfa 73
beta 73
xray xes 6 1 2 3 4 5 6
end
ctrl
end
A-CARBON (5,2;5,2)
A-CARBON (5,2;5,2)
A-CARBON (5,2;5,2)
A-CARBON (5,2;5,2)
A-CARBON (5,2;5,2)
A-CARBON (5,2;5,2)
A-CARBON (5,2;5,2)
A-CARBON (5,2;5,2)
A-CARBON (5,2;5,2)
A-CARBON (5,2;5,2)
A-CARBON (5,2;5,2)
A-CARBON (5,2;5,2)
A-CARBON (5,2;5,2)
A-CARBON (5,2;5,2)
A-CARBON (5,2;5,2)
A-CARBON (5,2;5,2)
A-CARBON (5,2;5,2)
A-CARBON (5,2;5,2)
```

A-CARBON (5,2;5,2)
A-CARBON (5,2;5,2)
A-CARBON (5,2;5,2)
A-CARBON (5,2;5,2)
A-CARBON (5,2;5,2)
A-HYDROGEN (3,1;3,1)
A-HYDROGEN (3,1;3,1)
A-HYDROGEN (3,1;3,1)
A-HYDROGEN (3,1;3,1)
A-HYDROGEN (3,1;3,1)
A-HYDROGEN (3,1;3,1)
A-HYDROGEN (3,1;3,1)
A-HYDROGEN (3,1;3,1)
A-HYDROGEN (3,1;3,1)
A-HYDROGEN (3,1;3,1)
A-HYDROGEN (3,1;3,1)
A-HYDROGEN (3,1;3,1)
A-HYDROGEN (3,1;3,1)
A-HYDROGEN (3,1;3,1)
O-CARBON (7111/411/1)
O-CARBON (7111/411/1)
O-CARBON (7111/411/1)
O-CARBON (7111/411/1)
O-CARBON (7111/411/1)
O-CARBON (7111/411/1)
O-CARBON (7111/411/1)
O-CARBON (7111/411/1)
O-CARBON (7111/411/1)
O-CARBON (7111/411/1)
O-CARBON (7111/411/1)
O-CARBON (7111/411/1)
O-CARBON (7111/411/1)
O-CARBON (7111/411/1)
O-CARBON (7111/411/1)
O-CARBON (7111/411/1)
O-CARBON (7111/411/1)
O-CARBON (7111/411/1)
O-CARBON (7111/411/1)
O-CARBON (7111/411/1)
O-CARBON (7111/411/1)
O-CARBON (7111/411/1)
O-CARBON (7111/411/1)
O-CARBON (7111/411/1)
O-HYDROGEN (41/1*)
O-HYDROGEN (41/1*)
O-HYDROGEN (41/1*)
O-HYDROGEN (41/1*)
O-HYDROGEN (41/1*)

```
O-HYDROGEN (41/1*)
O-HYDROGEN (41/1*)
O-HYDROGEN (41/1*)
O-HYDROGEN (41/1*)
O-HYDROGEN (41/1*)
O-HYDROGEN (41/1*)
O-HYDROGEN (41/1*)
O-HYDROGEN (41/1*)
O-HYDROGEN (41/1*)
end
/.
$STOBEHOME/bin/StoBe.x <help.inp >& pentXES.out
#mv fort.96 PFN.dos
mv fort.2 pentXES.res
mv fort.11 pentXES.xes
rm help.inp fort*
```

APPENDIX C. BROADENING FILES

A sample input file used to broaden a N *1s* NEXAFS spectrum simulation is given below, followed by a summary of the modifications needed to perform an angle-resolved broadening.

```
ln -s GlycineN.xas fort.1
cat >help.inp <</.
title
glycine, N1s Xray absorption spectrum
print
range 390 434.9
points 450
width 0.7 6.5 400. 412.
xray xas
total 1
end
/.
$STOBEHOME/bin/xrayspec.x < help.inp > GlycineNBroad.out
mv XrayT001.out Spectrum.out
rm help.inp fort.*
```

Angle-resolved calculations replace the *total 1* keyword with the *angle* keyword followed by the values of the two angles θ and ϕ describing the incident direction of the X-rays:

```
angle 90 0 1
```

APPENDIX D. CONTAMINATION OF AU MESH

The Au mesh used to monitor the photon flux at the SGM beamline became contaminated during the course of the measurements of 4(HPBT) and PCBM. The potassium contaminant did not have an effect on the analysis of the measured C *1s* NEXAFS spectra, as the structure arising from the K $L_{2,3}$ NEXAFS was found only in the region from 295 eV to 302 eV. This contamination led to the sharp decreases in absorption signal in this region in many of the spectra contained in this study, but it is clear from Figure D.1 that the region of interest to the C *1s* NEXAFS (below 295 eV) is unaffected.

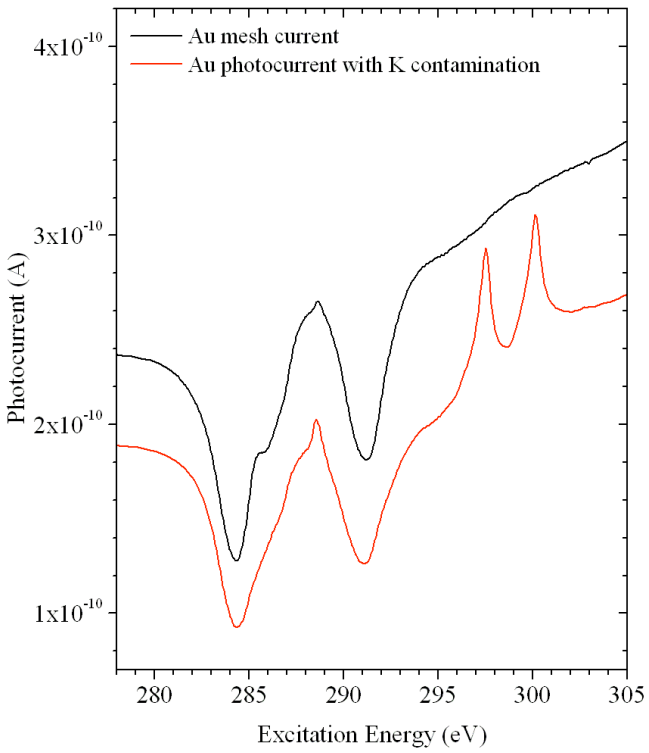

Figure D.1: Au mesh photocurrent at the C *1s* absorption edge, showing the effects of K contamination. The sharp peaks at 297.5 eV and 300 eV are due to K $L_{2,3}$ absorption.

APPENDIX E. UNPROCESSED GLYCINE TEY SPECTRA

The glycine spectra shown in Figure E.1 have been normalised to the measured mesh current, but have not undergone background subtraction of edge-jump normalisation. The edge-jump of the O *1s* NEXAFS decreases dramatically upon irradiation, indicating that the amount of oxygen in the sample has decreased over the course of the experiment. By comparison, the edge-jumps in the C *1s* and N *1s* NEXAFS are not dramatically affected.

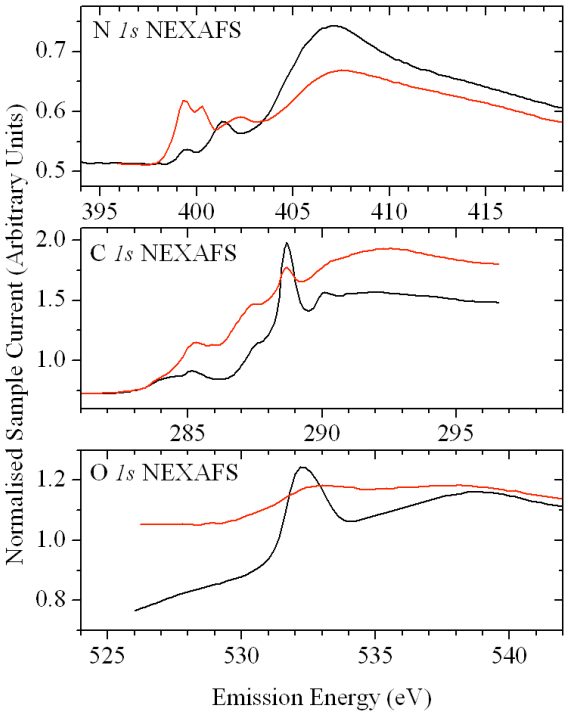

Figure E.1: Mesh-current normalised TEY spectra of glycine in the early (black) and late (red) stages of radiation damage.

APPENDIX F. TBPE ATOMIC COORDINATES

The coordinates of the heavy atoms used in the simulations of the TBPe spectra are:

C	0.00043424	-1.43311630	0.00337250
C	0.00023871	-2.86623529	0.00217225
C	1.23195750	-3.57583934	0.00818594
C	2.45170615	-2.91712822	0.00192320
C	2.43216833	-1.49636711	-0.00761336
C	1.25765809	-0.74098445	-0.00273322
C	3.80596772	-3.66378055	-0.00915584
C	4.55246994	-3.35560013	-1.33032169
C	3.62808315	-5.19330529	0.09189940
C	4.67176089	-3.19622575	1.18624441
C	1.25757946	0.74027615	-0.00181271
C	1.23192174	3.57532363	0.00846644
C	2.43209602	1.49548682	0.00535433
C	2.45154575	2.91617045	0.01362914
C	3.62738019	5.19179494	0.10493687
C	3.80627813	3.66182351	0.01711711
C	4.57352598	3.34347301	-1.28954742
C	4.65489476	3.20444300	1.22839869
C	0.00043686	1.43285762	-0.00331924
C	0.00023596	2.86591286	-0.00292897
C	-1.25660356	-0.74046154	0.00390551
C	-1.25675723	0.74073456	0.00188065
C	-1.23166092	-3.57550227	-0.00632165
C	-1.23162422	3.57531740	-0.01258598
C	-2.43117970	-1.49546356	0.00031421
C	-2.43147519	1.49579745	0.00358590
C	-2.45114206	-2.91600746	-0.00763335
C	-2.45134576	2.91649789	-0.00819292
C	-3.62873167	5.19179786	-0.10576673
C	-3.62875808	-5.19002828	-0.09780397
C	-3.80640721	-3.66032004	-0.00632530
C	-3.80606144	3.66245227	-0.00189929
C	-4.55587839	3.35644946	1.31793336
C	-4.56660282	-3.34373367	1.30480323
C	-4.66084099	-3.19965043	-1.21235398
C	-4.66889183	3.19154515	-1.19820494

APPENDIX G. 4(HPBT) ATOMIC COORDINATES

The two models used in the StoBe simulations of 4(HPBT) are described in Section 10.2. The *xyz* coordinates of the heavy atoms of the single-armed model are:

S	-5.53221	-2.61252	0.32604
S	-8.84257	-5.50705	-0.03059
C	-1.24879	-0.69864	0.00000
C	0.00396	-1.35800	-0.00464
C	1.24518	-0.69864	0.00000
C	1.24725	0.73793	-0.06776
C	0.00361	1.39728	0.00000
C	-1.23873	0.73341	0.02860
C	-2.51479	-1.42033	0.05699
C	-2.73061	-2.76894	-0.02192
C	-4.00352	-3.44367	0.05514
C	-4.22537	-4.81640	-0.06278
C	-5.58720	-5.19384	0.06510
C	-6.44401	-4.11857	0.29111
C	-7.87849	-4.12218	0.46978
C	-8.70535	-3.14195	1.01106
C	-10.08374	-3.50967	1.02875
C	-10.33556	-4.76658	0.50569
C	-11.65038	-5.48666	0.36161
C	-11.77615	-6.77089	1.21515
C	-13.10345	-7.51066	0.97805
C	-13.23416	-8.79436	1.81766
C	-14.52093	-9.60336	1.55574
C	-15.81341	-8.90194	2.01436
C	2.41317	1.61585	-0.32139
C	2.41721	-1.59017	0.17518
C	3.52586	1.33760	-1.03754
C	3.59412	-1.32680	0.78585
C	-2.48459	1.52826	0.03126
C	-2.65414	2.72709	0.63484

The coordinates of the heavy atoms used in the four-armed model are:

S	0.33013	-0.87652	6.65067
S	1.00161	-0.63401	-8.89089

S	5.11811	0.61587	3.68796
S	9.18869	0.26136	4.62445
S	-0.25349	-0.47985	-4.90477
S	-0.92176	-1.31927	10.61614
S	-5.05610	0.75277	-1.84778
S	-9.12299	0.42018	-2.80803
C	0.01027	0.00000	-0.46460
C	0.01544	-0.08744	-1.84681
C	0.03098	-1.15162	9.26183
C	0.04762	-0.57059	-7.52859
C	0.05587	-0.27662	3.62704
C	0.05959	-0.09380	2.25418
C	0.17875	-2.11501	12.92375
C	0.35326	-1.81063	11.54724
C	0.57965	-0.21932	-6.32064
C	0.96534	0.17255	-3.98340
C	0.97075	0.26927	-2.63159
C	1.14629	0.00000	0.23230
C	1.22608	-0.03312	1.55939
C	1.27073	-1.48124	9.54701
C	1.44603	-1.85046	10.83152
C	1.75063	0.32868	-6.06701
C	1.96253	0.54629	-4.76505
C	2.45352	0.05725	2.19905
C	3.59058	-0.32890	1.71141
C	4.81640	-0.24235	2.29994
C	5.92613	-0.81992	1.87801
C	6.72173	0.18054	3.69746
C	6.98802	-0.58944	2.66084
C	7.31448	1.40202	5.70388
C	7.56864	0.63800	4.66508
C	8.40567	1.67828	6.44639
C	9.50486	1.13685	5.99080
C	-0.09116	-1.28011	-11.24839
C	-0.26841	-1.07350	-9.85420
C	-0.50523	-0.72343	8.08086
C	-0.89597	-0.17512	5.77614
C	-0.90292	0.01473	4.43425
C	-1.07663	-0.05783	1.55853
C	-1.15654	0.00000	0.23230
C	-1.18862	-0.89300	-7.83633
C	-1.36043	-1.17441	-9.14335
C	-1.68211	-0.17180	7.86527
C	-1.89683	0.13299	6.58138
C	10.82545	1.23575	6.49976
C	-2.38512	0.12120	-0.40005

C	-3.51779	-0.30991	0.05932
C	-4.74469	-0.19606	-0.52227
C	-5.84800	-0.81328	-0.14169
C	-6.65497	0.30195	-1.88793
C	-6.91260	-0.54065	-0.90710
C	-7.26153	1.65275	-3.80535
C	-7.50709	0.81608	-2.82194
C	-8.35590	1.96795	-4.52740
C	-9.44905	1.38456	-4.11073
C	-10.77081	1.50423	-4.61213